

# Development of Novel Quantitative Ultrasound Techniques

Noushin Jafarpisheh

A Thesis  
In the Department  
of  
Electrical and Computer Engineering

Presented in Partial Fulfillment of the Requirements  
For the Degree of  
Doctor of Philosophy (Electrical and Computer Engineering) at  
Concordia University  
Montréal, Québec, Canada

December 2022  
© Noushin Jafarpisheh, 2022

Concordia University  
School of Graduate Studies

This is to certify that the thesis prepared

By: **Noushin Jafarpisheh**

Entitled: **Development of Novel Quantitative Ultrasound Techniques**

and submitted in partial fulfillment of the requirements for the degree of

**Doctor of Philosophy (Electrical and Computer Engineering)**

complies with the regulations of this University and meets the accepted standards with respect to originality and quality.

Signed by the Final Examining Committee:

*Dr. Fuzhan Nasiri*

Chair

*Dr. Parvin Mousavi*

External Examiner

*Dr. Nizar Bougila*

External to Program

*Dr. M. Omair Ahamd*

Examiner

*Dr. Weiping Zhou*

Examiner

*Dr. Hassan Rivaz*

Supervisor

Approved by Dr. Jun Cai

Graduate Program Director

Date of Defense: February 9, 2023

Dr. Mourad Debbabi, Dean  
Faculty of Engineering and Computer Science

# Abstract

## Development of Novel Quantitative Ultrasound Techniques

**Noushin Jafarpisheh, Ph.D.**  
**Concordia University**

Ultrasound is a medical imaging modality with many advantages, such as being real-time, portable, and cost-effective. Nevertheless, it provides a qualitative representation of the human body, which cannot reveal the physical characteristics of the tissue. Quantitative ultrasound (QUS) has evolved as a non-invasive ultrasound-based imaging modality to investigate the acoustic properties of tissue microstructure. It aims at recovering quantitative properties of tissue microstructure by investigating the power spectra of the radio frequency data or statistics of the envelope of the backscattered signal. The accuracy and precision of microstructural properties are necessary for a correct description of tissue microstructure. In particular, spectral-based techniques estimate the frequency-dependent backscatter coefficient (BSC) from the echo signal power spectra after removing attenuation effects from tissues between the transducer and the region of interest. The BSC can be parametrized in terms of a power law function or form factor models. While the power law model is associated with physics, the form factor can inform sub-resolution scatterer features, such as the effective scatterer diameter (ESD) and the acoustic concentration (AC). Common approaches to estimating the ESD and AC are based on minimization strategies of the squared difference between a model spectrum and a measured spectrum (or form factors). A key aspect of ESD and AC estimation is that it accurately and precisely quantifies the scattering properties of tissue. This thesis aims to introduce our novel regularized-based strategies to improve the estimation of the average attenuation, BSC, ESD, and AC. Chapter 2 presents two versions of our proposed method, ALGEBRA, to accurately and precisely estimate average attenuation and BSC in various tissue-mimicking phantoms. The power spectra at each frequency and depth have equal weights in ALGEBRA. However, due to the attenuation, the high-frequency contents of the power spectra at deep regions have a low signal-to-noise ratio. Additionally, the average attenuation varies gradually while the BSC alters markedly in different parts of the tissue. In Chapter 3, we consider these two shortcomings of the ALGEBRA and propose a novel method optimized using

alternating direction method of multipliers (ADMM) to estimate the same parameters. Chapters 4 to 6 are dedicated to estimating ESD and AC using dynamic programming (DP) and analytical-based methods. In Chapter 7, we propose a novel approach to estimate the distribution of scatterer sizes instead of reporting a single size to more accurately characterize tissue. In the final chapter, we provide conclusions and future work.

# **Acknowledgments**

I am deeply indebted to my dear supervisor, Dr. Hassan Rivaz who generously provided knowledge and expertise. I could not have undertaken this journey without his technical supervision and excellent cooperation during my research. My sincere appreciation goes out to you for all your support and guidance. It is my sincere pleasure to extend my gratitude to our collaborators Dr. Ivan M. Rosado Mendez and Dr. Tim J Hall at Wisconsin University. Besides, I deeply express my gratitude to the committee members, Dr. Parvin Mousavi, Dr. Nizar Bougila, Dr. M. Omair Ahamd, and Dr. Weiping Zhou for invaluable patience and feedback. I am also grateful to my lovely parents and my sister for their emotional support.

# Contents

List of Figures.....	ix
List of Tables.....	xii
List of Abbreviation.....	xiii
<b>1 Chapter 1 Introduction and Literature Review .....</b>	<b>1</b>
1.1 Ultrasound Imaging .....	1
1.2 Quantitative Ultrasound .....	3
1.2.1 Literature Review .....	5
1.2.2 Clinical Applications .....	7
1.3 Thesis Statement .....	7
1.4 List of Publications.....	7
<b>2 Chapter 2 Analytic Global Regularized Backscatter Quantitative Ultrasound.....</b>	<b>10</b>
2.1 Background .....	10
2.2 Algorithms.....	11
2.2.1 1D-ALGEBRA.....	13
2.2.2 2D-ALGEBRA.....	16
2.3 Methods .....	19
2.3.1 Tissue-mimicking phantoms .....	19
2.3.2 Data Acquisition .....	21
2.3.3 Power Spectra Estimation .....	22
2.4 Results .....	24
2.5 Discussion .....	30
2.6 Conclusion .....	31
<b>3 Chapter 3 Physics-Inspired Regularized Pulse-Echo Quantitative Ultrasound: Efficient Optimization with ADMM.....</b>	<b>34</b>
3.1 Background .....	34
3.2 Methods .....	35
3.2.1 ADMM for L1 Norm Regularization in QUS.....	35
3.2.2 Weighted Frequency.....	38
3.2.3 Tissue mimicking phantom and data acquisition .....	39
3.2.4 Quantitative Metrics.....	42
3.3 Results .....	44
3.4 Discussion .....	46

3.5	<b>Conclusion</b> .....	48
<b>4</b>	<b>Chapter 4 Regularized Estimation of Effective Scatterer Size and Acoustic Concentration Quantitative Ultrasound Parameters Using Dynamic Programming</b> .....	<b>52</b>
4.1	<b>Background</b> .....	52
4.2	<b>Methods</b> .....	53
4.2.1	<b>Gaussian form factor</b> .....	53
4.2.2	<b>General form factor</b> .....	54
4.3	<b>Results</b> .....	57
4.4	<b>Conclusions</b> .....	58
<b>5</b>	<b>Chapter 5 Evaluation of Contrast to Noise Ratio of Parametric Images of Regularized Estimates of Quantitative Ultrasound</b> .....	<b>61</b>
5.1	<b>Background</b> .....	61
5.2	<b>Methods</b> .....	62
5.2.1	<b>Data Acquisition</b> .....	62
5.2.2	<b>Estimation of the Acoustic Concentration</b> .....	62
5.2.3	<b>Comparison of Object Conspicuity</b> .....	62
5.3	<b>Results</b> .....	63
5.4	<b>Discussion and Conclusion</b> .....	64
<b>6</b>	<b>Chapter 6 Analytical Globally-Regularized Estimation of Effective Scatterer Diameter and Acoustic Concentration in Quantitative Ultrasound</b> .....	<b>67_Toc127821676</b>
6.1	<b>Background</b> .....	67
6.2	<b>Methods</b> .....	67
6.3	<b>Results</b> .....	70
6.4	<b>Discussion</b> .....	71
6.5	<b>Conclusions</b> .....	71
<b>7</b>	<b>Chapter 7 Scatterer Size Distribution Estimation in Quantitative Ultrasound using Constrained Optimization</b> .....	<b>74</b>
7.1	<b>Background</b> .....	73
7.2	<b>Materials and Methods</b> .....	74
7.2.1	<b>Data</b> .....	75
7.2.2	<b>Frequency range</b> .....	75
7.2.3	<b>Quantitative analysis</b> .....	76
7.3	<b>Results and Discussion</b> .....	77
7.4	<b>Conclusions</b> .....	84

<b>8</b>	<b>Chapter 8 Conclusions and Future Work.....</b>	<b>85</b>
8.1	Conclusions.....	85
8.2	Future Work.....	86
	References.....	88

## List of Figures

Figure 1-1 Interaction of ultrasound waves with tissues.....	1
Figure 1-2 Verasonics ultrasound machine at IMPACT lab (a). An ultrasound transducer at IMPACT lab (b). An example of a B-mode image of a three-layered phantom (c). The middle layer extends from 40mm to 55mm depth. ....	2
Figure 1-3 Diffuse scattering (a). Oblique specular reflection (b). Perpendicular specular reflection (c). ....	3
Figure 1-4 An overview of modalities providing quantitative tissue properties. ....	4
Figure 2-1 Regularization strategies for (a) 1D- and (b) 2D-ALGEBRA. ....	17
Figure 2-2 Results of 1D-ALGEBRA (blue), 2D-ALGEBRA (red), DP (green), and LSQ (cyan) in phantom A (uniform). The error bars show the standard deviation over the 400 samples for attenuation coefficient (a) and reconstructed BSC averaged over 400 samples (b). In (a), blue, red, cyan and black are superimposed. The black dashed line is the GT. ....	25
Figure 2-3 Parametric images of the BSC at the center frequency in phantom A (uniform). Results are shown on a dB scale with respect to $10^{-4} \text{ cm}^{-1} \text{ sr}^{-1}$ . The colorbar shows BSC at the center frequency. ....	26
Figure 2-4 Results of 1D-ALGEBRA (blue), 2D-ALGEBRA (red), DP (green), and LSQ (cyan) in phantom C (attenuation step). The error bars show the standard deviation over the 860 samples for attenuation coefficient (a) and reconstructed BSC averaged over 400 samples in layer 1 (b), layer 2 (c), layer 3 (d). The black dashed line is the ground truth values. The red curve is superimposed by the blue curve. ....	27
Figure 2-5 Parametric images of the local attenuation (computed from Eq. (2-32)) of phantom C (attenuation step). The color bar shows the value of local attenuation. ....	28
Figure 2-6 Results of 1D-ALGEBRA (blue), 2D-ALGEBRA (red), DP (green), and LSQ (cyan) in phantom D (backscatter step). The error bars show the standard deviation over the 860 samples for the effective attenuation (a) and reconstructed BSC averaged over 400 samples in layer 1 (b), layer 2 (c), layer 3 (d). The black dashed line is the GT. The red curve is superimposed by the blue curve. ....	29
Figure 2-7 Parametric image of the backscatter coefficient at the center frequency of phantom D (backscatter step). Results are shown on a dB scale with respect to $10^{-4} \text{ cm}^{-1} \text{ sr}^{-1}$ . ....	30
Figure 2-8 Parametric image of the backscatter coefficient at the center frequency of phantom E (inclusion phantom). Results are shown on a dB scale with respect to $10^{-4} \text{ cm}^{-1} \text{ sr}^{-1}$ . ....	32
Figure 2-9 Influence of regularization weights in the parametric images of phantom E with 1D-ALGEBRA. Weights in (a): [10 10 10], weights in (b): [104 104 104]. ....	33
Figure 3-1 Lateral average of the power spectra of sample phantom (a) and reference phantom (b) in the logarithmic scale for the region with specular reflectors. ....	40
Figure 3-2 Lateral average of the power spectra of sample phantom (a) and reference phantom (b) in the logarithmic scale for the region with inclusions. ....	41
Figure 3-3 Contour levels of the lateral average of the power spectra of reference phantom in the logarithmic scale for the region with specular reflectors. ....	41
Figure 3-4 Contour levels of the lateral average of the power spectra of sample phantom (a) and reference phantom (b) in the logarithmic scale for the region with inclusions. ....	42
Figure 3-5 $wd$ for the region with specular reflectors. ....	42
Figure 3-6 $wd$ for the region with inclusions. ....	42
Figure 3-7 Location of ROI in the region with specular reflectors. ....	43

Figure 3-8 Location of ROI in the region with inclusions. ....43

Figure 3-9 Comparison of bias (a) and variance (b) of the BSC using ALGEBRA (ALGEBRA No *wd*), ALGEBRA associated with weighting the data term (ALGEBRA *w\_d*), ADMM without weighting the data term and using L2 norm in the regularization part for all the parameters (ADMM No *wd*), ADMM associated with weighting the data term and using L2 norm in the regularization part for all the parameters (ADMM *wd*), ADMM without weighting the data term and using L1 norm for the BSC and L2 norm for the average attenuation (ADMM L1L2 No *wd*), and ADMM associated with weighting the data term and using L1 norm for the BSC and L2 norm for the average attenuation (ADMM L1L2 *wd* ) in four ROI of the region with specular reflectors. Results are shown on a dB scale with respect to  $10^{-4} \text{ cm}^{-1} \text{ sr}^{-1}$ . ....45

Figure 3-10 Comparison of bias (a) and variance (b) of the average attenuation using ALGEBRA (ALGEBRA No *wd*), ALGEBRA associated with weighting the data term (ALGEBRA *w\_d*), ADMM without weighting the data term and using L2 norm in the regularization part for all the parameters (ADMM No *wd*), ADMM associated with weighting the data term and using L2 norm in the regularization part for all the parameters (ADMM *wd*), ADMM without weighting the data term and using L1 norm for the BSC and L2 norm for the average attenuation (ADMM L1L2 No *wd*), and ADMM associated with weighting the data term and using L1 norm for the BSC and L2 norm for the average attenuation (ADMM L1L2 *wd* ) in four ROI of the region with specular reflectors. ....46

Figure 3-11 Qualitative comparison of parametric image of the BSC at the center frequency of the region with inclusions, with GT (a), and different methods (b-g). Results are shown on a dB scale with respect to  $10^{-4} \text{ cm}^{-1} \text{ sr}^{-1}$ . ....49

Figure 3-12 Comparison of bias (a) and variance (b) of the BSC using ALGEBRA (ALGEBRA No *wd*), ALGEBRA associated with weighting the data term (ALGEBRA *wd*), ADMM without weighting the data term and using L2 norm in the regularization part for all the parameters (ADMM No *wd*), ADMM associated with weighting the data term and using L2 norm in the regularization part for all the parameters (ADMM *wd*), ADMM without weighting the data term and using L1 norm for the BSC and L2 norm for the average attenuation (ADMM L1L2 No *wd*), and ADMM associated with weighting the data term and using L1 norm for the BSC and L2 norm for the average attenuation (ADMM L1L2 *wd* ) in four ROI in the region with inclusions. Results are shown on a dB scale with respect to  $10^{-4} \text{ cm}^{-1} \text{ sr}^{-1}$ . ....50

Figure 3-13 Comparison of bias (a) and variance (b) of the average attenuation using ALGEBRA (ALGEBRA No *wd*), ALGEBRA associated with weighting the data term (ALGEBRA *wd*), ADMM without weighting the data term and using L2 norm in the regularization part for all the parameters (ADMM No *wd*), ADMM associated with weighting the data term and using L2 norm in the regularization part for all the parameters (ADMM *wd*), ADMM without weighting the data term and using L1 norm for the BSC and L2 norm for the average attenuation (ADMM L1L2 No *wd*), and ADMM associated with weighting the data term and using L1 norm for the BSC and L2 norm for the average attenuation (ADMM L1L2 *wd*) in four ROI in the region with inclusions. ....51

Figure 4-1 Results of LSQ (blue) and DP (red) methods using approach 1 in a simulated phantom with three layers and 20 instances of added zero-mean Gaussian noise. The error bars show the standard deviation over the 20 instances of noise for attenuation coefficient .....58

Figure 4-2 Results of LSQ and DP methods using approach 2 where n is fixed to 2 in a simulated phantom with three layers and 20 instances of added zero-mean Gaussian noise. The error bars in (a-c) show the standard deviation over the 20 instances of noise for attenuation coefficient (a),

backscatter coefficient magnitude B (b), scaled ESS A (c), and acoustic concentration (d). The black dashed line is the known values. ....	59
Figure 4-3 Results of LSQ and DP methods using approach 2 where n is not fixed to 2 and is estimated. The simulated phantom has three layers and 20 instances of added zero-mean Gaussian noise. The error bars show the standard deviation over the 20 instances of noise for attenuation coefficient (a), backscatter coefficient magnitude B (b), backscatter power law n (c), scaled ESS A (d), and acoustic concentration (e). The black dashed line is the known values. ....	60
Figure 5-1 Location of regions of interest in B-mode image. ....	63
Figure 5-2 B-mode (a) and AC (b) images of the cylindrical inclusions.....	64
Figure 5-3 Logarithmic scale of CNR of cylindrical inclusions in B-mode and AC images obtained with DP. The error bars represent differences between the two frames. ....	64
Figure 5-4 Scaled border resolution of cylindrical inclusions in B-mode and AC images obtained with DP. The vertical lines indicate, where each inclusion starts or ends. ....	66
Figure 6-1 Parametric image of ESD.....	70
Figure 6-2 Parametric mage of AC. the GT values are 236, 200 in the first and second layers, respectively.....	71
Figure 6-3 Parametric image of local attenuation.....	72
Figure 7-1 Logarithmic scale of the BSC for the uniform distribution, the cut-off frequency = 7.1.....	76
Figure 7-2 $GT_f$ , Guassian1 distribution (a), Comparison of estimation (red bars) and GTi (blue bars).....	78
Figure 7-3 $GT_f$ , Guassian2 distribution (a), Comparison of estimation (red bars) and GTi (blue bars).....	78
Figure 7-4 $GT_f$ , uniform distribution (a), Comparison of estimation (red bars) and GTi (blue bars).....	79
Figure 7-5 $GT_f$ , bi-modal distribution (a), Comparison of estimation (red bars) andGTi (blue bars).....	79
Figure 7-6 Comparison of estimations from the noiseless signal (red bars), noisy signals (yellow bars), and $GT_i$ (blue bars) for Gaussian1 distribution. The variance of noise in (b) is 10 times higher than (a).....	80
Figure 7-7 Comparison of estimations from the noiseless signal (red bars), noisy signals (yellow bars), and $GT_i$ (blue bars) for Gaussian2 distribution. The variance of noise in (b) is 10 times higher than (a).....	80
Figure 7-8 Comparison of estimations from the noiseless signal (red bars), noisy signals (yellow bars), and $GT_i$ (blue bars) for the uniform distribution. The variance of noise in (b) is 10 times higher than (a).....	81
Figure 7-9 Comparison of estimations from the noiseless signal (red bars), noisy signals (yellow bars), and $GT_i$ (blue bars) for the bi-modal distribution. The variance of noise in (b) is 10 times higher than (a).....	81

## List of Tables

Table 2-1(a) Regularization Weights in Four Phantoms, DP method .....	23
Table 2-1(b) Regularization Weights in Four Phantoms, 2D-ALGEBRA method .....	23
Table 7-1 Quantitative comparison of $RMSE_{nl}$ and $RMSE_{nh}$ respect to the $RMSE_c$ , where sub index nl, nh, and c refer to the low noise, high noise, and clean signal .....	82
Table 7-2 Uncertainty in $RMSE_{nl}$ and $RMSE_{nh}$ respect to the $RMSE_c$ , where sub index nl, nh, and c refer to the low noise, high noise, and clean signal. ....	82
Table 7-3 Quantitative comparison of $EMD_c$ , $EMD_{nl}$ , and $EMD_{nh}$ , , where sub index nl, nh, and c refer to the low noise, high noise, and clean signal. ....	83
Table 7-4 Uncertainty in $EMD_{nl}$ , and $EMD_{nh}$ , where sub index nl and nh refer to the low noise and high noise.....	83

## List of Abbreviations

AC	Acoustic Concentration
ADMM	Alternation Direction Method of Multipliers
ALGEBRA	AnaLytical Global rEgularized Backscatter
	quAntitative ultrasound
BGND	BackGrouND
BSC	Back Scatter Coefficient
CD	Contrast Detail
CNR	Contrast to Noise Ratio
DP	Dynamic Programming
EMD	Earth Mover's Distance
ESD	Effective Scatterer Diameter
ESS	Effective Scatterer Size
GFF	Gaussian Form Factor
gFF	general Form Factor
GT	Ground Truth
LASSO	Least Absolute Shrinkage and Selection Operator
LSQ	Least Squares
PEQUS	Pulse-Echo Quantitative Ultrasound
RF	Radio Frequency
ROI	Region Of Interest
RPM	Reference Phantom Method
QUS	Quantitative UltraSound
SNR	Signal to Noise Ratio

# Chapter 1

## Introduction and Literature Review

### 1.1 Ultrasound Imaging

Ultrasound is a medical imaging modality with a wide range of advantages, such as being real-time, portable, and cost-effective. The range of frequency for medical ultrasound devices is 1-20 MHz. Selecting the suitable transducer frequency is necessary for ensuring the best image resolution for diagnostic purposes. High-frequency ultrasound waves yield high axial-resolution images. However, they suffer from a higher level of attenuation compared to the lower frequency waves; thereby, they are the best suited for imaging shallow structures. On the other hand, low-frequency ultrasound waves can travel to deeper regions because of a lower amount of attenuation.

Figure 1.1 shows the interaction of ultrasound waves with tissues. An ultrasound transducer is made up of several piezoelectric crystals that vibrate when an electric current is applied to them. The vibrations generate ultrasound waves which moves through tissue. The ultrasound wave is partially converted to heat, partially scatters, partially penetrates deeper, and partially is reflected back to the transducer. Transmitting an ultrasound wave through tissues results in loss of amplitude, and, therefore, the energy of the ultrasound wave. The reflected echo received by the transducer is called radiofrequency (RF) data. The ultimate grayscale image displayed on the ultrasound machine is basically the envelope of the RF data and is called B-mode image. Figure 1.2(a)-(c) illustrates an ultrasound machine, a transducer, and a B-mode image, respectively.

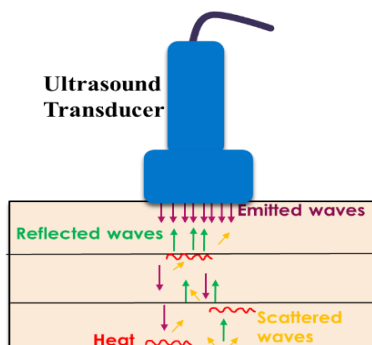


Figure 1-1 Interaction of ultrasound waves with tissues.

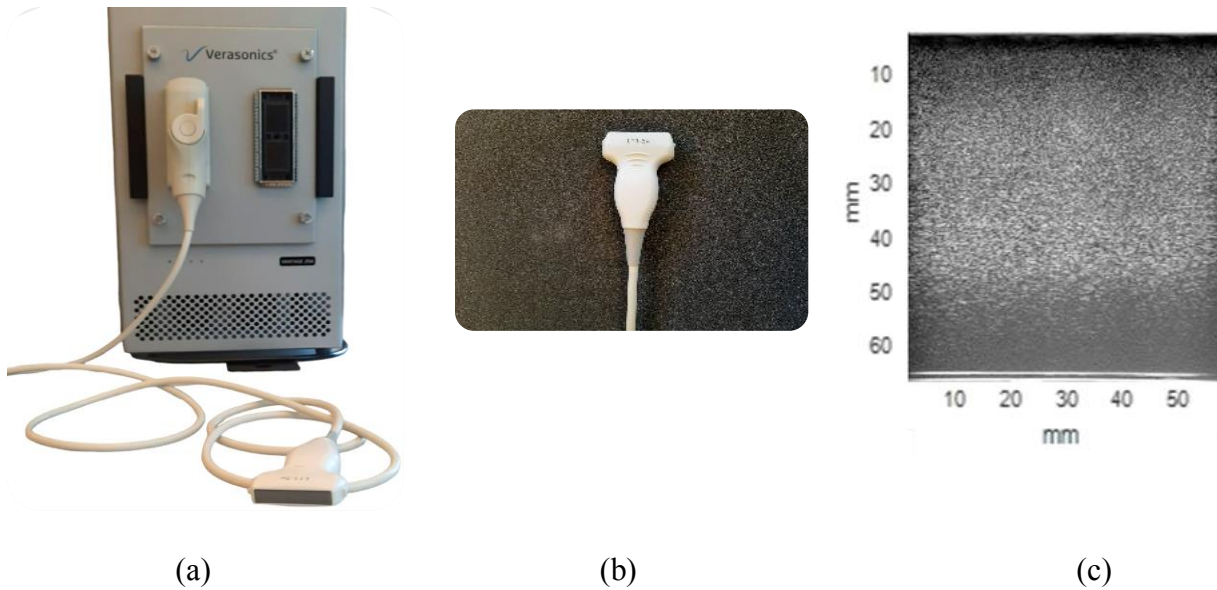


Figure 1-2 Verasonics ultrasound machine at IMPACT lab (a). An ultrasound transducer at IMPACT lab (b). An example of a B-mode image of a three-layered phantom (c). The middle layer extends from 40mm to 55mm depth.

More precisely, the interaction of ultrasound waves with tissue can be grouped as follows [1]:

- Absorption: It refers to a process that the energy of the ultrasound wave is converted to the heat.
- Refraction: Refraction occurs when sound encounters an interface between tissues with different sound speeds, causing the sound's direction to change
- Reflection: Upon reaching the ultrasound wave to two tissues with various impedances, different types of the reflection can occur, depending on the size of the interface compared to the wave length as well as the structure of the interface. When the interface is rough or its size is smaller than the wavelength, a minority of ultrasound wave travels back to the transducer while the remaining scatters in different directions (diffuse scattering). On the other hand, for the smooth interface with the size greater than the wavelength, a majority of the wave is received by the transducer (specular reflection). The transducer receives all of the echoes if the ultrasound wave encounters the interface perpendicularly. However, when the wave approaches the interface with an oblique angle, the wave reflects with the same angle, and the transducer receives no wave. Figure 1.3 depicts the aforementioned types of reflection.

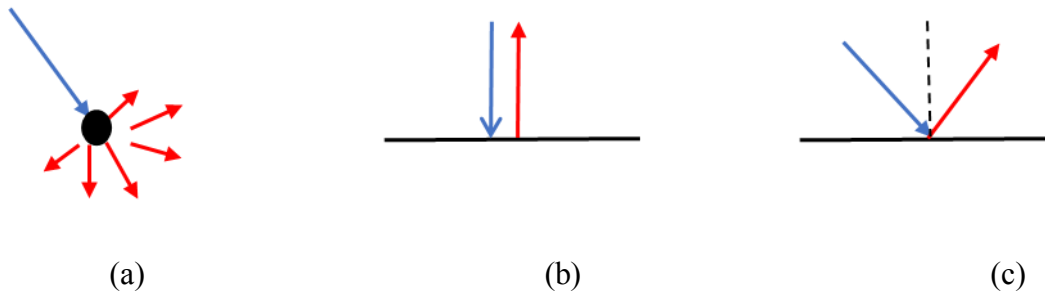


Figure 1-3 Diffuse scattering (a). Oblique specular reflection (b). Perpendicular specular reflection (c).

## 1.2 Quantitative Ultrasound

Despite all the advantages of ultrasound imaging, including being real-time and portable, an ultrasound image only describes tissue qualitatively. Therefore, accurate tissue classification based on ultrasound remains an area for improvement. Additionally, ultrasound is highly operator- and system-dependent, so its interpretation depends on the operator's skills.

Generally speaking, quantitative ultrasound (QUS) refers to the techniques that establish a quantitative assessment rather than presenting a qualitative map. Figure 1.4 illustrates a list of various modalities yielding quantitative analysis. However, QUS can reveal sub-resolution tissue characteristics [2]. It resolves the drawbacks of ultrasound imaging mentioned above by estimating the quantitative properties of tissue microstructure [3]–[6], aiming to extract the tissue's hidden properties.

QUS techniques are categorized into different fields [2], [7]–[10]. Backscatter-based techniques describe tissue microstructure in time or frequency domains. Envelope statics corresponds to the methods [10]–[14] in the time domain that incorporates estimating the ratio of the coherent and incoherent echoes backscattered from tissue and the number density of the scatterers. The primary models introduced for reflecting the statics of the envelope entail Rayleigh, Rician, Nakagami, K, and homodyned-K distributions [15], [16]. Spectral-based techniques [17]–[19] delve into the power spectra of the RF data backscattered from tissue. These techniques provide estimations of the acoustic properties of tissue which comprise attenuation [20]–[23], backscatter coefficient (BSC) [24], and scatterer properties [25]–[27]. In technical terms, total attenuation represents the energy loss due to the interaction between tissue and ultrasound waves during propagation. The attenuation level depends on the tissue's structure, frequency, and depth of propagation. For each

solid angle in each volume, BSC is explained by calculating the ratio of the mean intensity of the scatterers received at  $180^\circ$  angle and the mean intensity of the incident wave in the time domain [25], [28]. More precisely, spectrum-based QUS techniques [3], [17], [27], [29] investigate the Fourier transform of the RF data to estimate acoustic properties of tissue such as the effective scatterer diameter (ESD) [25], [30]–[34], scattering strength and acoustic concentration (AC) [17], [26], mean scatterer spacing [35]–[38], effective attenuation  $\alpha_{eff}$  (average attenuation from intervening tissues) [39], [40], and BSC  $\sigma_b$  [41]. The ESD (the correlation length of subwavelength variations of acoustic impedance) and AC (product of the number density of scatterers and the mean square acoustic impedance variation) are two crucial acoustic features associated with tissue microstructure [15]. These two parameters can be obtained by fitting form factor models to the experimental form factor derived from the BSC.

The form factor is the Fourier transform of the spatial correlation function of the relative impedance between scatterers and their surrounding [17], [25]. Spectral-based and envelope statics approaches can jointly be implemented for characterizing tissue [42]. Recent advancement in the area of QUS employs neural networks to improve tissue characterization [43]–[47]. Flow-based [15] and elasticity-based [48] classes describe blood flow and mechanical features of the tissue using Doppler shift and elastography methods, respectively. Blood flow can also be analyzed using non-Doppler methods, such as speckle tracking [49].

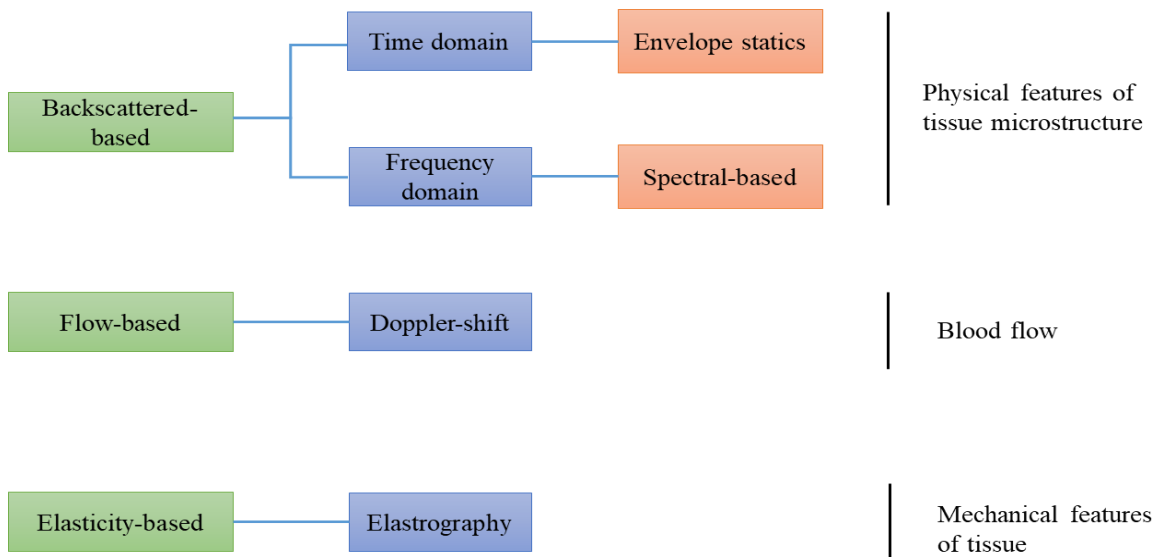


Figure 1-4 An overview of modalities providing quantitative tissue properties.

### 1.2.1 Literature Review

A growing attention has focused on improving QUS techniques. Recent work has demonstrated that the accuracy and precision of backscatter QUS parameters can be improved by regularizing the depth variation of estimates of tissue properties, based on the hypothesis of piece-wise variability with depth [50]–[54] or by regularizing lateral and axial variation [55]. Moreover, our group recently showed that using dynamic programming (DP) substantially improves estimates of effective attenuation  $\alpha_{\text{eff}}$  (average attenuation from intervening tissues) and BSC  $\sigma_b$  [56] compared to a least square (LSQ) method previously devised to estimate the same parameters [57]. LSQ and regularized algorithms based on DP were previously employed to estimate attenuation and BSCs. LSQ minimizes a cost function based on the squared-difference between the measured backscatter spectrum and a theoretical model to extract the values of the depth-averaged attenuation coefficient and the magnitude and frequency dependence of the BSC. DP follows a similar strategy, but includes a regularization term in the cost function that assumes piece-wise continuity in the values of the depth-averaged attenuation and the magnitude and frequency dependence of the BSC. To reduce the computational burden, the DP strategy stores minimized values of the cost function to avoid recomputing them at each spatial position.

However, the DP method faces three major issues:

- 1) It is a discrete optimization method. This means that the solution is based on minimizing the cost function from a set of discrete values defined by a search range and step size for the acoustic properties. A small step size improves the results by reducing the quantization error at the expense of increasing the computational complexity. This issue is exacerbated when processing a large field of view (i.e., abdominal or obstetric imaging). This limits the real-time applicability of DP. In addition, the step size must be defined by the user, adding to the complexity of its implementation.
- 2) A search range must be defined by the user. If ranges of values for the parameters of interest are not available for the tissue under study, a very large search range should be used, which further increases the computational complexity.
- 3) A fundamental problem of DP is that the graph formed by regularization costs must be a tree, and cannot have a cycle. As such, DP cannot consider the entire data. In other words, DP is applied

on a 2D (axial vs lateral) array of power spectra but considers regularization only over depth for each lateral location independent from the others.

Some of the recent work performed by other groups to improve QUS parameters is as follows: Destrempes *et al.* [52] optimized a generalized least absolute shrinkage and selection operator (LASSO) problem using a Lagrangian multiplier in addition to the Bayesian Information Criterion for estimating attenuation and scatterer properties to improve the contrast-to-noise ratio (CNR) on the difference in acoustic concentration. There is an interest in estimating coefficients related to distinct organs in the body. Deeba *et al.* [58] focused on diagnosing liver steatosis. They presented a cost function entailing total variation regularization to estimate effective scatterer diameter (ESD) and acoustic concentration (AC). They did not propose a new optimization algorithm but used MATLAB's convex optimization toolbox CVX [59] to solve the optimization problem. Rafati *et al.* [60] proposed a technique that can be used in diagnosing multiple liver diseases. They proposed a method to estimate the attenuation coefficient map using the attenuation coefficient slope. Accordingly, they approximated the logarithmic scale of the power spectra at each frequency as a function of depth. Consequently, the frequency where the maximum y-intercept occurred was selected for calculating the local attenuation coefficient slope. Afterward, the frequency range was limited to those where the ratio of the normalized power spectra with respect to the depths at two locations and two adjacent frequencies was within 25% of the estimated local attenuation coefficient slope. The ultimate estimate of the local attenuation coefficient slope was calculated using a linear regression on the confined frequency range. The use of  $L2$  norms in cost functions gained popularity since they are differentiable. Birdi *et al.* [61] introduced an analytical regularized based method using  $L2$  norms. The method directly estimates local attenuation providing a physical-based model, and as opposed to previous works, it couples the coefficients at all depth points. Additionally, performing this technique prevents post-processing computation for mapping effective attenuation to the local attenuation. The method is shown to outperform the traditional spectral log difference method. Furthermore, to exploit the advantages of the  $L1$  norm, the authors proposed a weighted  $L2$  norm scheme that can iteratively approximate the  $L1$  norm.

Oelze *et al.* [62] improved the estimation of ESD by weighting the low signal-to-noise ratio (SNR) part of the power spectra. Lavarello *et. al* [63] established three algorithms to estimate ESD based on a comparison between estimated BSC and the fluid-sphere scattering model. The authors

explained that the estimator can have a significant role in estimating ESD as well. Furthermore, similar to their previous work [64], they concluded that modeling a medium with a single scatterer size is not in accordance with the physical properties of the medium. Moreover, Nordberg *et al.* [65] proved when a medium contains scattering sources with a variety of sizes, a single scatterer size cannot accurately characterize that medium.

### ***1.2.2 Clinical Applications***

QUS potentially allows determining tissue characteristics and diagnose diseases objectively and noninvasively. Assessment of renal microstructure [4], [19], [20], fat infiltration [21], [24], structural evaluation of the uterine cervix during pregnancy [25, 26], cancer therapy monitoring and assessment [27], [28], fatty liver classification [76], [77], prostate cancer imaging [78], bone assessment [79], and breast cancer monitoring [80] are a few examples of clinical applications of QUS parameters. Besides, recent advances in ultrasound manufacturing have enabled the characterization and imaging of tissues based on sound speed, attenuation, and backscattering [2].

## **1.3 Thesis Statement**

In addition to testing new clinical applications, growing attention has focused on improving QUS techniques. Recent work has demonstrated that the accuracy and precision of QUS parameters can be improved by exploiting the regularized-based techniques [50]–[56], [60]. Accordingly, our focus is mainly on introducing regularized techniques for improving the estimation of QUS parameters.

## **1.4 List of Publications**

- **Journal Papers**

1. N Jafarpisheh, L. C Martinez, H Whitson, I. M Rosado-Mendez, and H Rivaz, “Physics-Inspired Regularized Pulse-Echo Quantitative Ultrasound: Efficient Optimization with ADMM”, IEEE Transactions on Ultrasonics, Ferroelectrics, and Frequency Control, Major revision requested, 2022.

2. N Jafarpisheh, I. M Rosado-Mendez, and H Rivaz, “Scatterer Size Distribution Estimation in Quantitative Ultrasound using Constrained Optimization”, Ultrasonic Imaging, Under Review 2022.

3. N Jafarpisheh, T J Hall, H Rivaz, and I M Rosado-Mendez, “Analytic Global Regularized Backscatter Quantitative Ultrasound”, IEEE Transactions on Ultrasonics, Ferroelectrics, and Frequency Control, 2021.

- **Conference Papers**

1. N Jafarpisheh, L. C Martinez, H. Whitson, I. M. Rosado-Mendez, and H. Rivaz, “Adaptive Weighting Strategy in Regularized Quantitative Ultrasound”, IEEE IUS 2022, Venice, Italy.

2. H Whitson, N Jafarpisheh, H. Rivaz, I Rosado-Mendez, and T J. Hall, “Comparative Performance of 1D and 2D Regularized Quantitative Ultrasound for Curvilinear Transducers in the Presence of Aberration Induced Clutter”, IEEE IUS 2022, Venice, Italy.

3. N Jafarpisheh, I. M Rosado-Mendez, and H Rivaz, Regularized Constrained Optimization of Scatterer Size Distribution Estimation in Quantitative Ultrasound”, International Symposium on Ultrasonic Imaging and Tissue Characterization (UITC) 2022.

4. N Jafarpisheh, I M Rosado-Mendez, T J Hall, and H Rivaz, “Two Novel Techniques to Estimate the Contribution of Each Scatterer Size in Quantitative Ultrasound”, International Symposium on Ultrasonic Imaging and Tissue Characterization (UITC) 2021.

5. N Jafarpisheh, T J Hall, H Rivaz, and I M Rosado-Mendez, “Analytic Global Regularized Backscatter Quantitative Ultrasound”, International Symposium on Ultrasonic Imaging and Tissue Characterization (UITC) 2021.

6. N Jafarpisheh, I M Rosado-Mendez, T J Hall, and H Rivaz, “Estimation of the Scatterer Size Distributions in Quantitative Ultrasound Using Constrained Optimization”, IEEE IUS, 2021.

7. N Jafarpisheh, I M Rosado-Mendez, T J Hall, and H Rivaz, “Analytical Globally-Regularized Estimation Of Effective Scatterer Diameter And Acoustic Concentration in Quantitative Ultrasound”, IEEE 18th International Symposium on Biomedical Imaging (ISBI), 2021.

8. N Jafarpisheh, I M Rosado-Mendez, T J Hall, and H Rivaz, "Evaluation of Contrast-to-Noise Ratio of Parametric Images of Regularized Estimates of Quantitative Ultrasound Parameters", IEEE IUS Conference, 2020.

9. N Jafarpisheh, I M Rosado-Mendez, T J Hall, and H Rivaz, "Regularized Estimation of Effective Scatterer Size and Acoustic Concentration Quantitative Ultrasound Parameters Using Dynamic Programming", IEEE EMBC Conference, 2020.

10. N Jafarpisheh, I M Rosado-Mendez, T J Hall, and H Rivaz, "Estimation of Effective Scatterer Size and Acoustic Concentration Quantitative Ultrasound Parameters Using Dynamic Programming", XVI Mexican Symposium on Medical Physics, 2020.

## Chapter 2

# Analytic Global Regularized Backscatter Quantitative Ultrasound

This chapter is published in IEEE Trans. UFFC, 2021 and International Symposium on Ultrasonic Imaging and Tissue Characterization (UITC) 2021.

Herein, we propose two novel techniques to accurately and precisely estimate two important QUS parameters, namely the effective attenuation coefficient and the BSC. Both techniques optimize a cost function that incorporates data and continuity constraint terms, which we call AnaLytical Global rEgularized BackscatteR quAntitative ultrasound (ALGEBRA). We propose two versions of ALGEBRA, namely 1D- and 2D-ALGEBRA. In 1D-ALGEBRA, the regularized cost function is formulated in the axial direction, and QUS parameters are calculated for one line of RF echo data. In 2D-ALGEBRA, the regularized cost function is formulated for the entire image, and QUS parameters throughout the image are estimated *simultaneously*. This simultaneous optimization allows 2D-ALGEBRA to “see” all the data before estimating QUS parameters. In both methods, we efficiently optimize the cost functions by casting it as a sparse linear system of equations. As a result of this efficient optimization, a comparison of the running time for one RF line describes that 1D-ALGEBRA and 2D-ALGEBRA are respectively 600 and 300 times faster than optimization using the dynamic programming (DP) method previously proposed by our group. In addition, the proposed technique has fewer input parameters that require manual tuning. Our results demonstrate that the proposed ALGEBRA methods substantially outperform least-squares (LSQ) and DP methods in estimating QUS parameters in phantom experiments.

### 2.1 Background

To cope with the issues in DP method mentioned in Chapter 1, here we propose two versions of a novel technique which we call fast AnaLytical Global rEgularized BackscatteR quAntitative ultrasound, or ALGEBRA. ALGEBRA solves the regularized cost function analytically and does not need search ranges and step sizes. The first version of ALGEBRA, 1D-ALGEBRA, minimizes

exactly the same cost function as DP [56], where 1D refers to regularization in one (axial) direction. The second version is called 2D-ALGEBRA and performs a global regularization in both axial and lateral directions. 1D- and 2D-ALGEBRA are inspired by state of the art regularization strategies used in ultrasound elastography [36, 37]. 1D- and 2D- ALGEBRA are about 600 times and 300 times faster than DP [56], respectively, and also provides more accurate and precise QUS estimates.

## 2.2 Algorithms

The application of ALGEBRA on QUS is based on the reference phantom method (RPM) [83] to provide system- and operator- independent QUS parameter estimation. According to the RPM, the ratio of the power spectrum  $S_s(f, z)$  of a sample  $s$  (phantom or tissue with unknown attenuation coefficient  $\alpha_s$  and BSC  $\sigma_{b,s}$ ) to the power spectrum  $S_r(f, z)$  of a reference phantom  $r$  (with known  $\alpha_r$  and  $\sigma_{b,r}$ , and similar sound speed to the sample, and where subscript  $r$  indicates “reference”) [84] can be modeled as:

$$\frac{S_s(f; z, x)}{S_r(f; z)} = \frac{\sigma_{b,s}(f; z, x)A_s(f; z, x)}{\sigma_{b,r}(f)A_r(f, z)} \quad 2-1$$

where  $f$ ,  $z$ , and  $x$  are frequency, depth, and lateral position, respectively. The factor  $A$  accounts for total attenuation of the acoustic pulse from the transducer to depth  $z$ :

$$\exp\left(-4 \int_0^z \alpha(f; z', x) dz'\right) \quad 2-2$$

where  $\alpha$  is in  $\text{Np.cm}^{-1}$ . Assuming that the attenuation coefficient varies linearly with frequency [56], i.e.,  $\alpha(f; z, x) = \alpha_0(z, x)f$ , where  $\alpha_0$  in  $\text{Np.cm}^{-1} \text{MHz}^{-1}$  is the *specific attenuation* as defined by the International Electrotechnical Commission [85], then Eq. (2-2) can be expressed as:

$$A(f; z, x) = \exp\left(-4f \int_0^z \alpha_0(z', x) dz'\right)$$

$$A(f; z, x) = \exp(-4f \alpha_{eff}(z, x)z)$$

2-3

where  $\alpha_{eff}$  is the *effective attenuation* equal to the average specific attenuation along the propagation depth  $z$ .

$$\alpha_{eff}(z, x) = \int_0^z \alpha_0(z', x) dz'$$

2-4

In the case of the homogeneous reference, the effective attenuation  $\alpha_{eff}$  [ $\text{cm}^{-1} \text{MHz}^{-1}$ ] is equal to its local attenuation coefficient  $\alpha_{0,r}$ . Note that  $\alpha$ ,  $\alpha_0$ , and  $\alpha_{eff}$  can also be expressed in  $\text{dB cm}^{-1}$  or  $\text{dB cm}^{-1} \text{MHz}^{-1}$  by multiplying their numerical value by 8.686.

We employ a power law model to parameterize the frequency dependence of  $\sigma_b(f; z, x)$  as follows:

$$\sigma_b(f; z, x) = \beta(z, x) f^{\nu(z, x)}$$

2-5

where  $\beta$  and  $\nu$  indicate the value of the BSC at 1MHz and its frequency dependence, respectively. After substituting Eqs. (2-2)-(2-4) into (2-1) and taking the natural logarithm from both sides similar to [56], we have:

$$X(f; z, x) = \ln\left(\frac{S_s(f; z, x)}{S_r(f; z, x)}\right) = -4a(z, x) f z + b(z, x) + n(z, x) \ln f$$

2-6

where

$$a(z, x) = \alpha_{eff}(z, x) - \alpha_{0,r}$$

$$b(z, x) = \ln\beta_s(z, x) - \ln\beta_r,$$

$$n(z, x) = \nu_s(z, x) - \nu_r.$$

2-7

Both 1D- and 2D-ALGEBRA make use of a cost function containing a data term,  $D$ , and a regularization term,  $R$ :

$$C = D + R.$$

2-8

### 2.2.1 1D-ALGEBRA

The ALGEBRA methods are applied to an  $N_R \times N_C \times N_F$  power spectra matrix, where  $N_R$  is the number of rows corresponding to different axial positions,  $N_C$  is the number of columns corresponding to different lateral positions, and  $N_F$  is the number of frequency bins within a useable frequency range. In 1D-ALGEBRA, one column (or lateral position) of power spectra is considered and regularization is performed in the axial direction to estimate  $a$ ,  $b$ , and  $n$  at different axial positions along that column. In 2D-ALGEBRA, the entire array of power spectra is used in a 2D regularization strategy.

Removing the  $x$  dependence in (2-5), data and regularization terms  $D$  and  $R$  in 1D-ALGEBRA are defined as follows:

$$D = \sum_{l=1}^{N_F} \sum_{i=1}^{N_R} (X(f_l, z_i) - b_i - n_i \ln(f_l) + 4a_i f_l z_i)^2$$

2-9

$$R = \sum_{p=1}^3 \sum_{i=2}^{N_R} w_p (p_i - p_{i-1})^2$$

2-10

where  $i$  and  $l$  refer axial location and frequency indices, respectively. Index  $p$  refers to the three parameters ( $p=1$  for  $a$ , 2 for  $b$ , and 3 for  $n$ ) and  $w_p$  is the regularization weight for parameter  $p$ .

As Figure 2-1(a) and Eq. (2-10) show, regularization is employed in the axial direction. To obtain the optimum parameters, we calculate the partial derivatives of the cost function with respect to  $a_i$ ,  $b_i$ , an  $n_i$  and set them to zero. After some manipulations, we arrive at a set of simple linear equation as follows:

$$UY=T.$$

2-11

$\mathbf{Y}$  is a column vector with  $3N_R$  components containing the parameters to be estimated at different depths, i.e.,  $a_i, b_i,$  an  $n_i$ :

$$\mathbf{Y} = [a_1, \dots, a_{N_R}, b_1, \dots, b_{N_R}, n_1, \dots, n_{N_R}]^T,$$

2-12

where superscript T indicates transposition.  $\mathbf{U}$  is a  $3N_R \times 3N_R$  matrix which can be separated into two  $3N_R \times 3N_R$  matrices named  $\mathbf{C}$  and  $\mathbf{W}$ :

$$\mathbf{U} = \mathbf{C} + \mathbf{W}.$$

2-13

Matrix  $\mathbf{C}$  is formed of 6 component matrices:

$$\mathbf{C} = \begin{bmatrix} \mathbf{C}_1 & \mathbf{C}_2 & \mathbf{C}_3 \\ \mathbf{C}_2 & \mathbf{C}_4 & \mathbf{C}_5 \\ \mathbf{C}_3 & \mathbf{C}_5 & \mathbf{C}_6 \end{bmatrix}$$

2-14

and  $\mathbf{C}_j, j = 1, \dots, 6,$  are  $N_R \times N_R$  diagonal matrixes:

$$\mathbf{C}_1 = (16 \sum_{l=1}^{N_F} f_l^2) \mathbf{Z}_2, \quad \mathbf{C}_2 = (-4 \sum_{l=1}^{N_F} f_l) \mathbf{Z}_1,$$

$$\mathbf{C}_3 = (-4 \sum_{l=1}^{N_F} f_l \ln f_l) \mathbf{Z}_1, \quad \mathbf{C}_4 = (N_F) \mathbf{I},$$

$$\mathbf{C}_5 = \left( \sum_{l=1}^{N_F} \ln f_l \right) \mathbf{I}, \quad \mathbf{C}_6 = \left( \sum_{l=1}^{N_F} (\ln f_l)^2 \right) \mathbf{I}$$

2-15

where  $\mathbf{I}$  is the  $N_R \times N_R$  identity matrix and

$$\mathbf{z}_1 = \begin{bmatrix} z_1 & 0 & \dots & 0 \\ 0 & z_2 & \dots & 0 \\ \vdots & \vdots & \ddots & \vdots \\ 0 & 0 & \dots & z_{N_R} \end{bmatrix}, \quad \mathbf{z}_2 = \begin{bmatrix} z_1^2 & 0 & \dots & 0 \\ 0 & z_2^2 & \dots & 0 \\ \vdots & \vdots & \ddots & \vdots \\ 0 & 0 & \dots & z_{N_R}^2 \end{bmatrix}.$$

2-16

Matrix  $\mathbf{W}$  is defined as:

$$\mathbf{W} = \begin{bmatrix} \mathbf{W}_a & \mathbf{0} & \mathbf{0} \\ \mathbf{0} & \mathbf{W}_b & \mathbf{0} \\ \mathbf{0} & \mathbf{0} & \mathbf{W}_n \end{bmatrix}$$

2-17

where  $\mathbf{W}_a$ ,  $\mathbf{W}_b$ , and  $\mathbf{W}_n$  are  $N_R \times N_R$  matrices given by:

$$\mathbf{W}_p = w_p \mathbf{B}$$

2-18

where

$$\mathbf{B} = \begin{bmatrix} 1 & -1 & 0 & 0 & \dots & 0 \\ -1 & 2 & -1 & 0 & \dots & 0 \\ 0 & -1 & 2 & -1 & \dots & 0 \\ \vdots & \vdots & \vdots & \vdots & \ddots & \vdots \\ 0 & 0 & 0 & \dots & -1 & 1 \end{bmatrix}$$

and  $\mathbf{0}$  is a  $N_R \times N_R$  matrix with zero elements.

$\mathbf{T}$  in (11) is a  $3N_R$  vector containing three vertically-concatenated  $N_R \times 1$  column vectors,  $\mathbf{T1}$ ,  $\mathbf{T2}$ , and  $\mathbf{T3}$  as follows:

$$\mathbf{T} = \begin{bmatrix} \mathbf{T1} \\ \mathbf{T2} \\ \mathbf{T3} \end{bmatrix},$$

2-19

whose  $i^{\text{th}}$  components are given by:

$$\begin{aligned} T1_i &= -4z_i \sum_{l=1}^{N_F} X(f_l, z_i) f_l, \\ T2_i &= \sum_{l=1}^{N_F} X(f_l, z_i), \\ T3_i &= \sum_{l=1}^{N_F} X(f_l, z_i) \ln f_l. \end{aligned}$$

2-20

The values of  $a_i$ ,  $b_i$ , an  $n_i$  at different depths are obtained by solving (11) for  $\mathbf{Y}$ .

### 2.2.2 2D-ALGEBRA

In 2D-ALGEBRA, we have similar data and regularization terms:

$$D = \sum_{l=1}^{N_F} \sum_{i=1}^{N_R} \sum_{j=1}^{N_C} (X(f_l, z_i, x_j) - b_{i,j} - n_{i,j} \ln(f_l) + 4a_{i,j} f_l z_i)^2$$

2-21

$$R = \sum_{p=1}^3 \sum_{i=2}^{N_R} \sum_{j=2}^{N_C} w_{p,z} (p_{i,j} - p_{i-1,j})^2 + w_{p,x} (p_{i,j} - p_{i,j-1})^2$$

2-22

where  $j$  refers to the lateral location index. The indices of the regularization weights indicate ( $z$ ) axial and ( $x$ ) lateral directions. Thus, as Eq. (2-22) shows, the regularization is employed in both axial ( $z$ ) and lateral ( $x$ ) directions (Figure 2-1(b)). As axial and lateral parameters are coupled together, optimization should be performed on the whole image, not separately for each direction.

For the 2D regularization the components of  $\mathbf{C}$  have different sizes ( $N_R N_C \times N_R N_C$ ) as each component should also include lateral coefficient parameters. Therefore, the size of  $\mathbf{C}$  will be  $3N_R N_C \times 3N_R N_C$ . The matrix components of  $\mathbf{W}_2$  are defined as follows:

$$\mathbf{W}_2 = \begin{bmatrix} \mathbf{W}_{a_2} & \mathbf{0} & \mathbf{0} \\ \mathbf{0} & \mathbf{W}_{b_2} & \mathbf{0} \\ \mathbf{0} & \mathbf{0} & \mathbf{W}_{n_2} \end{bmatrix}$$

2-23

where

$$\mathbf{W}_{p_2} = \mathbf{V} + \boldsymbol{\rho} .$$

2-24

$\mathbf{V}$  is a  $N_R N_C \times N_R N_C$  matrix defined as

$$\mathbf{V} = \begin{bmatrix} \mathbf{V}_1 & 0 & \cdots & 0 \\ 0 & \mathbf{V}_2 & 0 & 0 \\ 0 & 0 & \ddots & 0 \\ 0 & \cdots & 0 & \mathbf{V}_{N_C} \end{bmatrix}$$

2-25

where  $\mathbf{V}_1, \mathbf{V}_2, \dots, \mathbf{V}_{N_C}$  are  $N_R \times N_R$  matrices, and  $\mathbf{V}_2 = \mathbf{V}_3 = \cdots = \mathbf{V}_{N_C-1}$ :

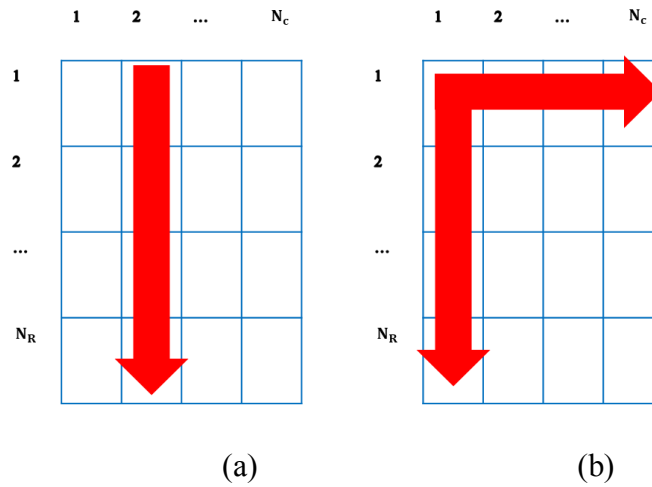


Figure 2-1 Regularization strategies for (a) 1D- and (b) 2D-ALGEBRA.

$$\mathbf{V}_1 = \begin{bmatrix} w_{p,z} + w_{p,x} & 0 & \cdots & 0 \\ 0 & 2w_{p,z} + w_{p,x} & \ddots & \vdots \\ \vdots & \vdots & \ddots & \vdots \\ 0 & 0 & \cdots & w_{p,z} + w_{p,x} \end{bmatrix}$$

2-26

$$\mathbf{V}_2 = \begin{bmatrix} w_{p,z} + 2w_{p,x} & 0 & \cdots & 0 \\ 0 & 2w_{p,z} + 2w_{p,x} & \ddots & \vdots \\ \vdots & \vdots & \ddots & \vdots \\ 0 & 0 & \cdots & w_{p,z} + 2w_{p,x} \end{bmatrix}$$

2-27

$$\mathbf{V}_{N_C} = \begin{bmatrix} w_{p,z} + w_{p,x} & 0 & \cdots & 0 \\ 0 & 2w_{p,z} + w_{p,x} & \ddots & \vdots \\ \vdots & \vdots & \ddots & \vdots \\ 0 & 0 & \cdots & w_{p,z} + w_{p,x} \end{bmatrix}$$

2-28

In (26) to (28), except for the first and last elements, all the elements of the main diagonal are repeated  $N_R - 2$  times. The size of matrix  $\boldsymbol{\rho}$  in Eq. (29) is  $N_R N_C \times N_R N_C$  same as  $\mathbf{V}$ . The formulation of  $\boldsymbol{\rho}$  is as follows:

$$\boldsymbol{\rho} = \begin{bmatrix} \mathbf{m1} & \mathbf{m2} & \mathbf{0} & \mathbf{0} \\ \mathbf{m2} & \mathbf{m1} & \ddots & \mathbf{0} \\ \mathbf{0} & \ddots & \ddots & \mathbf{m2} \\ \mathbf{0} & \mathbf{0} & \mathbf{m2} & \mathbf{m1} \end{bmatrix}$$

2-29

where  $\mathbf{m1}$  and  $\mathbf{m2}$  are  $N_R \times N_R$  matrices as follows. Matrix  $\mathbf{m1}$  is repeated  $N_C$  times and matrix  $\mathbf{m2}$  is repeated  $N_C - 1$  times in each direction to form  $\boldsymbol{\rho}$ .

$$\mathbf{m1} = \begin{bmatrix} 0 & -w_{p,z} & 0 & \cdots & 0 \\ -w_{p,z} & 0 & \ddots & \cdots & \cdots \\ 0 & \ddots & \ddots & \ddots & 0 \\ \vdots & \cdots & -w_{p,z} & \ddots & -w_{p,z} \\ 0 & 0 & 0 & -w_{p,z} & 0 \end{bmatrix}$$

2-30

$$\mathbf{m2} = \begin{bmatrix} -w_{p,x} & 0 & \cdots & 0 \\ 0 & \ddots & 0 & \vdots \\ \vdots & 0 & \ddots & 0 \\ 0 & \cdots & 0 & -w_{p,x} \end{bmatrix}$$

2-31

Again, index  $p$  refers to the three parameters ( $p=1$  for  $a$ , 2 for  $b$ , and 3 for  $n$ ). It is important to note that Eq. (24) has the same functional form for the three parameters  $a$ ,  $b$  and  $n$  because it is expressed in terms of index  $p$ . However, the actual values of the matrix  $\mathbf{W}_{p_2}$  are different for different values of  $p$  due to the different values of the weights  $w_{p_1}$  and  $w_{p_2}$ . Here, we also have a similar  $\mathbf{T}$  vector but with  $3N_R N_C$  elements. After solving a similar equation to (2-11), we will solve for all  $3N_R N_C$  parameters.

## 2.3 Methods

### 2.3.1 Tissue-mimicking phantoms

1D- and 2D-ALGEBRA were tested to data acquired from five tissue mimicking phantoms with the following properties:

- Phantom A: Uniform
  - $\alpha_{0,s} = 0.654 \text{ dB cm}^{-1} \text{ MHz}^{-1}$
  - $\beta_s = 1.02 \times 10^{-6} \text{ cm}^{-1} \text{ sr}^{-1} \text{ MHz}^{-\nu}$
  - $\nu_s = 4.16$
  - $\sigma_{b,s}(6.6\text{MHz})=2.62 \times 10^{-3} \text{ cm}^{-1} \text{ sr}^{-1}$
- Phantom B: Reference for Phantom A
  - $\alpha_{0,s} = 0.670 \text{ dB cm}^{-1} \text{ MHz}^{-1}$
  - $\beta_s = 8.79 \times 10^{-6} \text{ cm}^{-1} \text{ sr}^{-1} \text{ MHz}^{-\nu}$
  - $\nu_s = 3.14$
  - $\sigma_{b,s}(6.6\text{MHz})=3.29 \times 10^{-3} \text{ cm}^{-1} \text{ sr}^{-1}$
- Phantom C: Attenuation step

Top and bottom layers:

  - $\alpha_{0,s} = 0.510 \text{ dB cm}^{-1} \text{ MHz}^{-1}$
  - $\beta_s = 1.60 \times 10^{-6} \text{ cm}^{-1} \text{ sr}^{-1} \text{ MHz}^{-\nu}$
  - $\nu_s = 3.52$
  - $\sigma_{b,s}(8.9\text{MHz})=3.52 \times 10^{-3} \text{ cm}^{-1} \text{ sr}^{-1}$

Middle layer:

- $\alpha_{0,s} = 0.779 \text{ dB cm}^{-1} \text{ MHz}^{-1}$
- $\beta_s = 3.22 \times 10^{-6} \text{ cm}^{-1} \text{ sr}^{-1} \text{ MHz}^{-\nu}$
- $\nu_s = 3.13$
- $\sigma_{b,s}(8.9\text{MHz})=3.02 \times 10^{-3} \text{ cm}^{-1} \text{ sr}^{-1}$

- Phantom D: Backscatter step

Top and bottom layers

- $\alpha_{0,s} = 0.554 \text{ dB cm}^{-1} \text{ MHz}^{-1}$
- $\beta_s = 4.82 \times 10^{-7} \text{ cm}^{-1} \text{ sr}^{-1} \text{ MHz}^{-\nu}$
- $\nu_s = 3.80$
- $\sigma_{b,s}(8.9\text{MHz})=3.52 \times 10^{-3} \text{ cm}^{-1} \text{ sr}^{-1}$

Middle layer

- $\alpha_{0,s} = 0.58 \text{ dB} \cdot \text{cm}^{-1} \text{ MHz}^{-1}$
- $\beta_s = 3.94 \times 10^{-6} \text{ cm}^{-1} \text{ sr}^{-1} \text{ MHz}^{-\nu}$
- $\nu_s = 3.38$
- $\sigma_{b,s}(8.9\text{MHz})=6.37 \times 10^{-3} \text{ cm}^{-1} \text{ sr}^{-1}$

- Phantom E: Inclusion phantom (Gammex 410SCG phantom (Gammex-SunNuclear, Middleton, WI)):

Background

- $\alpha_{0,s} = 0.5 \text{ dB cm}^{-1} \text{ MHz}^{-1}$
- $\beta_s = 2.997 \times 10^{-6} \text{ cm}^{-1} \text{ sr}^{-1} \text{ MHz}^{-\nu}$
- $\nu_s = 3.34$
- $\sigma_{b,s}(8\text{MHz})=3.11 \times 10^{-3} \text{ cm}^{-1} \text{ sr}^{-1}$

Inclusions

- Three 8mm-diameter cylindrical inclusions with +12, +6 and -6dB scattering with respect to the background

More details about the composition of phantoms A-D are available in [34, 40].

Phantom A comprises a water-based agarose-propylene combined with filtered milk. Phantom B is composed of water-based agarose added by graphite powder. Both phantoms contain glass-beads with 5-43 $\mu\text{m}$  diameter as the source of scattering. The ground truth values were obtained with

single element transducers to measure attenuation and BSC utilizing narrowband substitution and broadband pulse-echo techniques, respectively [41, 42].

Phantoms C (uniform BSC) and D (uniform attenuation) are water-based phantoms with three layer phantoms composed of mixtures of gelatin and unfiltered milk. The concentration of scatterers in phantom C is 4g/L in all parts, while in phantom D the concentration of scatterers in the second layer is 8g/L which is 4 times more than the other two layers. On the other hand, molten gelatin and unfiltered milk have been mixed with the ratio of 2.1:1 in all layers in phantom D. This ratio in the middle layer of phantom C is 1:1 to increase its attenuation with respect to the first and third layer, where the ratio is 2.85:1 [84].

### **2.3.2 Data Acquisition**

- **Homogenous Phantom**

Two phantoms (A and B above) were scanned with a 9L4 linear array transducer on a Siemens Acuson S3000 (Issaquah, WA) scanner operated at a 6.6MHz nominal center frequency to obtain 10 uncorrelated frames of RF data for each phantom [56]. Phantom B was used as reference for the characterization of phantom A. RF data was accessed through the Axis Direct Research Interface [41].

- **Layered Phantoms**

10 uncorrelated frames of RF data were acquired from Phantoms C and D, using their top layers as references. Both phantoms were scanned using a linear array transducer on a Siemens Acuson S2000 scanner operated at an 8.9MHz center frequency [36].

- **Different Echogenicity Phantom (Gammex phantom)**

Phantom E was scanned using a Verasonics Vantage 128 system (Verasonics, Kirkland, WA) with a L11-5v transducer operated at 8MHz to obtain 10 uncorrelated frames of RF data. Uncorrelated frames from a homogeneous region of the same phantom were used as reference.

### 2.3.3 Power Spectra Estimation

We applied LSQ, DP, 1D- and 2D-ALGEBRA to 10 independent frames of RF echo data from each phantom. Parameter estimation regions of size 4mm×4mm were swept axially and laterally over each frame with an overlap of 85%, computing at each position the echo signal power spectrum using a multi-taper approach [88]. This procedure resulted in power spectra matrices with 40 columns and 74 rows in the uniform phantom, 86 columns and 108 rows in the layered phantoms, and 55 columns and 103 rows in Phantom E.

We have solved LSQ analytically. To apply DP, the following search ranges were used:

$$\frac{\alpha_{s\_min} - \alpha_r - 0.5}{8.686} < a < \frac{\alpha_{s\_max} - \alpha_r + 0.5}{8.686}$$

$$\log_{0.1} \frac{\beta_{s\_min}}{\beta_r} < b < \log_{10} \frac{\beta_{s\_max}}{\beta_r}$$

$$\nu_{s\_min} - \nu_r - 2 < n < \nu_{s\_max} - \nu_r + 2$$

where *min* and *max* indices refer to the minimum and maximum ground truth values in the layered phantoms. These values were the same in the uniform phantom.

Tables 2-1(a) and (b) show the regularization weights in each method. The weights of 1D-ALGEBRA are same as DP. The first and second elements of 2D-ALGEBRA weights correspond to the axial and lateral regularizations, respectively. In each method, first, the algorithm was executed using weights in order of 10. Then, considering the results, the weights were increased or decreased. The weights were increased when we saw a high variance in results, in other words when results were close to LSQ. On the other hand, weights were decreased when results were approaching a flat line. The values included in Table 2-1(a) and (b) are the final ones.

Table 2-1(a) Regularization Weights in Four Phantoms, DP method

DP			
Phantom	$w_\alpha$	$w_b$	$w_n$
A	$10^{12}$	$10^8$	$10^8$
C	$7 \times 10^6$	$10^1$	$6 \times 10^4$
D	$7 \times 10^8$	$3 \times 10^1$	$10^4$
E	$8 \times 10^2$	$8 \times 10^2$	$8 \times 10^2$

Table 2-1(b) Regularization Weights in Four Phantoms, 2D-ALGEBRA method

2D-ALGEBRA						
Phantom	$w_\alpha$		$w_b$		$w_n$	
A	$[10^{10}$	$10^{10}]$	$[10^8$	$10^8]$	$[10^8$	$10^8]$
C	$[7 \times 10^6$	$10^9]$	$[10^1$	$10^1]$	$[6 \times 10^4$	$6 \times 10^4]$
D	$[7 \times 10^8$	$7 \times 10^8]$	$[3 \times 10^1$	$3 \times 10^1]$	$[10^4$	$10^4]$
E	$[4 \times 10^2$	$4 \times 10^2]$	$[4 \times 10^2$	$4 \times 10^2]$	$[4 \times 10^2$	$4 \times 10^2]$

It can be easily shown that a symmetric diagonal dominant matrix, where its diagonal entries are positive, is a positive definite matrix. In addition, according to a theorem in linear algebra [89], the unique solution for equation  $\mathbf{Ax} = \mathbf{b}$  exists if and only if  $\mathbf{A}$  (here, matrix  $\mathbf{U}$ ) is full rank. Therefore, as  $\mathbf{U}$  is full rank, the unique solution exists. 1D- and 2D-ALGEBRA were implemented in Matlab R2018a (MathWorks, USA).

To obtain  $\mathbf{Y}$  in Eq. (2-11), we use the mldivide function "\" in Matlab. This operator is time efficient and provides two algorithms for full and sparse inputs [90].

## 2.4 Results

- **Phantom A**

Figure 2-2(a) shows the mean and the standard deviation (error bars) of the attenuation coefficient ( $\alpha_s$ ) vs. depth obtained from the 400 estimates using DP (green), 1D-ALGEBRA (blue), and 2D-ALGEBRA (red). The black dash line refers to the expected values. While 1D-ALGEBRA resulted in larger standard deviation compared to DP, the standard deviation obtained with 2D-ALGEBRA was close to that of DP.

In Figure 2-2(b), the BSC is reconstructed from the average values of the 400 estimates of  $\beta_s$  and  $\nu_s$ . It can be observed that the bias of estimation using 1D- and 2D-ALGEBRA is lower than LSQ and DP.

Figure 2-3 shows the B-mode image of the phantom and parametric images of the reconstructed BSC evaluated at 6.6MHz in dB scale with respect to  $10^{-4} \text{ cm}^{-1} \text{ sr}^{-1}$  using LSQ, DP, 1D- and 2D-ALGEBRA. In all phantoms, the range of color bar corresponds to the range of values obtained with DP. Visual comparison confirms that 1D- and 2D-ALGEBRA have the most similarity to ground truth compared to DP and LSQ. Quantitative analysis of bias and variance of BSC at center frequency reveals that using 1D-ALGEBRA leads to 98% decrease in variance and 39% in bias respect to DP. In addition, using 2D-ALGEBRA results in 100% and 35% reduction in variance and bias, respectively.

To estimate the QUS parameters in an image with  $N_C = 74$  and  $N_R = 40$  using 1D- and 2D-ALGEBRA required 4 and 8 sec, respectively. In comparison, a Matlab implementation of DP required 2400 second for the same problem.

- **Phantoms C and D**

Figure 2-4(a) and 2-4(b-d) show the average and standard deviation (error bars) over 860 estimates of  $\alpha_{eff}$  for Phantom C (attenuation step) and the results of the reconstruction of the BSC from the average values of  $\beta_s$  and  $\nu_s$  in each layer using Eq. (2-2 to 2-5), respectively. In these Figures, the black dashed line is the expected value of the parameter. In the case of the effective attenuation (Figure 2-4(a)), there is a smooth transition from the top to the middle layer to do the averaging effect of Eq. (2-4). Also, the standard deviation of DP is lower than 1D-ALGEBRA. On the other hand, Figure 2-5 reveals that the step size in DP had not been small enough as we see each layer

is not distinguished well. Here, to show how different layers are distinguished, we created a parametric image of the local attenuation ( $\alpha_{local}$ ). The following equation shows how  $\alpha_{local}$  is obtained from  $\alpha_{eff}$ :

$$\alpha_{local}(i) = \frac{\alpha_{eff}(i)z_i - \alpha_{eff}(i-1)z_{i-1}}{z_i - z_{i-1}}$$

2-32

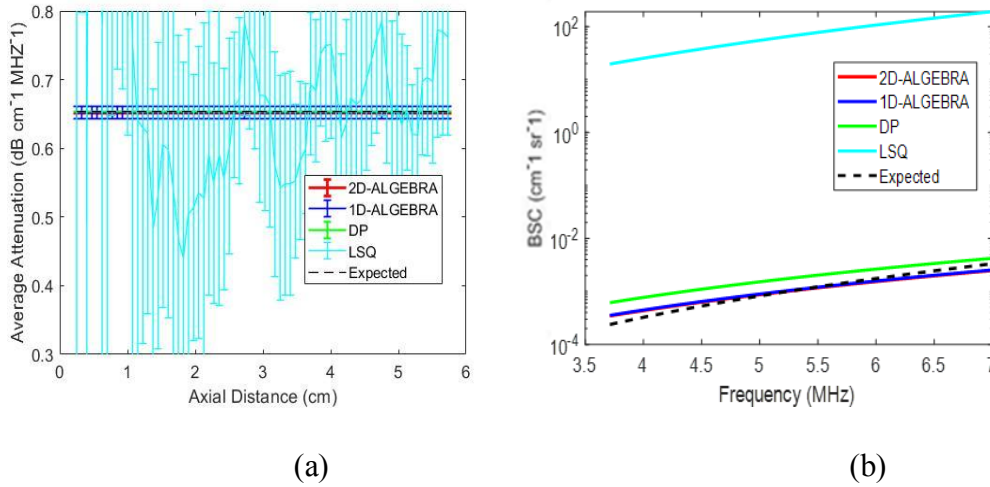


Figure 2-2 Results of 1D-ALGEBRA (blue), 2D-ALGEBRA (red), DP (green), and LSQ (cyan) in phantom A (uniform). The error bars show the standard deviation over the 400 samples for attenuation coefficient (a) and reconstructed BSC averaged over 400 samples (b). In (a), blue, red, cyan and black are superimposed. The black dashed line is the GT.

Figure 2-5(f) demonstrates that using 2D-ALGEBRA,  $\alpha_{local}$  estimation agrees well with ground truth. The analysis of bias and variance of local attenuation shows that 1D- and 2D-ALGEBRA yield 81% reduction in bias. The variance of DP results is small, but it should not be misinterpreted as we see the parametric image of DP is far from the ground truth. This is evidence of the drawbacks of DP referred to in the introduction section.

To estimate the QUS parameters in an image with  $N_C = 108$  and  $N_R = 86$  required 6 and 12 sec, respectively. In comparison, a Matlab implementation of DP required 3600 sec for the same problem.

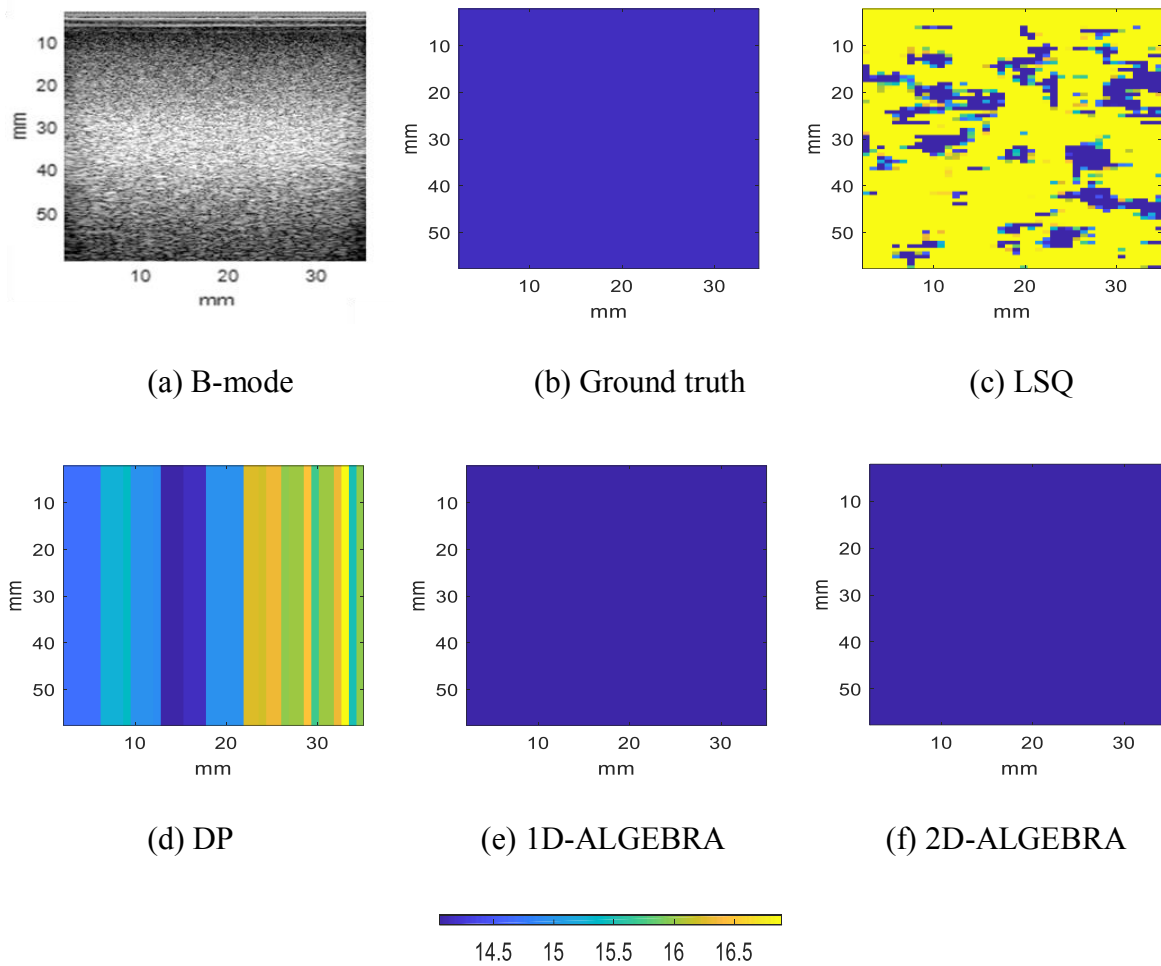


Figure 2-3 Parametric images of the BSC at the center frequency in phantom A (uniform). Results are shown on a dB scale with respect to  $10^{-4} \text{ cm}^{-1} \text{ sr}^{-1}$ . The colorbar shows BSC at the center frequency.

Figure 2-6(a) shows the error bars over 860 estimate of  $\alpha_{eff}$  for phantom D (backscatter step) and Figure 2-6(d) shows results of the reconstruction of the BSC from the average values of  $\beta_s$  and  $\nu_s$  in each layer.

Figure 2-7. shows the B-mode (a) and ground truth (b) as well as parametric images of BSC obtained at the center frequency using LSQ (c), DP (d), 1D (e)- and 2D-ALGEBRA (f) in phantom D (backscatter step). Visual assessment confirms that 1D- and 2D-ALGEBRA outperform other methods. Quantitative assessments of BSC at central frequency disclose 88% reduction in variance as well as 56% in bias using 1D-ALGEBRA compared to DP. In addition, using 2D-ALGEBRA leads to 99% and 55% decrease in variance and bias compared to DP, respectively.

To estimate the QUS parameters in an image with  $N_C = 108$  and  $N_R = 86$  with 1D- and 2D-ALGEBRA took 9 and 18 sec, respectively. In comparison, a Matlab implementation of DP took 5400 second for the same problem.

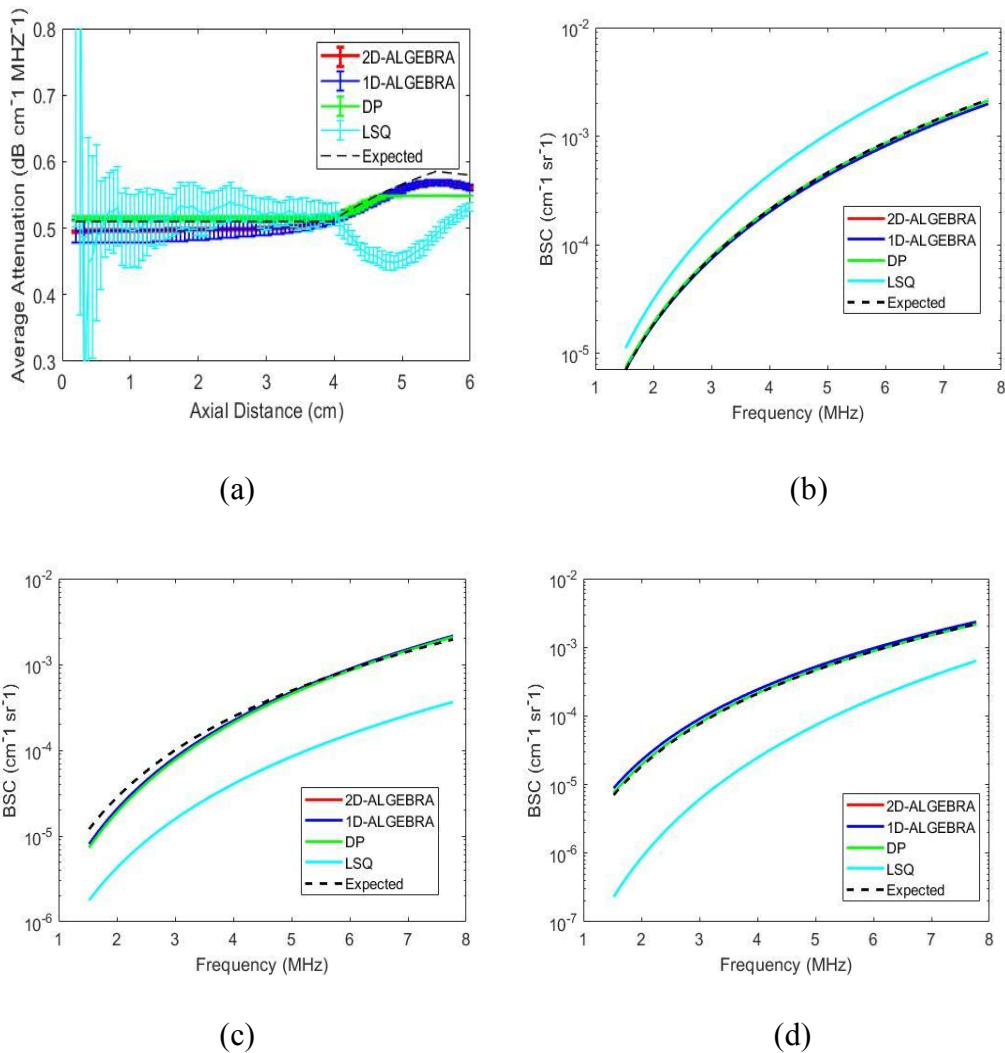


Figure 2-4 Results of 1D-ALGEBRA (blue), 2D-ALGEBRA (red), DP (green), and LSQ (cyan) in phantom C (attenuation step). The error bars show the standard deviation over the 860 samples for attenuation coefficient (a) and reconstructed BSC averaged over 400 samples in layer 1 (b), layer 2 (c), layer 3 (d). The black dashed line is the ground truth values. The red curve is superimposed by the blue curve.

- **Phantom E**

Figure 2-8 shows the parametric image of BSC at the center frequency. Quantitative assessment of BSC at the center frequency reveals that using 1D-ALGEBRA leads to 35% reduction in bias

in addition to 29% reduction in variance laterally compared to DP. Furthermore, using 2D-ALGEBRA yields 31% and 25% reduction in variance laterally and axially, respectively as well as 26% reduction in bias with respect to DP.

To estimate the QUS parameters in an image with  $N_C = 103$  and  $N_R = 55$ , required 2 and 4 sec, respectively. In comparison, a Matlab implementation of DP took 1200 second for the same problem.

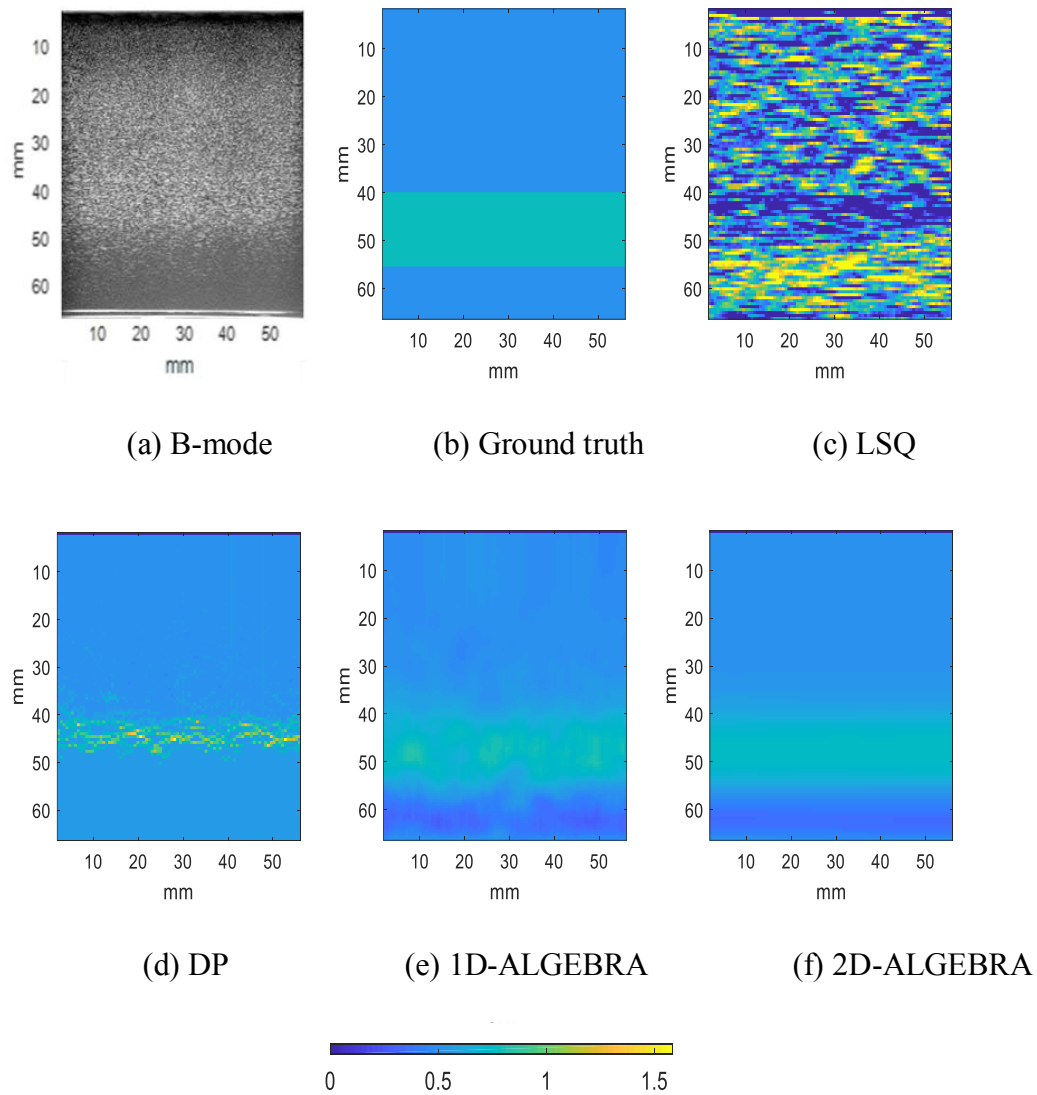
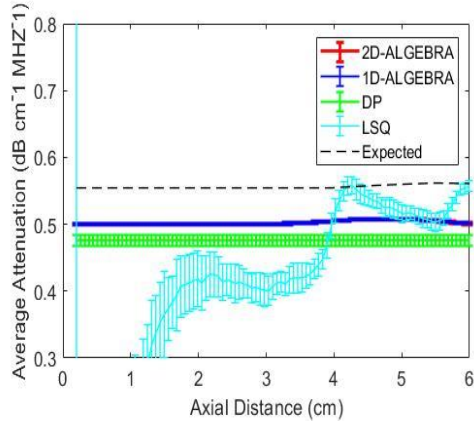
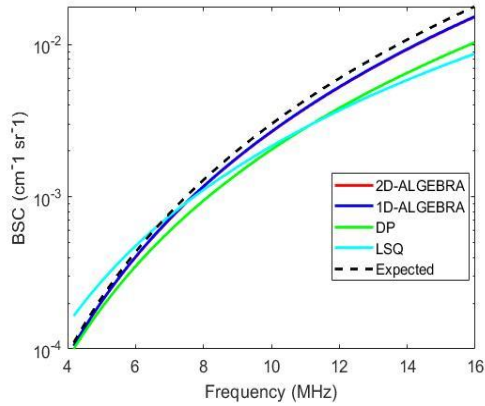


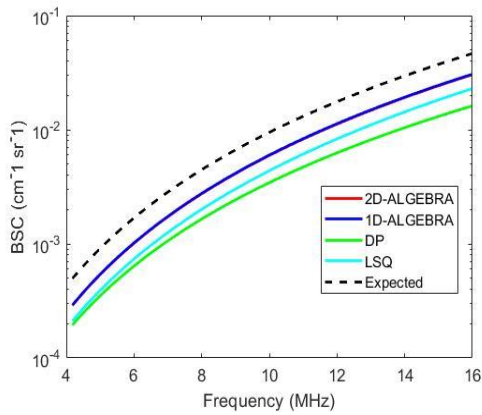
Figure 2-5 Parametric images of the local attenuation (computed from Eq. (2-32)) of phantom C (attenuation step). The color bar shows the value of local attenuation.



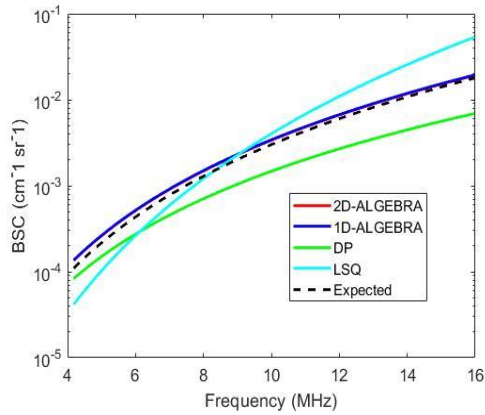
(a)



(b)



(c)



(d)

Figure 2-6 Results of 1D-ALGEBRA (blue), 2D-ALGEBRA (red), DP (green), and LSQ (cyan) in phantom D (backscatter step). The error bars show the standard deviation over the 860 samples for the effective attenuation (a) and reconstructed BSC averaged over 400 samples in layer 1 (b), layer 2 (c), layer 3 (d). The black dashed line is the GT. The red curve is superimposed by the blue curve.

Figures 2-9(a) and (b) show two parametric images of phantom E using 1D-Algebra with two different sets of weights:  $[10, 10, 10]$  and  $[10^4, 10^4, 10^4]$ , respectively. Figure 2-9(b) is smoother than Figure 2-9(a) (less variance), at the expense of blurring the edges of the inclusions (larger bias).

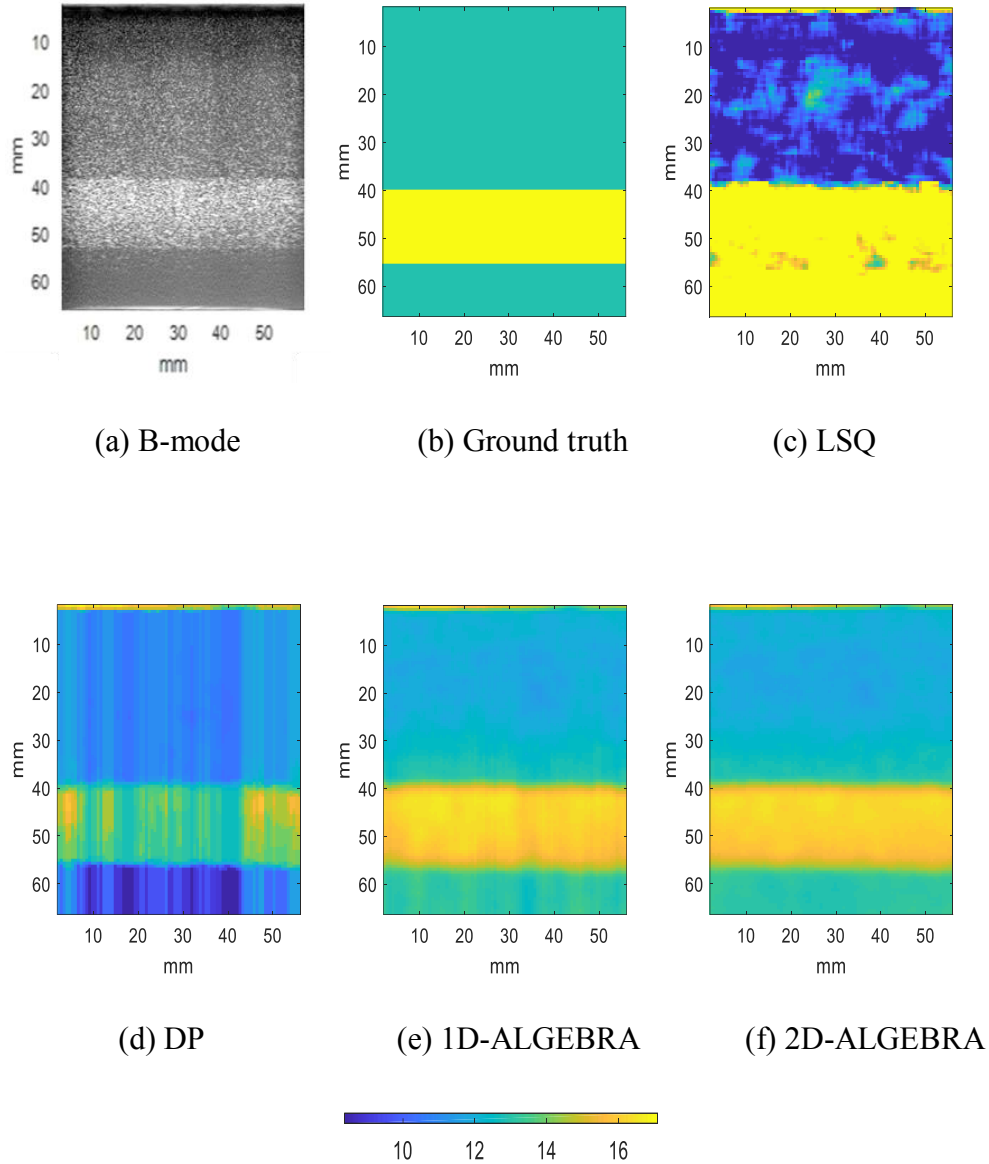


Figure 2-7 Parametric image of the backscatter coefficient at the center frequency of phantom D (backscatter step). Results are shown on a dB scale with respect to  $10^{-4} \text{ cm}^{-1} \text{ sr}^{-1}$ .

## 2.5 Discussion

This work presented two analytical, regularized estimators of the attenuation and backscatter properties of tissue-mimicking materials. After various tests in tissue-mimicking phantoms, these algorithms, named 1D- and 2D-ALGEBRA, outperformed previously proposed regularized strategies (DP) in the following aspects:

1. Because of 1D- and 2D-ALGEBRA are analytical solutions to the minimization of a cost function, it does not require the definition of search ranges for the expected values of the parameters.
2. Contrary to DP, the attenuation and backscatter parameters can be estimated on a continuous scale.
3. Both 1D- and 2D-ALGEBRA are up to 600 times faster than DP.

Considering these advantages, ALGEBRA has great potential to be applied clinically.

Theoretically, we expect exactly the same result using DP and 1D-ALGEBRA as the cost functions are the same. However, achieving this requires step sizes to be small enough so that discontinuous ranges provided by DP be approximated by continuous range provided by 1D-ALGEBRA. On the other hand, as we are using a large number of samples, it is practically impossible to consider small step size for each parameter. For that reason, DP results are not as good as 1D-ALGEBRA. Nevertheless, 1D-ALGEBRA yields estimates with similar levels of bias and standard deviation than DP, but in a much shorter time.

Moreover, comparing 1D-ALGEBRA and 2D-ALGEBRA reveals that 2D-ALGEBRA outperforms 1D-ALGEBRA in terms of bias and variance as it exploits regularization in both axial and lateral directions. Comparing the backscatter coefficient estimation results shown in Figures 2-2, 2-4, 2-6(b-d) can result in the misleading conclusion that 1D-ALGEBRA and 2D-ALGEBRA provide almost the same results. This happens as we are plotting semi-log of  $\beta_s^{Vs}$ . The improved performance of 2D-ALGEBRA compared to 1D-ALGEBRA is clear when 2D color-coded images are compared as shown in Figures 2-3, 2-5, and 2-7. In phantom A (uniform) shown in Figure 2-3, 2D-ALGEBRA leads to almost same estimations in all parts of the phantom. For the layered phantoms (Figures 2-5, 2-7) it can be seen that 2D-ALGEBRA can well distinguish three layers of phantoms C and D, especially in phantom D with the backscatter step.

## 2.6 Conclusion

In this study, two versions of an analytically-solved, regularized QUS estimation technique, 1D-ALGEBRA and 2D-ALGEBRA, were proposed to estimate the effective attenuation as well as the magnitude and frequency dependence of the backscatter coefficient. 1D-ALGEBRA is the fast version of our previous DP method which applies an axially regularized cost function. On the other

hand, 2D-ALGEBRA uses a globally (axially and laterally) regularized cost function. Regarding the quantitative analysis of bias and variance, we can conclude that applying 2D-ALGEBRA substantially improves the results compared to DP as it benefits the regularization in both axial and lateral directions.

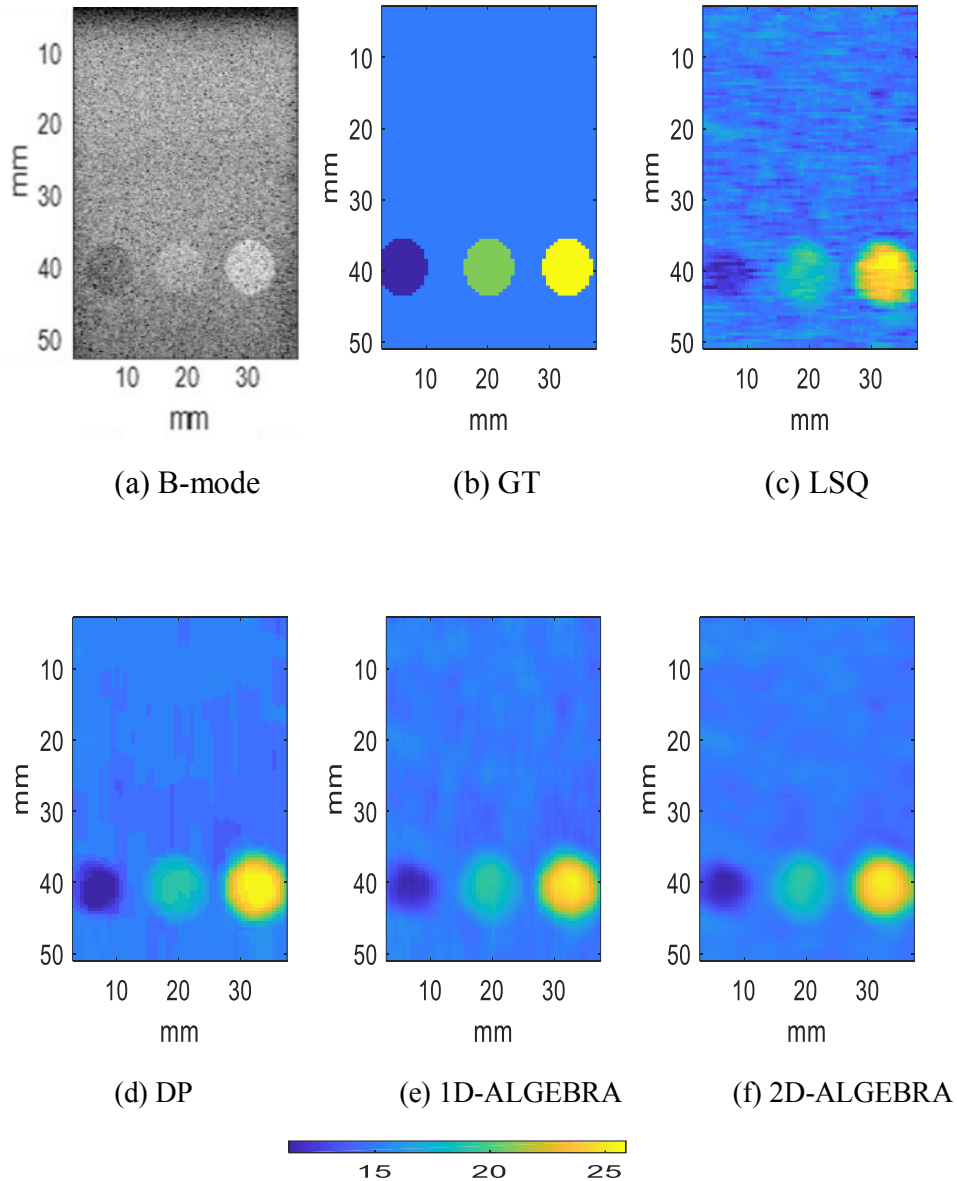


Figure 2-8 Parametric image of the backscatter coefficient at the center frequency of phantom E (inclusion phantom). Results are shown on a dB scale with respect to  $10^{-4} \text{ cm}^{-1} \text{ sr}^{-1}$ .

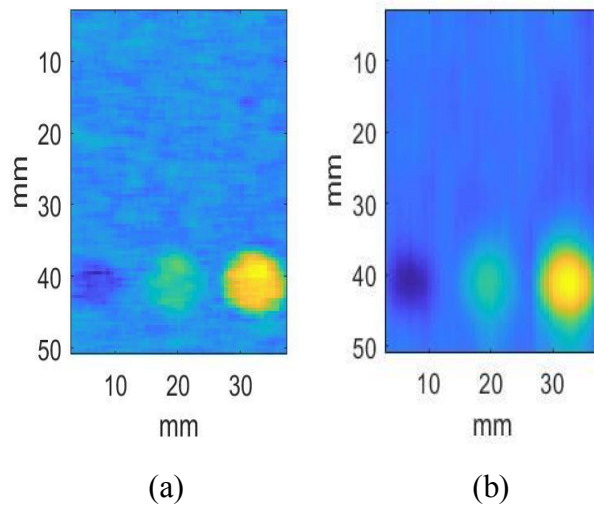


Figure 2-9 Influence of regularization weights in the parametric images of phantom E with 1D-ALGEBRA. Weights in (a): [10 10 10], weights in (b): [104 104 104].

## Chapter 3

# Physics-Inspired Regularized Pulse-Echo Quantitative Ultrasound: Efficient Optimization with ADMM

This chapter is submitted in IEEE Trans. UFFC, Major revision requested, 2022 and IEEE International Ultrasonic Symposium (IUS), 2022.

Herein, we make two contributions to this field: First, we consider the physics of the average attenuation and backscattering to devise regularization terms accordingly. More specifically, since the average attenuation gradually alters in different parts of the tissue while BSC can vary markedly from tissue to tissue, we apply  $L2$  and  $L1$  norms for the average attenuation and the BSC, respectively. Second, we multiply different frequencies and depths of the power spectra with different weights according to their noise levels. Our rationale is that the high-frequency contents of the power spectra at deep regions have a low signal-to-noise ratio. We exploit the alternating direction method of multipliers (ADMM) for optimizing the cost function. Qualitative and quantitative evaluation of bias and variance exhibit that our proposed algorithm substantially improves the estimations of the average attenuation and the BSC.

### 3.1 Background

Our group recently proposed ALGEBRA, to estimate the total attenuation and the BSC. ALGEBRA optimizes a penalty function containing the  $L2$  norm in both data and regularization terms. However, it suffers from two major issues as follows:

- 1) ALGEBRA considers  $L2$  norm regularization for both the average attenuation from intervening tissues (hereforth referred to as  $\alpha_{avg}$ ), and the BSC. Nonetheless, according to the physics, the  $\alpha_{avg}$ , and BSC have different rates of spatial variations (due to the averaging effect in  $\alpha_{avg}$  and the different physical mechanisms underlying absorption and scattering). In general, BSC can change from tissue to tissue, while  $\alpha_{avg}$ , presents more gradual changes.

- 2) ALGEBRA considers equal involvement for power spectra at each frequency and depth in

parameter estimation. However, different frequency components of the power spectrum present varying levels of signal-to-noise ratio (SNR) as a function of depth. A maximum likelihood estimator should put less trust in low SNR data.

To overcome the drawbacks mentioned above, we utilize the  $L2$  norm for the average attenuation and the  $L1$  norm for the BSC in the regularization part of the cost function. To optimize the proposed cost function efficiently, we employ the Alternation Direction Method of Multipliers, or ADMM. ADMM has been previously used by Coila *et al.* [50] for the regularization of local attenuation estimation. However, the authors did not parameterize BSC through the power-law model. We also introduce a criterion to define weights that vary with frequency and depth.

## 3.2 Methods

Similar to [56], [91], [92], we start with the RPM [83], a well-known approach employed to cancel system dependencies. Accordingly, we exploit equations 2-1 to 2-9.

### 3.2.1 ADMM for $L1$ Norm Regularization in QUS

We consider two different regularization functions  $R_1$  and  $R_2$  as follows. In  $R_1$ , we use the  $L1$  norm regularization for all the parameters:

$$R_1 = \sum_{i=2}^{N_R} w_a |a_i - a_{i-1}| + w_b |b_i - b_{i-1}| + w_n |n_i - n_{i-1}|$$

3-1

where  $w_a$ ,  $w_b$ , and  $w_n$  refer to the regularization weights for each parameter.

In  $R_2$ , we use  $L2$  norm for the average attenuation and  $L1$  for the BSC-related terms:

$$R_2 = \sum_{i=2}^{N_R} w_a (a_i - a_{i-1})^2 + w_b |b_i - b_{i-1}| + w_n |n_i - n_{i-1}|.$$

3-2

Here, the issue is that  $L1$  norm is not analytically differentiable. To solve this, consider the goal is minimizing the following constrain cost function:

$$C = D(x) + R(s)$$

$$\text{subject to } Kx + Ls = m$$

3-3

where  $K$  and  $L$  are known matrixes and  $m$  is a given vector,  $x$  and  $s$  are separable variables.

The augmented Lagrangian function solves the unconstrained version of the above constrained cost function as follows:

$$L\rho(x, s, y) = D(x) + R(s) + y^T (Kx + Ls - m) + \left(\frac{\rho}{2}\right) \|Kx + Ls - m\|_2^2$$

3-4

where  $y$  is the Lagrange multiplier and  $\rho > 0$  weights the constrain.

ADMM solves the Eq. (3-3) iteratively as follows:

$$x^{k+1} = \operatorname{argmin}_x (L\rho(x, s^k, y^k))$$

$$s^{k+1} = \operatorname{argmin}_s (L\rho(x^{k+1}, s, y^k))$$

$$y^{k+1} = y^k + \rho(Kx^{k+1} + Ls^{k+1} - m)$$

3-5

where  $k$  shows the iteration number.

Therefore, as ADMM's name implies, it penalizes each component of the cost function sequentially (alternative direction). This feature is favorable when an identical optimization procedure is not applicable for both data and regularization terms.

Herein, we start with rewriting Eq. (2-9) in the matrix format and call the obtained equation  $Qx = Y$  where  $x = [a_1 \ a_2 \ \dots \ a_{N_R} \ b_1 \ \dots \ b_{N_R} \ n_1 \ \dots \ n_{N_R}]^T$ ,  $Q$  is a matrix containing depth and frequency and  $Y$  is a vector. We multiply both sides of this equation by  $Q^T$  and name  $Q^T Q = H$ ,  $Q^T Y = t$ , and minimize the following cost function:

$$C = \frac{1}{2} \|Hx - t\|_2^2 + \lambda \|s\|_1$$

$$\text{subject to } Kx - s = 0$$

3-6

where  $s$  denotes the regularization term,  $H$ ,  $K$ , and  $t$  are equal to Eqs. 2-14, 2-17, 2-19, respectively:

Now, to update  $x$ ,  $s$ , and  $y$ , we exploit Eqs. (3-4), (3-5), where  $D(x)$  and  $R(s)$  are  $\frac{1}{2} \|Hx - t\|_2^2$ , and  $\lambda \|s\|_1$ , respectively. Accordingly, we obtain:

$$x^{k+1} := (H^T H + \rho K^T K)^{-1} H^T t + \rho K^T (s^k - y^k)$$

To update  $s$ , the following equation is obtained with respect to the shrinkage function  $S_{\frac{\lambda}{\rho}}$ :

$$s^{k+1} = \operatorname{argmin}_s \lambda \|s\|_1 - y + \frac{\rho}{2} \|Kx^{k+1} - s\|_2^2$$

which performs as soft thresholding:

$$S_{\frac{\lambda}{\rho}} = \operatorname{sgn}(\cdot) \max\{|\cdot| - \frac{\lambda}{\rho}, 0\}$$

Consequently, we have:

$$s^{k+1} := S_{\frac{\lambda}{\rho}}(Kx^{k+1} + y^k)$$

$$y^{k+1} = y^k + Kx^{k+1} - s^{k+1}.$$

3-7

In contrast to the BSC, which can vary abruptly between different tissue regions, the average attenuation varies moderately. To be consistent with this physical property, we propose employing the  $L2$  norm for the average attenuation and the  $L1$  norm for the BSC in the regularization part instead of incorporating the same norms for all the parameters. Accordingly, we split the vector  $x$  into two parts for the average attenuation  $x_1$  and the BSC  $x_2$ . Consequently, the corresponding elements of  $s$  and  $y$  are called  $s_1, s_2, y_1, y_2$ . Therefore, the algorithm is modified as follows:

$$C = \frac{1}{2} \|Hx - t\|_2^2 + \lambda_1 \|s_1\|_2^2 + \lambda_2 \|s_2\|_1$$

$$\text{subject to } K_1 x_1 - s_1 = 0, K_2 x_2 - s_2 = 0$$

3-8

Updating  $x$  and  $y$  are same as Eq. (3-7), but  $s$  is updated by  $s_1$  and  $s_2$  as follows:

$$\begin{aligned}
x^{k+1} &:= (H^T H + \rho K^T K)^{-1} H^T t + \rho K^T (s^k - y^k) \\
s_1^{k+1} &:= (K_1 x_1^{k+1} + y_1^k) / (\rho + \lambda_1) \\
s_2^{k+1} &:= \frac{S_{\lambda_2}}{\rho} (K_2 x_2^{k+1} + y_2^k) \\
y^{k+1} &= y^k + K x^{k+1} - s^{k+1}
\end{aligned}
\tag{3-9}$$

where  $H$  and  $K$  are same as Eqs. (2-14) and (2-17), and  $K_1, K_2, x_1, x_2$  are:

$$K_1 = K_a, K_2 = \begin{bmatrix} K_b & \mathbf{0} \\ \mathbf{0} & K_n \end{bmatrix}
\tag{3-10}$$

$$x_1 = [a_1 \ a_2 \ \dots \ a_{N_R}]^T, x_2 = [b_1 \ \dots \ b_{N_R} \ n_1 \ \dots \ n_{N_R}]^T
\tag{3-11}$$

### 3.2.2 Weighted Frequency

We use a weighted frequency scheme to give the power spectra a score (weight) at each frequency and depth. To do so, the data term is multiplied by  $w_d$ . Thus, the data term formulation is adapted as follows:

$$D = \sum_{l=1}^{N_F} \sum_{i=1}^{N_R} w_d(l, i) (X(f_l, z_i) - b_i - n_i \ln(f_i) + 4a_i f_l z_i)^2
\tag{3-12}$$

To select the bandwidth, we plot the logarithmic scale of the lateral average of the power spectra of sample and reference phantoms and determine the corresponding frequency range where higher power is amassed. The black dash lines in Figures 3-1 and 3-2 illustrate this range for example power spectra obtained from a sample phantom and a reference phantom, which are the corresponding frequencies for 80% of the maximum logarithmic power spectra. Herein, the background of the sample phantom is the reference phantom. To calculate  $w_d$ , we propose using contour level sets depicted in Figures 3-3 and 3-4, and to carry out this, we form the following equations to compute  $w_s$  and  $w_r$  for the sample and reference phantoms separately.

$$w_s = \begin{cases} 1, & S_s > T_{1s} \\ \frac{S_s - T_{2s}}{T_{1s} - T_{2s}}, & T_{1s} > S_s > T_{2s} \end{cases}$$

$$w_r = \begin{cases} 1, & S_r > T_{1r} \\ \frac{S_r - T_{2r}}{T_{1r} - T_{2r}}, & T_{2s} > S_r > T_{2r} \end{cases}$$

where  $S$  is the logarithmic scale of the power spectra shown in Figures 3-1 and 3-2, and  $T_1$  and  $T_2$  express the upper level and lower level of contours shown in Figures 3-3 and 3-4 with yellow and purple colors, respectively. The upper and lower level are 90% of the maximum and 167% of the minimum of the logarithmic power spectra.

In the end, the intersection of the  $w_s$  and  $w_r$  computed using element-wise matrix multiplication is regarded as  $w_d$ :

$$w_d = w_s \odot w_r.$$

3-13

Figure 3-1(a) exhibits power spectra of the sample phantom that were affected by the specular reflectors. Accordingly, we only consider the reference phantom to calculate  $w_d$  ( $w_d = w_r$ ). Figures 3-5 and 3-6 demonstrate  $w_d$  for the region with specular reflectors and the region with inclusions.

### 3.2.3 Tissue mimicking phantom and data acquisition

Two regions of a phantom named Gammex 410SCG (Gammex-Sun Nuclear, Middleton, WI) were scanned with the serial number of 805546-4612-3 and 802259-2888-5 at Mexico and University of Wisconsin-Madison. In both regions, the background is the reference phantom.

- **Region with Specular Reflectors**

Five uncorrelated frames of RF data were collected, using the same transducer and operation parameters as the Gammex 410 SCG phantom. This region contains the presence of three nylon filaments of 0.1 mm in diameter. To get the Nylon filaments to produce specular reflectors, they were scanned placing the transducer perpendicular to the front face of the phantom. These structures produce echo signals originated from a coherent scattering process, despite the fact that these structures can commonly be present prior to the region of interest or within it, they violate

the assumption of incoherent scattering process on which the RPM is based, reducing the accuracy and precision of acoustic parameters such as the backscatter coefficient [93], [94]. Therefore, the importance of this analysis was to evaluate the susceptibility of the method in the estimation of QUS parameters, in terms of bias and variance, due to the presence of specular reflectors.

The background has the following properties:

- $\alpha_{eff} = 0.6035 \text{ dB cm}^{-1} \text{ MHz}^{-1}$
- $\beta_r = 2.9966 \times 10^{-6} \text{ cm}^{-1} \text{ sr}^{-1} \text{ MHz}^{-\nu}$
- $\nu_n = 3.4281$
- $\sigma_{b,r}(8 \text{ MHz}) = 3.74 \times 10^{-3} \text{ cm}^{-1} \text{ sr}^{-1}$

• **Region with Inclusions**

Ten uncorrelated frames of RF data were collected, using the homogeneous region as the reference with an L11-5v transducer operated at an 8 MHz center frequency on a Verasonics Vantage 128 system (Verasonics, Kirkland, WA).

This region is composed of three cylindrical inclusions with +12dB, +6dB, and -6dB scattering respecting the background. The  $\alpha_{avg}$  and the BSC of this region are same as the region with specular reflectors.

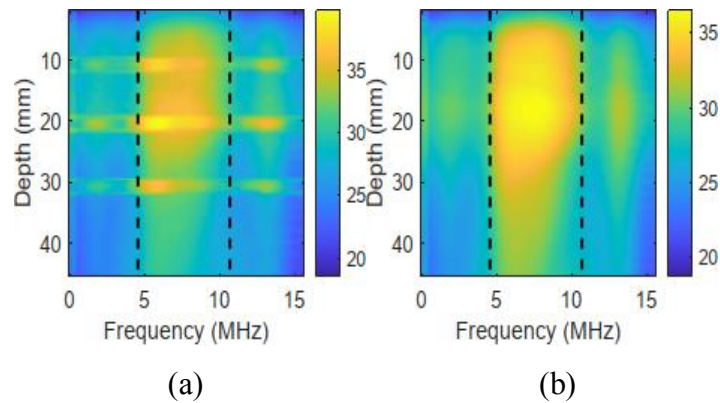
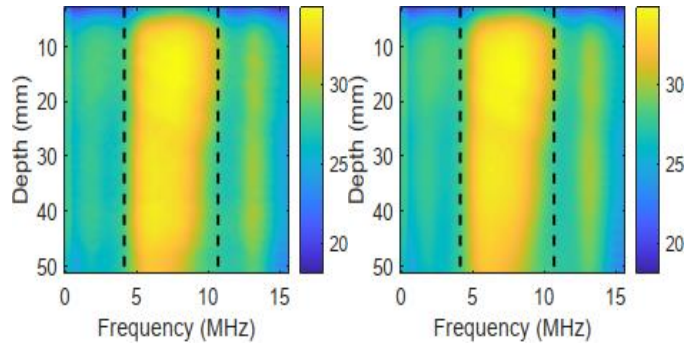


Figure 3-1 Lateral average of the power spectra of sample phantom (a) and reference phantom (b) in the logarithmic scale for the region with specular reflectors.



(a)

(b)

Figure 3-2 Lateral average of the power spectra of sample phantom (a) and reference phantom (b) in the logarithmic scale for the region with inclusions.

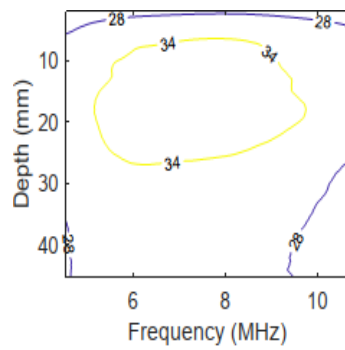
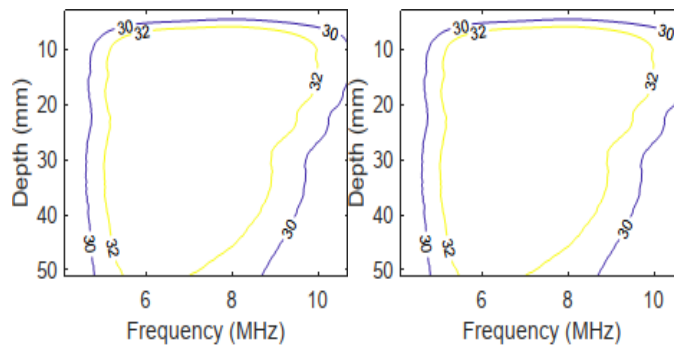


Figure 3-3 Contour levels of the lateral average of the power spectra of reference phantom in the logarithmic scale for the region with specular reflectors.



(a)

(b)

Figure 3-4 Contour levels of the lateral average of the power spectra of sample phantom (a) and reference phantom (b) in the logarithmic scale for the region with inclusions.

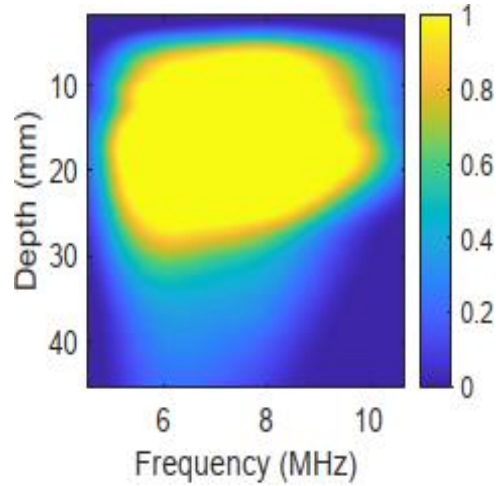


Figure 3-5  $w_d$  for the region with specular reflectors.

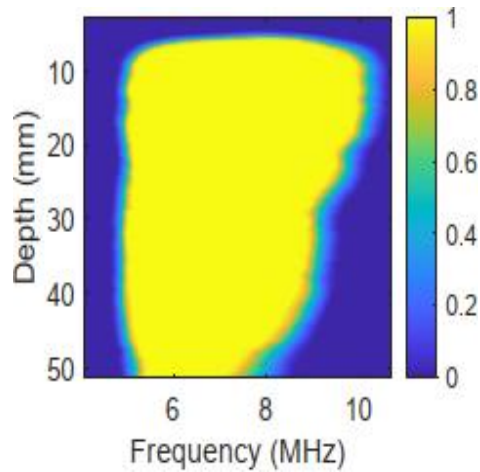


Figure 3-6  $w_d$  for the region with inclusions.

### 3.2.4 Quantitative Metrics

In this study, we report the variance and bias of the estimations to evaluate and compare the results. To compute the variance and bias, four regions of the interests (ROI) are selected for each region. Figures. 3-7 and 3-8 present the locations of each ROI on a B-mode image of the region with specular reflectors and the region with inclusion, respectively. For the region with specular reflectors the locations are selected between the fibers and for the region with inclusions at the center of the background and each inclusion.

To report the bias and variance for each ROI, we calculate the average of the estimations across the frames,  $M$ , and exploit the following equations. The BSC is scaled to dB w. r. to  $10^{-4}$  as follows:

$$\text{bias\_}\alpha_{avg} = |M_{a_i}(\cdot) - GT_a|$$

$$\text{variance\_}\alpha_{avg} = \text{var}(M_{a_i}(\cdot))$$

$$\text{bias\_}BSC = |10 \log_{10} \left( \frac{M_{BSC_i}(\cdot)}{10^{-4}} \right) - 10 \log_{10} \left( \frac{GT_{BSC}}{1e^{-4}} \right)|$$

$$\text{variance\_}BSC = \text{var} \left( 10 \log_{10} \left( \frac{M_{BSC_i}(\cdot)}{10^{-4}} \right) \right)$$

3-14

where GT accounts for the ground truth.

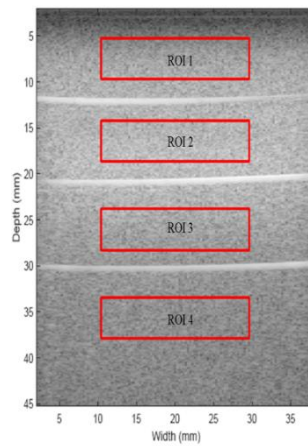


Figure 3-7 Location of ROI in the region with specular reflectors.

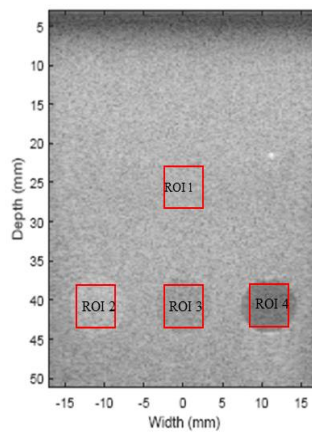


Figure 3-8 Location of ROI in the region with inclusions.

### 3.3 Results

Figures. 3-9 to 3-13 compare six techniques tested on the region with specular reflectors and the region with inclusions. Regularization weights are tuned individually for each set to ensure the best results are fulfilled.

- **Region with Specular Reflector**

Figures. 3-9 and 3-10 report the bias and variance of the BSC on the dB scale and the average attenuation. The Figures demonstrate the superior performance of ADMM in terms of bias and variance compared to the ALGEBRA. More precisely, comparing ADMM and ALGEBRA both without  $w_d$  in regions 1 to 4 reveals the bias of BSC estimation decreased 86.1%, 88.3%, 76.3%, and 83.1%, respectively and the variance experienced 68.8%, 78.9%, 60.1% and 77.7% reduction. Moreover, the bias of average attenuation decreased 85.5%, 92.7%, 83%, and 93.2% in ROI 1 to 4 as well as 76.5%, 84.4%, 54.1%, and 76.2% reduction in the variance in each region is obtained. Additionally, associating ADMM with  $w_d$ , and different norms in the regularization term enhance the estimation.

Quantitative comparison of ALGEBRA with and without  $w_d$  in Figure 3- 9 shows that smoother estimations are acquired by incorporating  $w_d$  in the cost function. Moreover, engaging ADMM with  $w_d$  is accompanied by the following quantitative analysis concerning not including  $w_d$  in the cost function. Using the  $w_d$  strategy in ADMM reduced the bias of BSC by 88.1%, 52.5%, and 98.9%, in regions 1 to 3, compared to not using  $w_d$ . Additionally, the variance is reduced by 42.1% in region 1. Moreover, attenuation evaluation results in 86.3%, 44.6%, decline in bias in regions 1 and 3. Regarding variance appraisal 52.2% lower variance is reported in region 1 when using ADMM with  $w_d$  vs not using  $w_d$ . A Matlab implementation of ALGEBRA shows it is 100 times faster than ADMM for this region.

- **Region with Inclusion**

The results of BSC estimation at center frequency using six techniques are depicted in Figure 3-11. The visual comparison of the parametric images presents that ADMM surpasses ALGEBRA as it is more similar to the GT. From Figures 3-12 and 3-13, it is perceived that encompassing  $w_d$  in the ALGEBRA cost function reduces the bias and variance of the BSC and the average

attenuation estimations. Comparing results of our proposed technique concerning ADMM without weighting the data term shows 80.3% reduction in the bias in region 2 as well as 15.5%, 22.1%, and 1% reduction in the variance of BSC estimation in region 1, 3, and 4, respectively. Furthermore, attenuation evaluation results in 29.4%, 88.2%, and 66.1% decline in the bias of regions 2 to 4 besides 4.2%, 10.9% decrement in the variance of regions 1 and 3. A Matlab implementation of ALGEBRA shows it is 18 times faster than ADMM for this region.

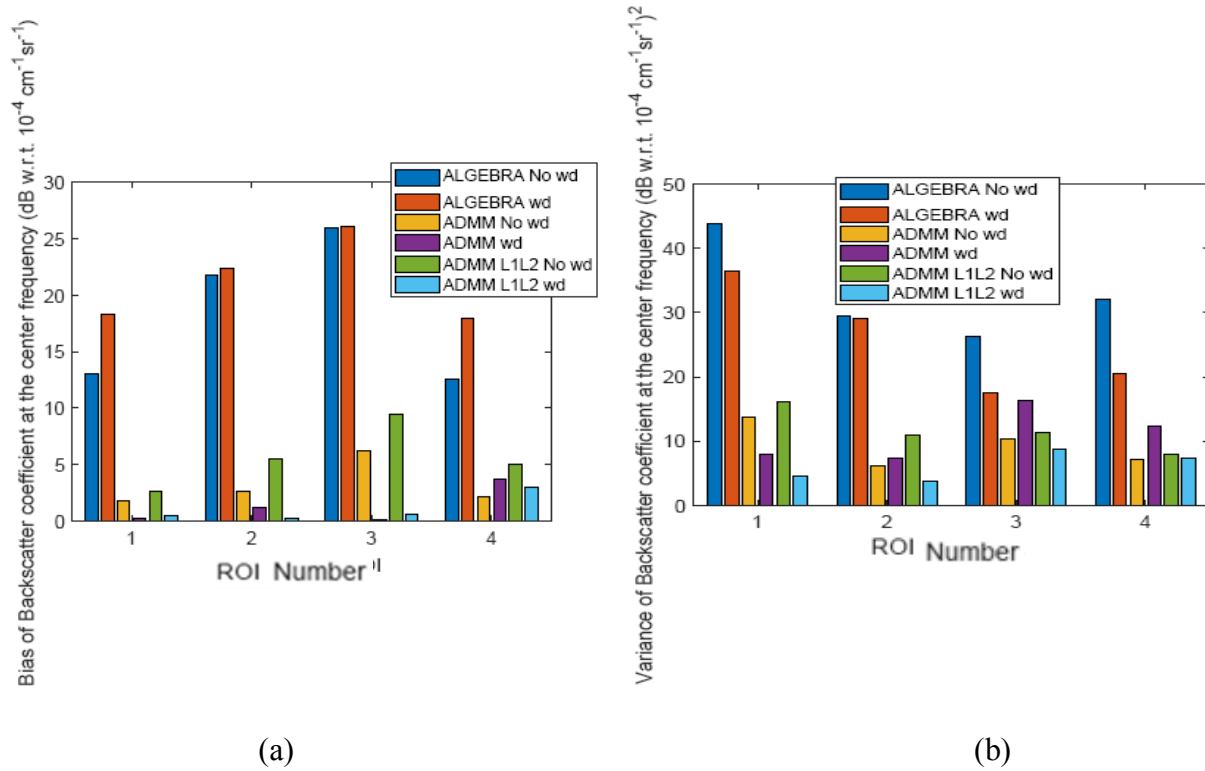


Figure 3-9 Comparison of bias (a) and variance (b) of the BSC using ALGEBRA (ALGEBRA No  $w_d$ ), ALGEBRA associated with weighting the data term (ALGEBRA  $w_d$ ), ADMM without weighting the data term and using  $L2$  norm in the regularization part for all the parameters (ADMM No  $w_d$ ), ADMM associated with weighting the data term and using  $L2$  norm in the regularization part for all the parameters (ADMM  $w_d$ ), ADMM without weighting the data term and using  $L1$  norm for the BSC and  $L2$  norm for the average attenuation (ADMM L1L2 No  $w_d$ ), and ADMM associated with weighting the data term and using  $L1$  norm for the BSC and  $L2$  norm for the average attenuation (ADMM L1L2  $w_d$ ) in four ROI of the region with specular reflectors. Results are shown on a dB scale with respect to  $10^{-4} \text{ cm}^{-1} \text{ sr}^{-1}$ .

### 3.4 Discussion

In this work, we exploited the RPM to formulate our proposed technique. Although new reference phantom free methods have been developed, the RPM can be feasibly implemented in the clinic without having to scan a phantom after each patient. Commercial scanners can be equipped by a pre-tuned reference phantom or data to train a machine learning model for providing the attenuation values. However, these systems provide the BSC measurement at one frequency [2].

Here, we presented a novel penalty function consisting of  $L2$  norm weighted data term and  $L1$  and  $L2$  norm regularization terms optimized using ADMM. Our method was applied to data acquired from two regions of a phantom which we called the region with specular reflectors and the region with inclusions.

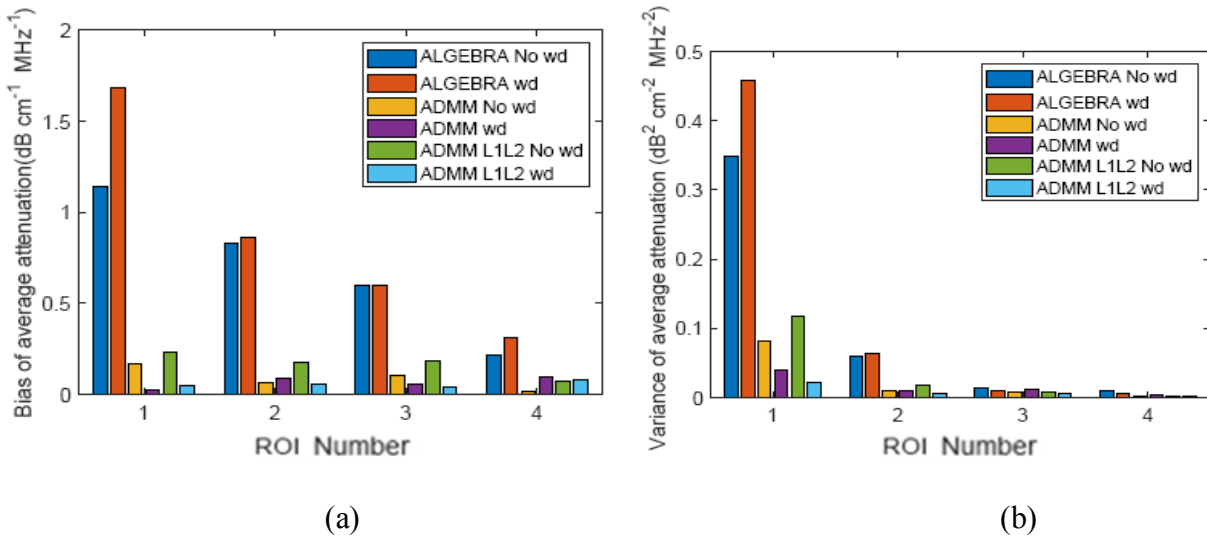


Figure 3-10 Comparison of bias (a) and variance (b) of the average attenuation using ALGEBRA (ALGEBRA No  $w_d$ ), ALGEBRA associated with weighting the data term (ALGEBRA  $w_d$ ), ADMM without weighting the data term and using  $L2$  norm in the regularization part for all the parameters (ADMM No  $w_d$ ), ADMM associated with weighting the data term and using  $L2$  norm in the regularization part for all the parameters (ADMM  $w_d$ ), ADMM without weighting the data term and using  $L1$  norm for the BSC and  $L2$  norm for the average attenuation (ADMM L1L2 No  $w_d$ ), and ADMM associated with weighting the data term and using  $L1$  norm for the BSC and  $L2$  norm for the average attenuation (ADMM L1L2  $w_d$ ) in four ROI of the region with specular reflectors.

Unlike [91], we carefully focused on selecting the bandwidth in the first part of our proposed technique. In [91], the frequency range was chosen based on the evaluation of the bias and variance of the BSC and the average attenuation estimations. Therefore, we observed for the region with inclusions a wide frequency range leads to the results that were in very good agreements with the GT. However, herein, our strategy for selecting the bandwidth of interest is different. Figures 3-1 and 3-2 show that the frequency ranges were chosen based on the parametric image of the power spectra of the sample and reference phantoms. The intersection of the corresponding frequency ranges of the sample and the reference phantoms with high concentrated power is accounted for as the bandwidth of interest which is depth dependent as well. Our proposed approach for selecting the bandwidth of interest is more reasonable compared to the method we applied in [91] because of two points: 1) It is possible that a wide frequency range leads to excellent results in terms of the quantitative and qualitative assessments, but the selected band may contain low power, which is the case when sample and reference phantom are the same 2) In clinical applications with unknown GT, evaluation of bias which leads to selecting the frequency range is not practical.

In the next step, we weighted the data term using the contour level sets. Weighting the data term is similar to giving scores from 0 to 1 to the least and most informative band of the echo signal power spectrum. On the other hand, considering zero weight does not make sense as there is still power on the less informative parts. Furthermore, assigning zero weights means completely ignoring the data term part of the cost function. Hence, we shifted the calculated  $w_d$  and normalized it by dividing it by the maximum value of the new calculated  $w_d$ . Afterward, we appointed the  $L2$  regularization norm for attenuation and the  $L1$  norm for BSC to be in accordance with the physic-based properties of each. Finally, our novel cost function was minimized using ADMM. An important point that should be taken into account is that the expense of the computational complexity for reducing the bias and variance is worth, especially when a phantom or tissue that we attempt to characterize, be similar to the region with specular reflectors meaning that the majority part of the media is with the same QUS parameters and a small fraction of that has different parameters. In such a case, the ALGEBRA completely fails and our proposed technique is highly preferable. But similar to ALGEBRA, a limitation of our method is that for calculating the local attenuation, first, the effective attenuation needs to be estimated. Overall, the best results in terms of bias and variance for both regions of the phantom were acquired by

weighting the data term and applying  $L1$  and  $L2$  norms in the regularization part of the cost function.

Calculating  $w_d$  is performed offline. In a general case, we need to consider both phantoms. Here, as the sample and reference phantoms are the same and we take into account the average power spectra, the correlation between the power spectra of the sample and reference is high and they look similar. Therefore, considering only reference would be enough.

In real experiments where GT are unknown, choosing the weights can be more challenging. In such cases, one way to investigate what weights are proper is to first run LSQ which is equal to setting zero weights for all the parameters and plot the QUS parameters. Then, we can set the weights to the values in the range of 0.1, 10,  $1e2$ , ...,  $1e8$  and plot the results. Let us assume that for the weight  $1e3$ , the results are almost identical to the LSQ. This means this weight is too small. Furthermore, if we suppose for the weight  $1e7$  the results are constant, it means the chosen weight is too large. In this case,  $1e5$  can be the optimal weight. To test this, we can double the optimal weight ( $2e5$ ) and plot the results. If the results are similar to  $1e5$ , then the optimal weight is  $1e5$ . This implies that the results are independent of the weight.

Additionally, here, we did not make an effort to optimize the computational complexity. Instead, our goal was to introduce a prototype for estimating the average attenuation and BSC. On the other hand, Matlab is inherently inefficient especially when relying on for loops over matrix manipulations. Dramatic speed improvements can be obtained using the same algorithm when implemented using a different language.

Significant differences between our work and other groups are: I) Proposing weighting the data term. II) Taking into account physics properties of QUS parameter in the cost function.

We predict using  $w_d$  and combining  $L1$  and  $L2$  norms in the cost function can further improve the bias of estimation for the cases that sample and reference phantoms are different.

### **3.5 Conclusion**

Herein, we proposed a novel approach for estimating the average attenuation and the BSC. Our algorithm incorporates ADMM to penalize a cost function containing  $L2$  norm weighted data term and  $L1$  and  $L2$  norms regularization terms to be associated with the physical properties of the BSC and the average attenuation. Visual and quantitative evaluations justify that our proposed algorithm substantially outperforms the other techniques.

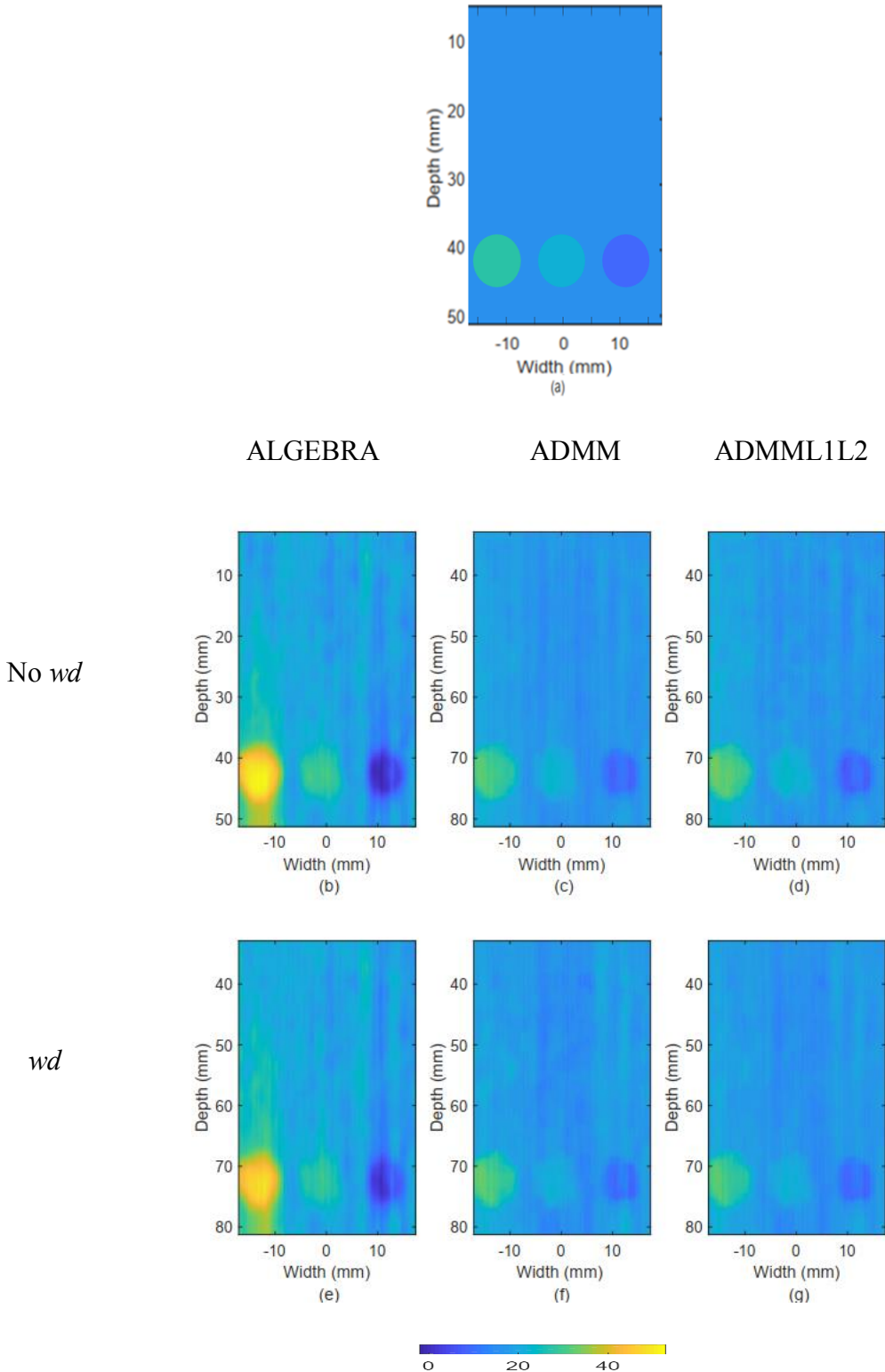


Figure 3-11 Qualitative comparison of parametric image of the BSC at the center frequency of the region with inclusions, with GT (a), and different methods (b-g). Results are shown on a dB scale with respect to  $10^{-4} \text{ cm}^{-1} \text{ sr}^{-1}$ .

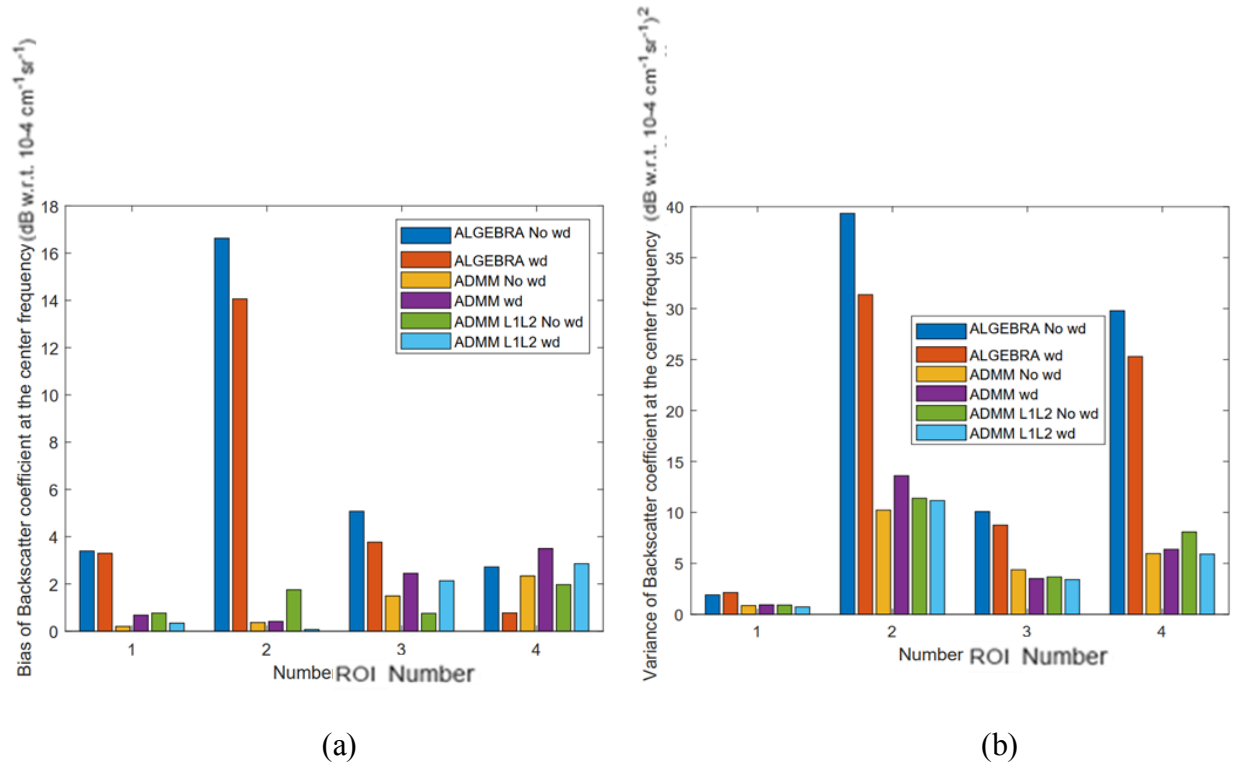


Figure 3-12 Comparison of bias (a) and variance (b) of the BSC using ALGEBRA (ALGEBRA No  $w_d$ ), ALGEBRA associated with weighting the data term (ALGEBRA  $w_d$ ), ADMM without weighting the data term and using L2 norm in the regularization part for all the parameters (ADMM No  $w_d$ ), ADMM associated with weighting the data term and using L2 norm in the regularization part for all the parameters (ADMM  $w_d$ ), ADMM without weighting the data term and using L1 norm for the BSC and L2 norm for the average attenuation (ADMM L1L2 No  $w_d$ ), and ADMM associated with weighting the data term and using L1 norm for the BSC and L2 norm for the average attenuation (ADMM L1L2  $w_d$ ) in four ROI in the region with inclusions. Results are shown on a dB scale with respect to  $10^{-4} \text{ cm}^{-1} \text{ sr}^{-1}$ .

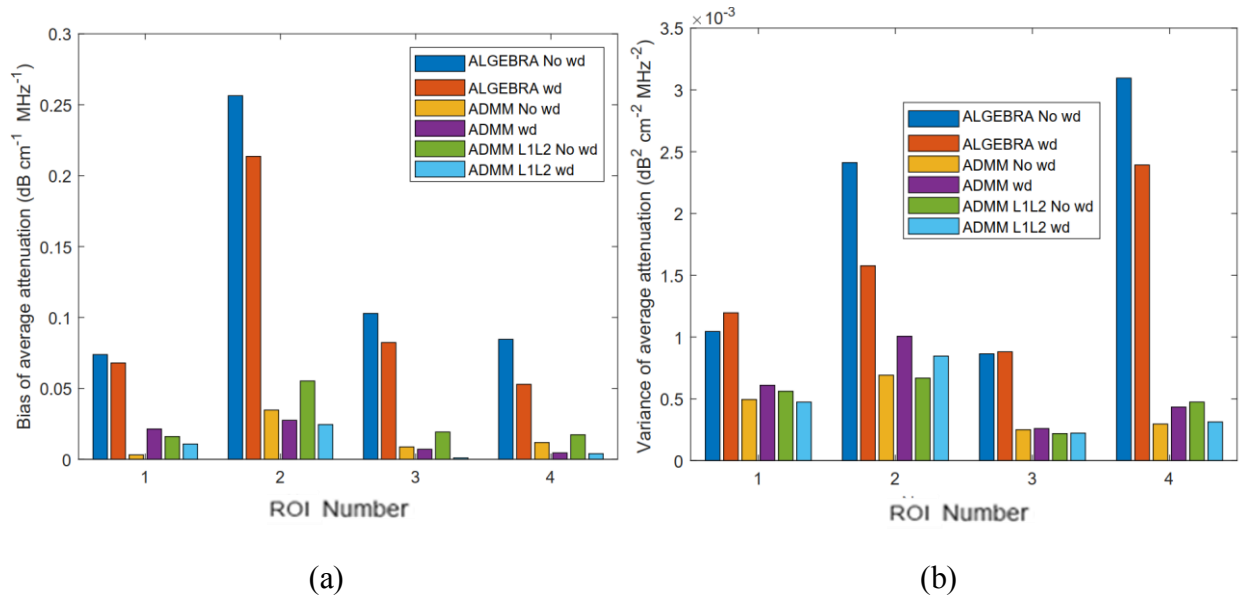


Figure 3-13 Comparison of bias (a) and variance (b) of the average attenuation using ALGEBRA (ALGEBRA No  $w_d$ ), ALGEBRA associated with weighting the data term (ALGEBRA  $w_d$ ), ADMM without weighting the data term and using L2 norm in the regularization part for all the parameters (ADMM No  $w_d$ ), ADMM associated with weighting the data term and using L2 norm in the regularization part for all the parameters (ADMM  $w_d$ ), ADMM without weighting the data term and using L1 norm for the BSC and L2 norm for the average attenuation (ADMM L1L2 No  $w_d$ ), and ADMM associated with weighting the data term and using L1 norm for the BSC and L2 norm for the average attenuation (ADMM L1L2  $w_d$ ) in four ROI in the region with inclusions.

## Chapter 4

# Regularized Estimation of Effective Scatterer Size and Acoustic Concentration Quantitative Ultrasound Parameters Using Dynamic Programming

This chapter is published in IEEE Engineering in Medicine and Biology Society (EMBC), 2020 and XVI Mexican Symposium on Medical Physics, 2020.

Herein, we develop a novel technique based on DP to simultaneously estimate the acoustic attenuation, the effective scatterer size (ESS), and the acoustic concentration (AC) from ultrasound backscattered power spectra. This is achieved through two different approaches: (1) using a Gaussian form factor (GFF) and (2) using a general form factor (gFF) that is more flexible than the Gaussian form factor but involves estimating more parameters. Both DP methods are compared to an adaptation of a previously proposed LSQ method. Simulation results show that in the GFF approach, the variance of DP is on average 88%, 75% and 32% lower than that of LSQ for the three estimated QUS parameters. The gFF approach also yields similar improvements.

### 4.1 Background

We recently proposed a novel method to estimate attenuation and parameters from a power-law fit to the backscatter coefficient with improved precision. This method is based on a regularized cost function and optimized using DP [56], [57]. Recent work by other groups has also shown that more accurate QUS parameters can be estimated using regularized cost functions [39], [50], [52], [95].

Herein, we build on that work to include the use of form factor models to obtain a regularized estimate of ESS, AC, and the effective attenuation. We intend to involve scatterer characterization in backscattering formulas to accurately and precisely estimate AC and ESS in addition to effective attenuation. In the following two sections, we outline two different approaches based on DP for estimating QUS parameters. In both approaches, we exploit the RPM to have a system independent algorithm. In the last section, we present our results and compare them to the LSQ method.

## 4.2 Methods

The general formula of attenuation is:

$$A(f, z) = \exp(-4\alpha f z)$$

4-1

where  $A$  is the total attenuation,  $f$  is the frequency,  $z$  is the depth and  $\alpha$  is the effective attenuation coefficient (average attenuation from intervening tissues). A general model for parametrizing the backscatter coefficients is:

$$B(f) = B_0 G(f)$$

4-2

where  $B_0$  is the magnitude and  $G(f)$  is the frequency dependence of backscatter coefficients. Under the condition of weak scattering, the following equation defines  $G(f)$  in terms of a form factor model ( $F(f, a_{eff})$ ):

$$G(f) = f^4 F(f, a_{eff})$$

4-3

### 4.2.1 Gaussian form factor

As the microstructure of real tissue is often modeled using scatterers with spherically-symmetrical, Gaussian impedance correlation functions [17], a Gaussian form factor model has been selected as follows:

$$F(f, a_{eff}) = \exp\left(-0.827(k a_{eff})^2\right)$$

4-4

where  $k$  is wave number and  $a_{eff}$  is ESS. By substituting (4-4) in (4-3), and (4-3) in (4-2), we have:

$$B(f) = B_0 f^4 \exp\left(-0.827(k a_{eff})^2\right).$$

4-5

To estimate ESS and AC, we use the RPM strategy based on normalizing the power spectrum  $S$  of the sample (s) by a power spectrum from a reference phantom ( $r$ ), both of which are estimated from RF signals from a clinical scanner. The spectral ratio can be modeled as:

$$\frac{S_s}{S_r} = \frac{B_s(f)A_s(f, z)}{B_r(f)A_r(f, z)}$$

$$= \frac{B_{0_s}f^4 \exp(-0.827(k_s a_s)^2) \exp(-4\alpha_s f z)}{B_{0_r}f^4 \exp(-0.827(k_r a_r)^2) \exp(-4\alpha_r f z)}$$

4-6

We assume that the media has a constant sound speed with the frequency dependence of attenuation near  $f^1$ . In addition, in order to use RPM, the sample and the reference phantom must have similar sound speed, so  $k_s = k_r$ . After taking the natural logarithm from both sides of (6), and substituting  $X_1 = \log \frac{S_s}{S_r}$ ,  $B = \log \frac{B_{0_s}}{B_{0_r}}$ ,  $a = a_s^2 - a_r^2$ , and  $\alpha = \alpha_s - \alpha_r$ , we have:

$$X_1 = B - 0.827k^2a - 4\alpha f z$$

4-7

This equation is summed over the frequency range from  $f_1$  to  $f_2$ . The goal is to estimate  $B$ ,  $a$ , and  $\alpha$  using DP. Then, using the following equations,  $B_{0_s}$ ,  $a_s$ , and  $\alpha_s$  can be obtained:

$$B_{0_s} = \exp(B) B_{0_r}, a_s = \sqrt{(a + a_r^2)}, \alpha_s = \alpha + \alpha_r$$

4-8

#### 4.2.2 General form factor

According to [15], for Gaussian scatterers and other form factors over a limited range of frequency,  $F(f, a_{eff})$  and  $ka \leq 1.2$  can be considered as follows:

$$F(f, a_{eff}) = \exp(-A f^n)$$

4-9

where bold  $A$  is related to the ESS of tissue by  $0.827 \left( \frac{2\pi}{c} a \right)^n$ ,  $c$  is sound speed within tissue which is assumed to be 1540 m/s, and  $n \sim 2$ . After taking the ratio of power spectra of echo signals of sample and reference phantoms, and taking the natural logarithm, we have:

$$\frac{S_s}{S_r} = \frac{B_{0_s} f^4 \exp(-A_s f^n) \exp(-4\alpha_s f z)}{B_{0_r} f^4 \exp(-A_r f^n) \exp(-4\alpha_r f z)}$$

4-10

$$X_2 = B - A f^n - 4\alpha f z$$

4-11

For the rest of this work, we first assumed  $n=2$ , and estimated three parameters  $B$ ,  $A$ , and  $\alpha$ . This equation is summed over the frequency range from  $f_1$  to  $f_2$ . Then, we considered  $n$  as a parameter that should be estimated. In both approaches, once  $B_{0_s}$  and  $a_s$  (in approach 1) and  $A_s$  (in approach 2) are estimated, AC ( $N\gamma^2$ ) can be obtained using the following equation:

$$B_{0_s} = \left( \frac{2\pi}{c} \right)^4 a_s^6 \frac{N\gamma^2}{9}$$

4-12

As a first approximation to assess the accuracy and precision of the proposed DP method, we simulated sample and reference power spectra adding white Gaussian noise to  $B$ ,  $a$ , and  $\alpha$  and to  $B$ ,  $a$ ,  $n$ , and  $\alpha$  in equations (4-7) and (4-11), respectively. Spectra were simulated to come from a layered phantom having a central layer with  $\alpha=0.7787 \text{ dB}\cdot\text{cm}^{-1}\text{MHz}^{-1}$ ,  $B=0.3222\text{e-}5 \text{ cm}^{-1}\cdot\text{sr}^{-1} \text{ MHz}^{-n}$ ,  $a=31 \text{ }\mu\text{m}$ ,  $A=13.0269 \text{ }\mu\text{m}^n\mu\text{s}^n \text{ m}^{-n}$ ,  $n=3.1263$  sandwiched between two layers with  $\alpha=0.5101$ ,  $B=0.1600\text{e-}5$ ,  $a=35$ ,  $A=11.3917$ ,  $n=3.5190$  and  $\alpha=0.5196$ ,  $B=0.1600\text{e-}5$ ,  $a=35$ ,  $A=15.7979$ ,  $n=3.5190$ . The values for the reference phantom are  $\alpha=0.5101$ ,  $B=0.1599\text{e-}5$ ,  $a=35$ ,  $A=10.3917$ ,  $n=2$ . All of these values are used for two simulation approaches. Twenty independent realizations of the power spectra were simulated for each approach through the following equations:

Data for approach 1:

$$X_1 = \log \frac{B_{0_s}}{B_{0_r}} + \eta_{B_i} - 0.827k^2 \left( (a_s^2 - a_r^2) + \eta_{a_i} \right) - 4 \left( (\alpha_s - \alpha_r) + \eta_{\alpha_i} \right) fZ, \quad i = 1, \dots, 20$$

4-13

Data for approach 2:

$$X_2 = \log \frac{B_{0_s}}{B_{0_r}} + \eta_{B_i} - ((A_s - A_r) + \eta_A) f^{(n_s - n_r) + \eta_{n_i}} - 4((\alpha_s - \alpha_r) + \eta_{\alpha_i}) fZ, \quad i = 1, \dots, 20$$

4-14

where  $i$  refers to an instance of noise and  $\eta$  indicates noise for each variable shown as a subindex. DP and LSQ were applied to the simulated spectra within a frequency range from  $f_l = 3.7$  MHz to  $f_2 = 7$  MHz similar to the experimental analysis bandwidth in our laboratory and using the following search ranges for both approaches:

$$(a_{s\_min} - 5)^2 - a_r^2 < a < (a_{s\_max} + 5)^2 - a_r^2$$

$$\alpha_{s\_min} - \alpha_r - 0.5 < \alpha < \alpha_{s\_max} - \alpha_r + 0.5$$

$$\log \left( 0.1 \frac{B_{s\_min}}{B_r} \right) < B < \log \left( 10 \frac{B_{s\_max}}{B_r} \right)$$

$$n_{s\_min} - n_r - 2 < n < n_{s\_max} - n_r + 2$$

$$A_{s\_min} - A_r - 2 < A < A_{s\_max} - A_r + 2$$

The general form of cost function contains two terms, data term, D, and regularization term, R, as follows:

$$C = D + R$$

4-15

where D and R for the first and second approaches are defined as follows:

$$D1 = \sum_{f_1}^{f_2} (X_1 - B + 0.827k^2a + 4\alpha fz)^2$$

4-16

$$D2 = \sum_{f_1}^{f_2} (X_2 - B + \mathbf{A}f^n + 4\alpha fz)^2$$

4-17

$$R1 = w_\alpha |\alpha_j - \alpha_{j-1}| + w_B |B_j - B_{j-1}| + w_a |a_j - a_{j-1}|$$

4-18

$$R2 = w_\alpha |\alpha_j - \alpha_{j-1}| + w_B |B_j - B_{j-1}| + w_A |A_j - A_{j-1}| + w_n |n_j - n_{j-1}|$$

4-19

where  $j$  refers to the  $j$ th depth.

### 4.3 Results

The results of approach 1 are shown in Figure 4-1. These results show that the variance of DP is on average 88%, 75% and 32% lower than that of LSQ for  $\alpha$ ,  $B$ , and  $a$ , respectively. In approach 2, we first set  $n$  to 2. The ground truth value of  $n$  in our simulations is also 2. Results are shown in Figure 4-2. Then, we set  $n$  to be a variable number and estimate it. The results are shown in Figure 4-3. These results show that the variance of DP is on average 75%, 100%, and 100% lower than that of LSQ for  $\alpha$ ,  $B$ , and  $A$ , respectively. When estimating four parameters, these improvements are 77%, 100% and 100%, 100% respectively for  $\alpha$ ,  $B$ ,  $n$  and  $A$ . Since LSQ does not have the regularization term to limit the estimates of parameters, the parameters get a substantially higher variance compared to DP. In addition, in DP, Eq. (4-7) and (4-11) are summed over the frequency range as well as depth in the recursion step. However, considering in LSQ there is no recursion step, the summation is only over the frequency range.

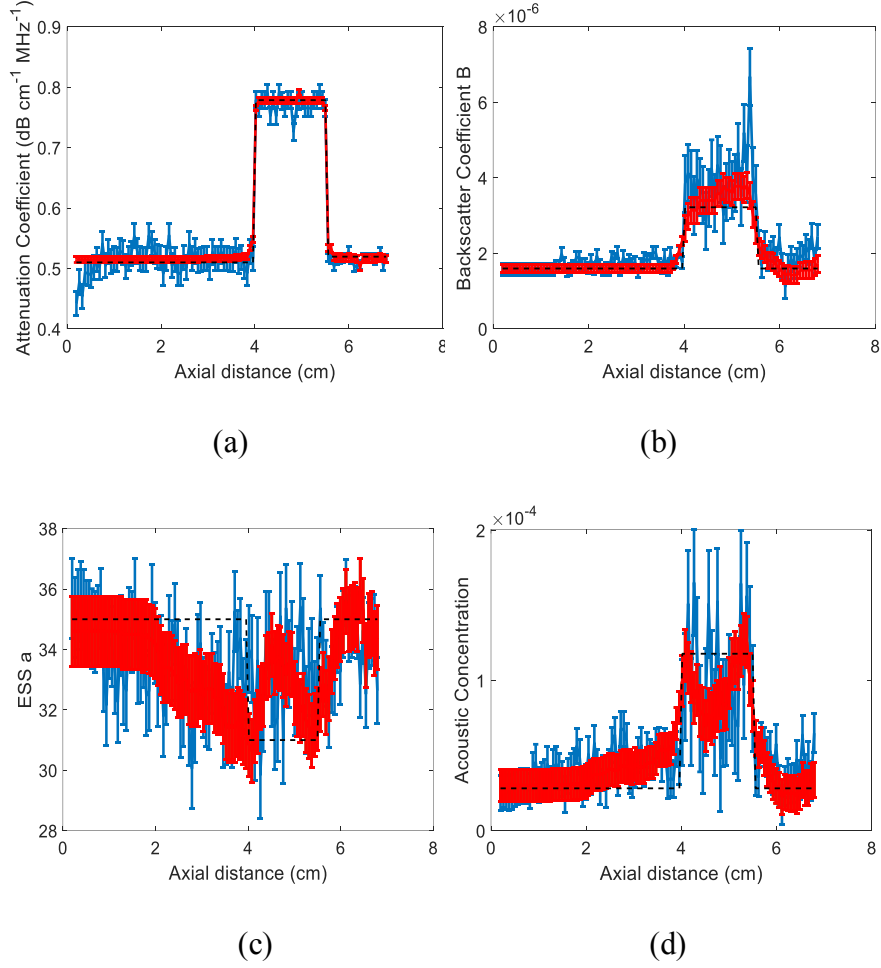


Figure 4-1 Results of LSQ (blue) and DP (red) methods using approach 1 in a simulated phantom with three layers and 20 instances of added zero-mean Gaussian noise. The error bars show the standard deviation over the 20 instances of noise for attenuation coefficient

The estimation results of Figure 4-1 (c) can be substantially improved if the frequency range is chosen such that  $ka \sim 1$ . In our simulations, the frequency for which  $ka=1$  for the two scatterer diameters simulated corresponds to 7.662 and 8.651 MHz, whereas the frequency range of this work was set to 3.7 to 7 MHz.

## 4.4 Conclusions

In this work, we presented two approaches based on RPM to parameterize backscattering in terms of form factor models. In the first approach, we assumed the Gaussian form factor and proposed DP to estimate ESS and AC. In the second approach, we used a more general form factor formulation which is appropriate for any impedance correlation functions. Here, we estimated

more parameters through DP and LSQ. Besides, in both approaches, we simultaneously estimated the attenuation coefficient. We observed DP substantially reduced variance of estimations compared to the LSQ.

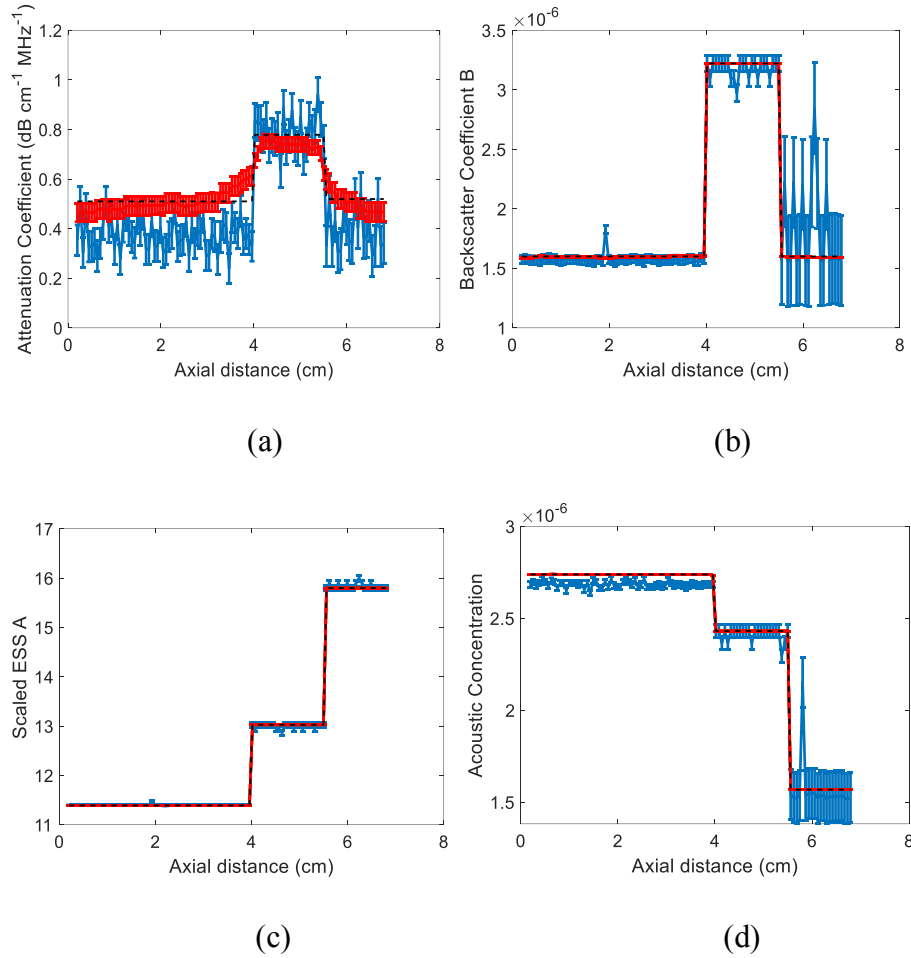


Figure 4-2 Results of LSQ and DP methods using approach 2 where  $n$  is fixed to 2 in a simulated phantom with three layers and 20 instances of added zero-mean Gaussian noise. The error bars in (a-c) show the standard deviation over the 20 instances of noise for attenuation coefficient (a), backscatter coefficient magnitude B (b), scaled ESS A (c), and acoustic concentration (d). The black dashed line is the known values.

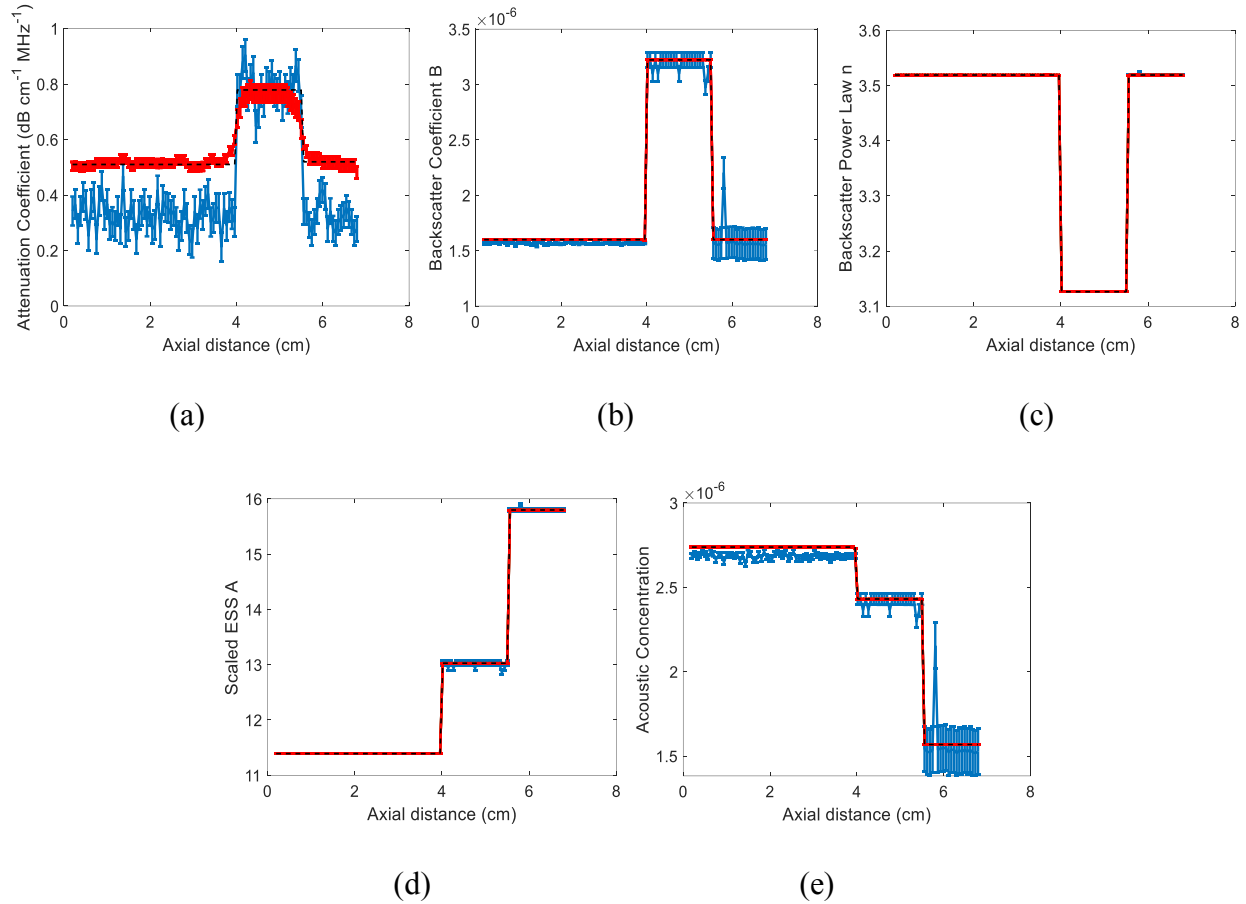


Figure 4-3 Results of LSQ and DP methods using approach 2 where  $n$  is not fixed to 2 and is estimated. The simulated phantom has three layers and 20 instances of added zero-mean Gaussian noise. The error bars show the standard deviation over the 20 instances of noise for attenuation coefficient (a), backscatter coefficient magnitude  $B$  (b), backscatter power law  $n$  (c), scaled ESS  $A$  (d), and acoustic concentration (e). The black dashed line is the known values.

## Chapter 5

# Evaluation of Contrast to Noise Ratio of Parametric Images of Regularized Estimates of Quantitative Ultrasound

This chapter is published in IEEE International Ultrasonic Symposium (IUS), 2020.

Here, we investigate whether parametric images of regularized estimates of the acoustic concentration can provide better conspicuity of high contrast objects than conventional B-mode images. To this end, we apply regularized estimation of acoustic concentration using DP to data acquired from a Gammex 410SCG phantom. The phantom contains three inclusions with different echogenicities, which are created from different concentration of scatterers. Conspicuity is quantified in terms of the inclusion CNR and border resolution. Our results demonstrate that using regularized QUS, the CNR of parametric images of the acoustic concentration was substantially higher CNR than those of conventional B-mode images, at the expense of border resolution.

### 5.1 Background

The application of QUS is usually based on creating parametric images, which visually represent the spatial variation of the estimated acoustic properties [30], [96]. Numerous researchers have employed parametric images to estimate scattering properties including the acoustic concentration [96], [97]. Two key steps to obtain parametric images of the AC are the removal of system-dependent effects (such as gains and focusing) and the compensation for intervening tissue attenuation. Our group recently developed a regularization strategy based on DP to compensate for system-settings and attenuation. We have previously shown that this strategy improves the accuracy and precision of QUS parameters [98].

Given that the acoustic concentration is a quantitative surrogate of tissue echogenicity, just like the brightness of the conventional B-mode image, here we investigate whether parametric images of the AC could provide better conspicuity of high contrast objects than conventional B-mode

images. To this end, we compare the CNR and border conspicuity of AC parametric images to those of B-mode images in a tissue mimicking phantom with cylindrical inclusions.

## 5.2 Methods

### 5.2.1 Data Acquisition

Two uncorrelated frames of raw RF echo signals were obtained from 8mm-diameter cylindrical inclusions (-6, +6, and +12dB more echogenic than the background) of a Gammex 410SCG phantom (Gammex-SunNuclear, Middleton, WI) with a Verasonics Vantage 128 system (Verasonics Inc., Kirkland, WA) using a L11-5v transducer operated at an 8MHz nominal center frequency.

### 5.2.2 Estimation of the Acoustic Concentration

A multi-taper technique [88] was used to compute a two-dimensional matrix of power spectra by slipping a 5mm×5mm window with 85% overlap over each frame laterally and axially, which yielded 103 rows and 55 columns of power spectra.

AC parametric images were constructed using the DP-based regularized approach that simultaneously compensates for attenuation [56] and estimates AC assuming a Gaussian form factor (Eqs. (4-7), (4-12)). The regularized strategy to estimate the AC is based on the RPM.

In addition, B-mode images were constructed from the log transform of the absolute value of the analytic echo signal without further compressing the dynamic range.

### 5.2.3 Comparison of Object Conspicuity

To compare object detectability between AC and B-mode images, we quantified the compromise between contrast and noise, as well as the border resolution. The CNR, was computed as:

$$CNR = \frac{\bar{p}_i - \bar{p}_{BGND}}{\sqrt{\sigma_i^2 + \sigma_{BGND}^2}}$$

where  $p$  refers to either AC or B-mode values,  $i=1, 2,$  or  $3$  for the  $-6\text{dB}, +6\text{dB}, +12\text{dB}$  inclusions, respectively, and the overbar and  $\sigma$  indicate the mean and standard deviation of  $p$  within  $5\times 5\text{mm}^2$  ROI within the inclusions and the background (BGND). The ROIs are shown in Figure 5-1.

To assess border conspicuity, we plotted three axial lines crossing through the center of each inclusion and measured the intensity of B-mode and parametric images on each line, and normalized by subtracting minimum value in each curve, and then dividing by the maximum value.

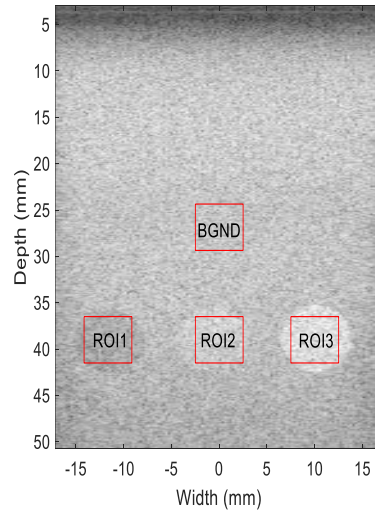


Figure 5-1 Location of regions of interest in B-mode image.

### 5.3 Results

Figure 5-2(a) and (b) show B-mode and AC images of the phantom with inclusions. Figure 5-3 shows the logarithmic scale of CNR for the three inclusions for the AC parametric image (red) and the B-mode image (blue). In all cases the value of CNR of the AC image is larger than the B-mode CNR by a factor ranging from 4.92 to 14.16.

Figure 5-4. represents the border conspicuity of the AC parametric image obtained with DP and the B-mode images for all inclusions. It can be seen that the border conspicuity of the B-mode image is better than that of the AC image.

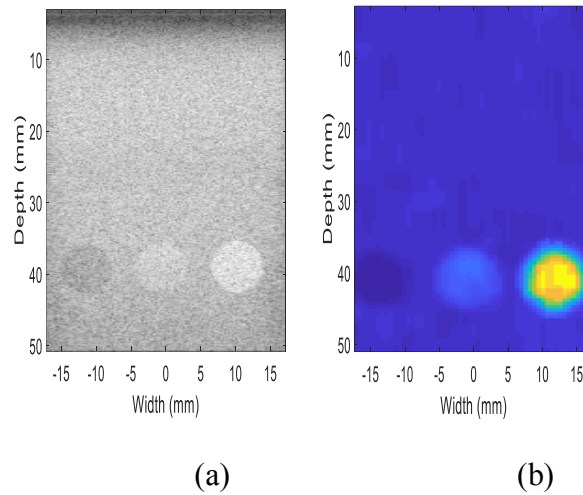


Figure 5-2 B-mode (a) and AC (b) images of the cylindrical inclusions

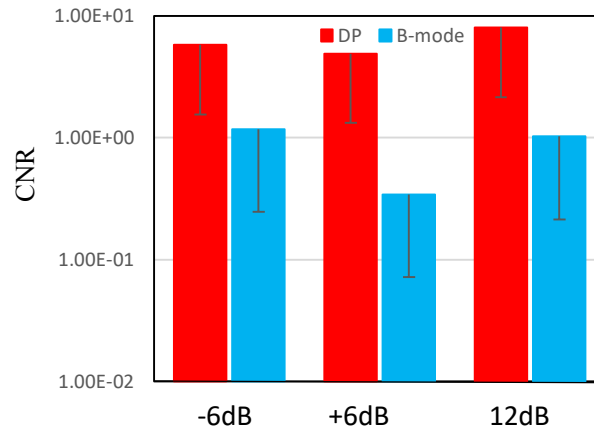


Figure 5-3 Logarithmic scale of CNR of cylindrical inclusions in B-mode and AC images obtained with DP. The error bars represent differences between the two frames.

## 5.4 Discussion and Conclusion

In this work, we evaluated whether parametric images of the DP-estimated AC provide better CNR and border resolution than the B-mode image. This could be helpful to show whether parametric images obtained with DP could be better options over B-mode images for the detection of objects with different echogenicities. To this end, we applied our state of art method [98] to data acquired from a Gammex 410SCG phantom and obtained the following results:

- Higher CNR for all inclusions in the AC parametric image compared to the B-mode image
- Better border resolution in the B-mode image compared to the AC parametric image obtained with DP.

Figure 5-3 shows that in the AC parametric image and B-mode image, +12dB and -6dB cylinders result in higher CNR, respectively and consequently, can be visualized more easily than other inclusions. This implies that the sequence of detectability of inclusions is different from B-mode image.

From Figure 5-4, we observe that using B-mode we can understand, where exactly are inclusions. In fact, wherever we see a jump (step change) in the intensity profile, it implies the region of inclusion starts or ends. On the other hand, from intensity profile of DP, the exact region of inclusions is not detectable. Instead, we see a transition (slope) from the background to the inclusions, which is due to the finite size of the estimation region (5mm×5mm) in the power spectra. Therefore, even in the AC images, the common tradeoff between CNR and resolution is present.

Here, we studied “easy-to-detect” objects. However, to assess the quality of an image and estimate the contrast of an object, a contrast-detail (CD) analysis is required, where well-trained observers view different diameter of objects to select the smallest visible one and form a CD curve [99], [100].

The work presented here is an initial step towards future studies that will analyze the tradeoff between CNR and border resolution in more complex structures. Furthermore, we will extend the analysis to parametric images of the effective scatterer diameter.

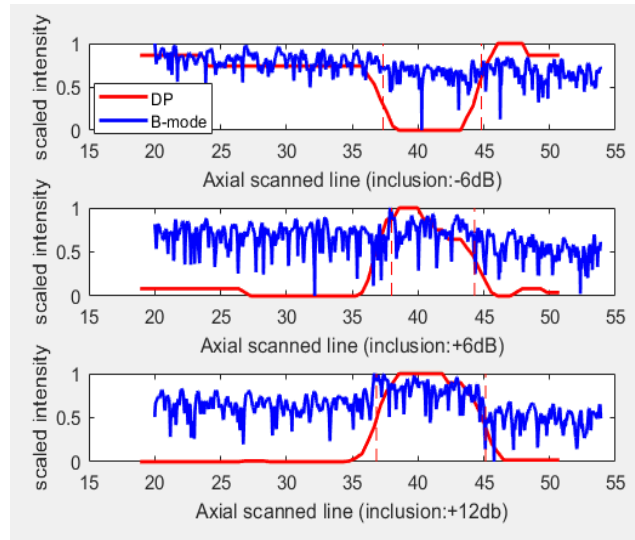


Figure 5-4 Scaled border resolution of cylindrical inclusions in B-mode and AC images obtained with DP. The vertical lines indicate, where each inclusion starts or ends.

## Chapter 6

# Analytical Globally-Regularized Estimation of Effective Scatterer Diameter and Acoustic Concentration in Quantitative Ultrasound

This chapter is published in IEEE International Symposium on Biomedical Imaging (ISBI), 2021.

Herein, we propose a novel technique to analytically estimate the effective scatterer diameter and the acoustic concentration using simultaneous attenuation compensation. We show that our proposed technique substantially outperforms a recently-proposed, DP based method, and is 100 times faster.

### 6.1 Background

Our group has recently proposed a regularized method to estimate ESD and AC using DP [101]. DP can provide accurate and precise estimation subject to appropriate pre-defined search ranges of ESD and AC values. The search ranges correspond to each feature that needs to be estimated which must be defined around optimized values served as the ground truth if it is applicable. In the cases where the ground truth is unknown, the search range should be defined wide enough to assure it contains the range of values expected for the tissue under characterization. In addition, DP is a discrete estimation method because the search ranges are divided into discrete step sizes. Accordingly, the smaller the step size and the wider the search range, the larger the computational burden, which could impede real time clinical implementation. To tackle these difficulties, we propose a novel analytical strategy to estimate ESD and AC that does not depend on search ranges and step sizes, and that is faster than DP. The novel method is compared to DP in simulated echo signals. Because a similar analytical strategy, referred to as ALGEBRA [91], was proposed for the quantification of BSC, we referred to the new method as ALGEBRA<sub>ESD</sub>.

### 6.2 Methods

We employ the RPM [83], a common and well known framework in the area of QUS to remove diffraction and system effects. We intend to exploit the spectrum normalization performed in the

RPM to simulate its real applications which is done usually for experimental data. The RPM normalizes the power spectrum of a sample phantom  $s$  (or tissue in a clinical application) with unknown acoustic properties by the spectrum of a reference phantom  $r$  with well-defined acoustic properties and similar sound speed to that of the sample. The sample and the reference should be scanned with the same system settings.

Performing the similar strategy described in Chapter 4 as well as employing the original ALGEBRA, in ALGEBRA<sub>ESD</sub>, we solve the following cost function analytically, as both  $D$  and  $R$  are quadratic in terms of the unknowns. Therefore, by taking the derivatives with respect to  $b$ ,  $d$ , and  $a$ , and set them to zero we have:

$$C = D + R \tag{6-1}$$

$$D = \sum_{l=1}^{N_F} \sum_{i=1}^{N_R} (X(f_l, z_i) + b(z) - 0.827k^2d(z) - 4a(z)fc)^2 \tag{6-2}$$

$$R = \sum_{p=1}^3 \sum_{i=2}^{N_R} w_p (p_i - p_{i-1})^2 \tag{6-3}$$

where  $i$  and  $l$  refer axial location and frequency indices, respectively. Index  $p$  refers to the three parameters ( $p=1$  for  $a$ , 2 for  $b$ , and 3 for  $n$ ) and  $w_p$  is the regularization weight for parameter  $p$

Doing this, leads to having the following equation, where  $\mathbf{F}$  is a square matrix,  $\mathbf{T}$  is a vector composed of three  $3N_R$  vectors, T1, T2, and T3, and the goal is to estimate  $\mathbf{Y}$ , a vector with  $3N_R$  elements containing all parameters that should be estimated as follows.

$$\mathbf{FY} = \mathbf{T} \tag{6-4}$$

$$\mathbf{T} = \begin{bmatrix} \mathbf{T1} \\ \mathbf{T2} \\ \mathbf{T3} \end{bmatrix},$$

6-5

where  $i^{\text{th}}$  components are as follows:

$$T1_i = -4z_i \sum_{l=1}^{N_F} X(f_l, z_i) f_l,$$

$$T2_i = \sum_{l=1}^{N_F} X(f_l, z_i),$$

$$T3_i = -0.827 \sum_{l=1}^{N_F} X(f_l, z_i) k_i^2.$$

6-6

$$\mathbf{Y} = [a_1, \dots, a_{N_R}, b_1, \dots, b_{N_R}, d_1, \dots, d_{N_R}]^T.$$

6-7

As a result, we estimate all parameters for all depths at once, which leads to improved results especially for noisy regions of the image. We tested ALGEBRA<sub>ESD</sub> and compared it to DP by applying both methods to a simulated power spectra array containing 74 rows ( $N_R$ ) and 20 columns ( $N_C$ ).

The power spectra were mathematically computed. The simulated phantom contains two layers, each 37 mm deep, with the following properties:  $\beta_s = [112.6, 285.1] \times 10^{-8} \text{ cm}^{-1} \text{ sr}^{-1} \text{ MHz}^{-4}$ ,  $\delta_s = [50, 60] \text{ }\mu\text{m}$ ,  $\alpha_s = [0.5, 0.6] \text{ dB cm}^{-1} \text{ MHz}^{-1}$ , where the first and the second elements of the vector corresponds to the values in the first and second layers, respectively. Furthermore, the physical properties of the reference phantom are  $\beta_r = 4.4 \times 10^{-8} \text{ cm}^{-1} \text{ sr}^{-1} \text{ MHz}^{-4}$ ,  $\delta_r = 30 \text{ }\mu\text{m}$ ,  $\alpha_r = 0.59 \text{ dB cm}^{-1} \text{ MHz}^{-1}$ . We generated the normalized power spectra by adding white Gaussian noise to  $b$ ,  $d$ , and  $a$  in Eq. (5) as follows:

$$X = b + n_{b_i} - 0.827k^2(d + n_{d_i}) - 4(a + n_{a_i})fz, i = 1, \dots, 20$$

6-8

where  $n$  refers to white Gaussian noise for each parameter indicated as a sub-index, and  $i$  represents each instance of noise.

To keep the representative results comprehensible, we calculate the local attenuation from the effective attenuation using Eq. 2-32.

### 6.3 Results

Figures 6-1 to 6-3 show parametric images of the ESD, AC, and local attenuation estimation in the simulated phantom obtained using  $ALGEBRA_{ESD}$  (b) and DP (c). It can be clearly observed that, the results of  $ALGEBRA_{ESD}$  agree well with the ground truth (a) and substantially outperform DP. To have quantitative assessments, we calculate the ratio of all estimated and ground truth values and then computed the minimum and maximum value of this ratio. Clearly, in this assessment, a method performs well when both min and max values are close to one. Accordingly, the min and max values are as follows using  $ALGEBRA_{ESD}$  and DP, respectively. For ESD estimation we get [0.93, 1.08] and [0.75, 1.3], for AC estimation [0.61, 1.6] and [0.21, 6.7], and for local attenuation [1, 1] and [0.98, 1.02]. In addition, the analytical estimation is substantially faster than DP. The estimation of QUS parameters using proposed method and DP required 0.711 sec and 103.1 sec, respectively. Both methods were executed with Matlab R2018a (MathWorks, USA) on an Intel Core i5-6500 CPU.

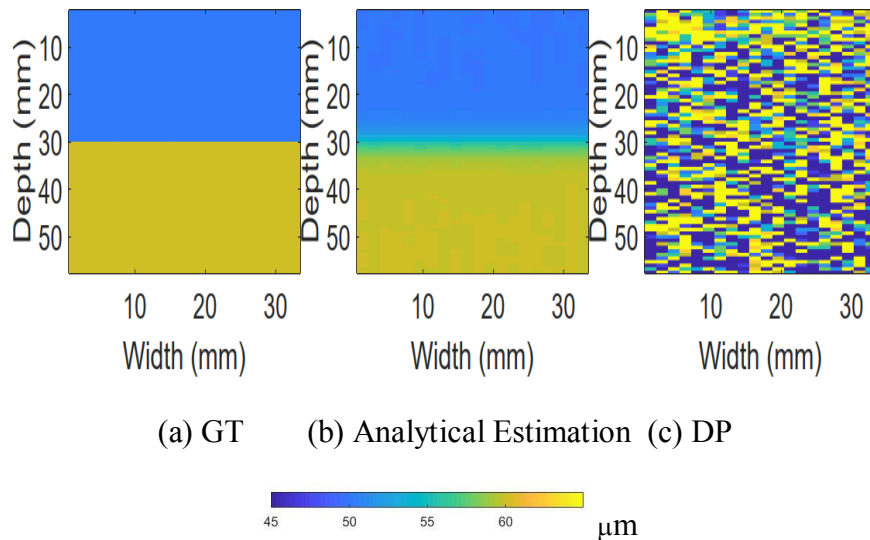


Figure 6-1 Parametric image of ESD.

## 6.4 Discussion

Theoretically, we expect the results of  $AGLEBRA_{ESD}$  to be same as DP as both approaches aim to minimize the identical cost function. However, the quantization of the search ranges in DP reduces the accuracy and precision of the estimated values. On the other hand, if we select the step sizes in the DP very small such that it approaches the continuous search ranges, it leads to a very high computational complexity. In contrast, the analytical estimation we introduced here does not only improve the results in terms of accuracy and precision, but also it is computationally efficient which makes it a suitable option in real-time QUS applications.

## 6.5 Conclusions

Herein, we proposed a novel method to analytically estimate the ESD and AC called  $ALGEBRA_{ESD}$ . We applied the method to 20 samples of the simulated noisy normalized spectra, and observed that  $ALGEBRA_{ESD}$  substantially outperformed the DP strategy recently proposed by our group [101].  $ALGEBRA_{ESD}$  was also substantially faster than DP, which is important in several clinical applications. In the future, we intend to apply our proposed method to more complex phantoms that reflect characteristics of real tissue. Furthermore, we will compare the analytical approach to iterative approaches using the nonlinear solvers such as NelderMead Simplex and Bayesian Optimization.

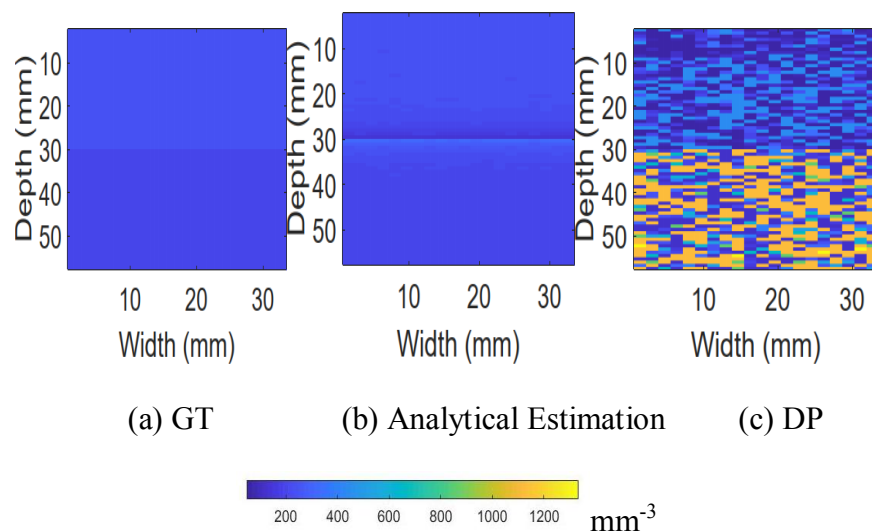


Figure 6-2 Parametric map of AC. the GT values are 236, 200 in the first and second layers, respectively.

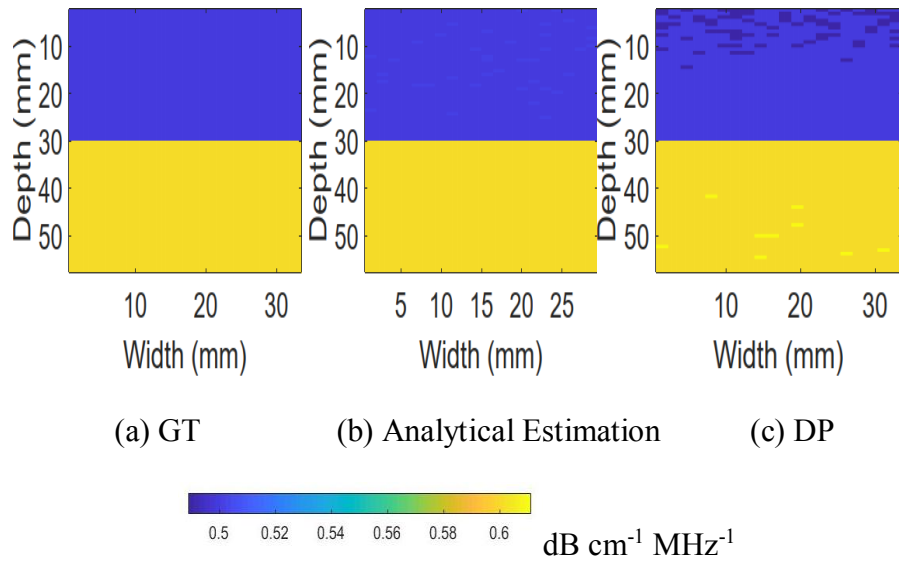


Figure 6-3 Parametric image of local attenuation.

## Chapter 7

# Scatterer Size Distribution Estimation in Quantitative Ultrasound using Constrained Optimization

This chapter is under review in *Ultrasonic Imaging*, 2022, and published in *International Symposium on Ultrasonic Imaging and Tissue Characterization (UITC) 2021, 2022*, and *IEEE International Ultrasonic Symposium (IUS)*, 2021.

Herein, we propose a novel strategy to estimate a distribution showing the contribution of different scatterer sizes. We conduct the estimation using a linear combination of the backscatter coefficient (BSC) for each scatterer size forming the resulting BSC. We perform the estimation by optimizing a constrained cost function solved using convex optimization and validate our method on four ground truth distributions. Results on simulated Gaussian (two phantoms), uniform (one phantom), and bi-modal (one phantom) distributions suggest that our proposed method can provide a good estimation for the scatterer size distribution.

### 7.1 Background

In order to gain characteristic information about tissue microstructure, backscattered echo signals can be parametrized with form factors to obtain the QUS parameters such as ESD [25]. The form factor represents the variation of the frequency dependence part of the backscattered signal from Rayleigh scattering and it is proportional to the spatial Fourier transform of the variations of acoustic impedance that constitute the scattering sources [25]. Extracting microstructure information from the form factors is feasible if the scatterer's radius is not too small or too large compared to the wavelength [102]. In other words, it is known that the wave number  $k$  multiplied by the radius of the scatterer  $a$  needs to be between 0.6 to 1.2 [25]. Therefore, this limitation in estimating the scatterer size should be taken into account meaning that it is not possible to estimate all the scatterers' radii within a medium.

Shape and scatterer size distribution affect RF data [103]. The impact of aggregate size distribution on backscattered data has been investigated in publications such as [104], [105]. Furthermore, analyzing scatterer size distribution can conduct us to deduce the tissue microstructure.

Diseases typically affect the distribution of scatterers in tissues. Besides, the distribution of sizes is wide in diseases such as aggregated red blood [106] and diffuse renal disease [107]. Accordingly, the proposed method should allow the scatterer's size distribution to be quantified in order to provide a comprehensive characterization of tissue. Consequently, herein, our aim is to estimate the contribution of each scatterer's size within the media that satisfies the condition  $0.6 \leq ka \leq 1.2$ .

## 7.2 Materials and Methods

Let the frequency-dependent part of the BSC for each scatterer size be  $BSC_a(f)$ , where sub index  $a$  indicates scatterer radius, and  $x$  represent the contribution of each size within  $BSC_a(f)$ . The resulting BSC for entire sizes is  $BSC(f)$  defined as follows:

$$BSC(f) = \sum_a x_a BSC_a(f) \tag{7-1}$$

The equivalent version in matrix format is:

$$A x = b \tag{7-2}$$

where  $A$  is the bank of BSC for individual sizes with  $N_F$  rows referring to the number of frequency bins and  $N_S$  columns representing the length of the scatterer size range.  $b$  is a column vector showing the compounded BSC with  $N_F$  elements and  $x$  contains  $N_S$  entries illustrating the contribution of each BSC for individual sizes. We propose to optimize the following cost function  $C$ :

$$C = ||Ax - b|| \tag{7-3}$$

where  $||\cdot||$  refers to norm 2. To minimize Eq. (7-3), we exploit the CVX toolbox [108] in Matlab R2018a. The CVX modeling system provides a framework to find a solution for convex optimization. It allows the constraints to be defined using Matlab syntaxes. Herein, the CVX constrains  $x$  to nonnegative values. In other words, the weight of a scatterer size cannot be negative.

An important point that should be taken into account is that there is a limitation in estimating scatterer size. To extract scatterer properties including ESD, for a known frequency range, the inequality of  $0.6 \leq ka \leq 1.2$  needs to be satisfied.

We divide the problem into two parts, the forward problem, and the inverse problem. In the forward problem, for a given frequency range, the matrix  $A$  is generated, then assuming a distribution called  $GT_f$  (ground truth in the forward problem), vector  $b$  is made using Faran theory without considering any limitations. In the inverse problem phase, we define a search range with the acceptable  $0.6 \leq ka \leq 1.2$  scatterer size taken into account when recovering the contribution of different diameters.

As the matrix  $A$  is not necessarily full rank, reducing the number of columns (number of bins for scatterers sizes) will reduce the number of unknowns, rendering  $A$  a full rank matrix with a unique solution for the linear equation. As a result, a step size for scatterer size is specified, and the ignored columns are expected to be added to the closest acceptable column (scatterer size). Besides, the probability corresponding to the sizes that cannot be estimated is summed to the probability of the closest size that can be estimated which forms the GT in the inverse problem ( $GT_i$ ).

### **7.2.1 Data**

Four simulated phantoms are used to validate our proposed algorithm, with the distributions of scatterer sizes assumed to be Gaussian (two phantoms,  $N(60, 64)$ ,  $N(40, 64)$ ), uniform (one phantom  $U(31, 70)$ ), and bi-modal (one phantom, summation of two Gaussian  $N(60, 64) + N(140, 25)$ ). The phantoms used for *in silico* validation consist of 200 grams of glass beads in a 1.6L volume of water-based gel with different scatterer size distributions. The simulated frequency range is from 3 to 9MHz. The ESD for the first Gaussian, second Gaussian, uniform, and bi-modal distributions are  $64\mu\text{m}$ ,  $46\mu\text{m}$ ,  $70\mu\text{m}$ , and  $141\mu\text{m}$ , respectively.

### **7.2.2 Frequency range**

Herein, we applied the following criterion to select the frequency range: For a known frequency range (here, 3 to 9 MHz) we plot the BSC and determine the corresponding frequency where the plot starts to become flat. More precisely, we take the derivative of the BSC in the linear scale and, specify the cut-off frequency where the derivative of BSC becomes 0.004. Figure 7-1 manifests

the BSC of the uniform distribution in the logarithmic scale. The blue line shows the BSC for the total frequency range and the red line depicts the cut-off frequency as 7.1.

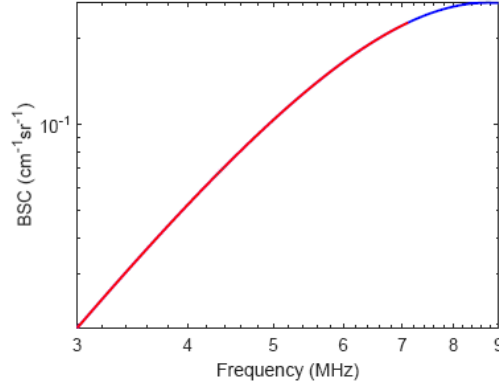


Figure 7-1 Logarithmic scale of the BSC for the uniform distribution, the cut-off frequency = 7.1.

As a simulation of the instrument noise present in real measurements, we corrupt the calculated BSC with additive Gaussian noise. To test the robustness of our method against uncertainties, we added two levels of zero mean Gaussian noise to the resulting BSC in Eq. (7-1). Therefore, the equation will be modified as:

$$BSC(f) = \sum_a x_a BSC_a(f) + n_f$$

7-4

where  $n_f$  is zero mean Gaussian noise. The low level of additive Gaussian noise in Eq. (4) for the first Gaussian, second Gaussian, uniform, and bi-modal distributions are  $N(0, 10^{-3})$ ,  $N(0, 10^{-3})$ ,  $N(0, 3 \times 10^{-4})$ ,  $N(0, 3 \times 10^{-2})$ , respectively. The variance of the high level of noise is 10 times higher than the corresponding low level of noise.

### 7.2.3 Quantitative analysis

In addition to qualitatively comparing the GT and the estimated distributions, we measure the root mean square error (RMSE) to quantitatively assess our results. To do so, we calculate RMSE for the estimated histogram from clean signal and noisy signals and denote them as  $RMSE_c$  and  $RMSE_n$ , respectively. RMSE is defined as follows:

$$RMSE = \sqrt{\frac{1}{M} \sum_i (\hat{D}_i - D_i)^2}$$

7-5

where  $D_i$ , and  $\hat{D}_i$  refer the ground truth of the contribution  $x$  for the  $i^{th}$  diameter in the inverse problem, and the estimated diameter, respectively and  $M$  denotes the total number of diameter bins in the estimation problem.

Furthermore, to compare the estimated histogram and the GT, we report the earth mover's distance (EMD) [109]. EMD corresponds to the minimum amount of work needed for one distribution to be transformed into another. More precisely, it is proportional to the area between two cumulative density functions (CDF). We calculate EMD between the GT and the estimated histogram from the clean signal as well as noisy signals and represent them as  $EMD_c$  and  $EMD_n$ .

### 7.3 Results and Discussion

Figures 7-2(a) to 7-5(a) show the GTs fed to the Faran code in the forward problem ( $GT_F$ ) and Figures 7-2(b) to 7-5(b) compare the estimation from noiseless signal shown in red with the GT in the inverse problem ( $GT_i$ ) illustrated in blue. Figures 7-2(a) and 7-3(a) present two Gaussian distributions. The distribution in Figure 7-2(a) only contains a few diameters that cannot be estimated (i.e., less than  $43\mu\text{m}$ ) while the second distribution in Figure 7-3(a) contains more sizes that are not within the  $0.6 \leq ka \leq 1.2$  range. The  $ka$  range for the first Gaussian, second Gaussian, uniform, and bi-modal distributions in the forward problem phase are between  $[0.006, 2.67]$ ,  $[0.006, 3.59]$ ,  $[0.006, 2.83]$ , and  $[0.006, 2.87]$ , respectively.

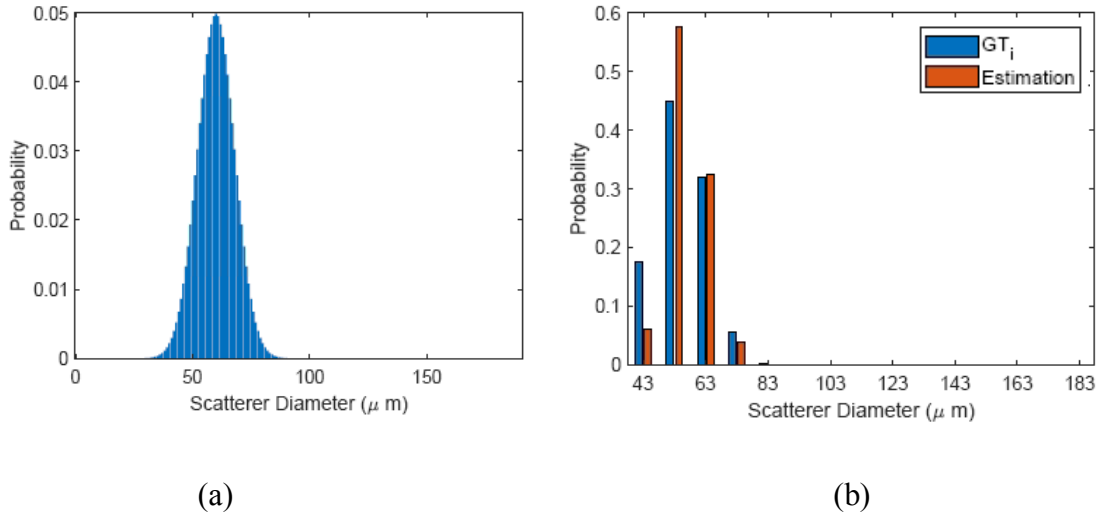


Figure 7-2  $GT_f$ , Gaussian1 distribution (a), Comparison of estimation (red bars) and  $GT_i$  (blue bars).

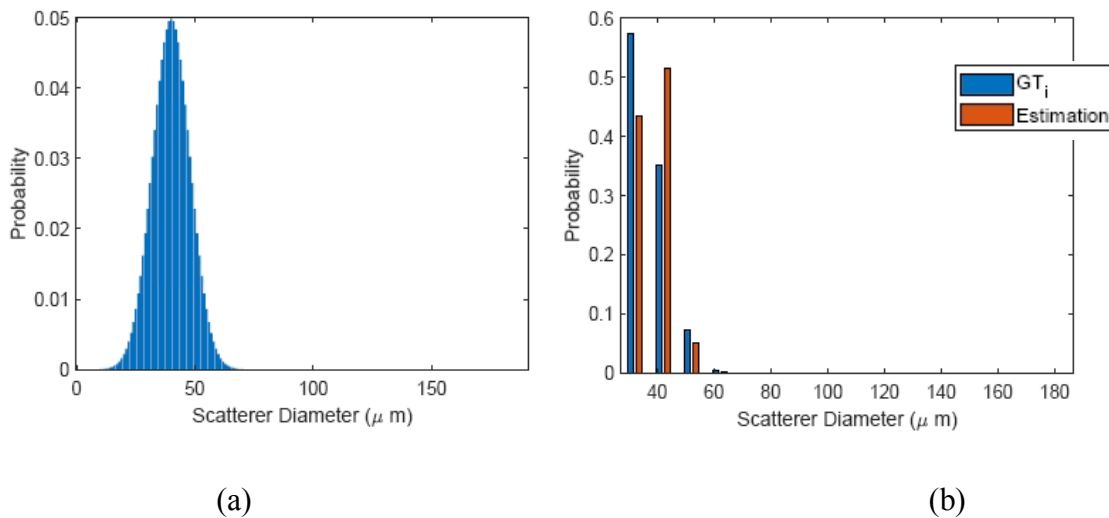


Figure 7-3  $GT_f$ , Gaussian2 distribution (a), Comparison of estimation (red bars) and  $GT_i$  (blue bars).

Figure 7-4(a) demonstrates a uniform distribution and Figure 7-5(a) shows a bi-modal distribution. Figure 7-5(b) demonstrates that our method can detect the two peaks in the bi-modal distribution. Figures 7-6 to 7-9 demonstrate the estimations from the clean signal and noisy signals for the same  $GT_f$ , depicted in Figures 7-2(a) to 7-5(a). The variance of noise in Figures 7-6(b) to 7-9(b) is ten times higher than Figures 7-6(a)-7-9(a). Visual comparison shows that adding a higher level of noise leads to higher error.

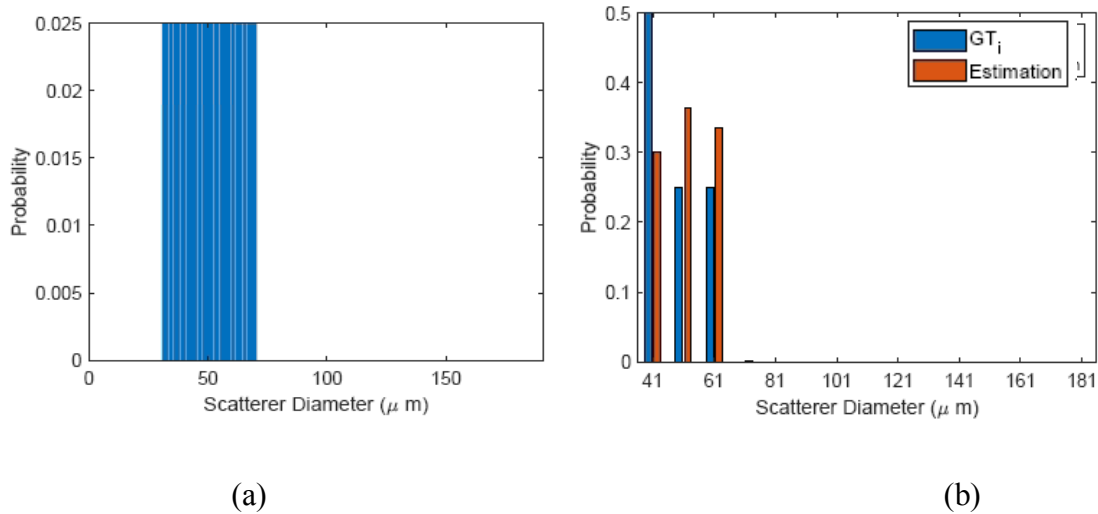


Figure 7-4  $GT_f$ , uniform distribution (a), Comparison of estimation (red bars) and  $GT_i$  (blue bars).

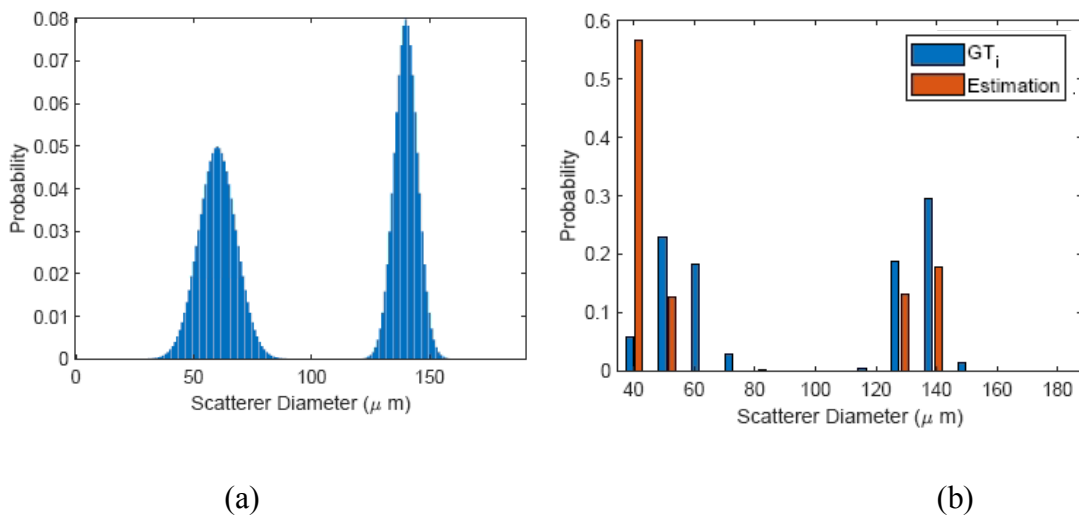
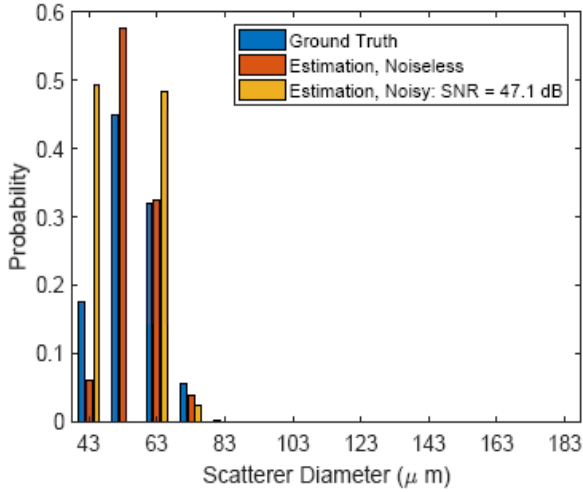
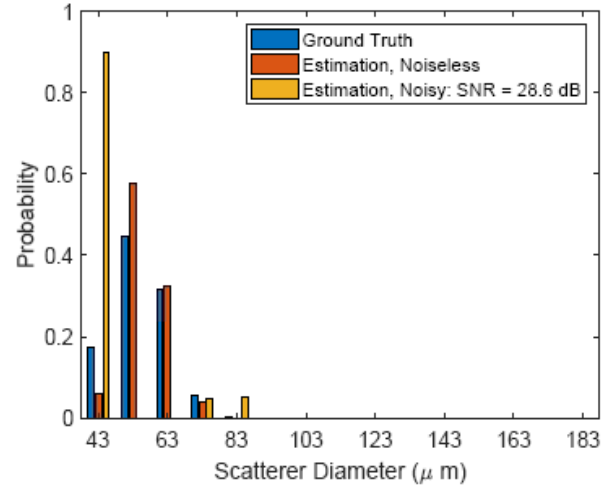


Figure 7-5  $GT_f$ , bi-modal distribution (a), Comparison of estimation (red bars) and  $GT_i$  (blue bars)

The quantitative assessment in Table 7-1 illustrates the ratio of  $RMSE_{nl}$  and  $RMSE_{nh}$  with respect to the  $RMSE_c$  (subscripts nl, nh and c respectively refer to low noise, high noise and clean). These results show that increasing the noise variance by a factor of ten yields a modest increase in RMSE. In Table 7-2, the uncertainty in  $RMSE_{nl}$  and  $RMSE_{nh}$  with respect to the  $RMSE_c$  over the different realizations of low and high noise is shown. The uncertainty in  $RMSE_{nh}$  with respect to the  $RMSE_c$  is lower than  $RMSE_{nl}$  with respect to the  $RMSE_c$  in all distributions meaning that  $RMSE_{nh}/RMSE_c$  in Table 7-1 is more precise than  $RMSE_{nl}/RMSE_c$ .

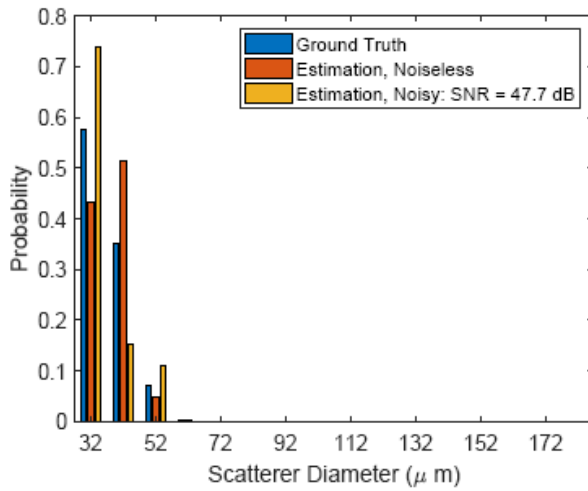


(a)

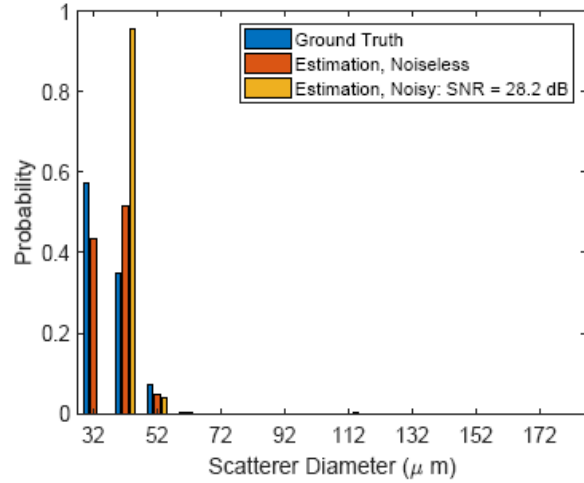


(b)

Figure 7-6 Comparison of estimations from the noiseless signal (red bars), noisy signals (yellow bars), and  $GT_i$  (blue bars) for Gaussian1 distribution. The variance of noise in (b) is 10 times higher than (a).

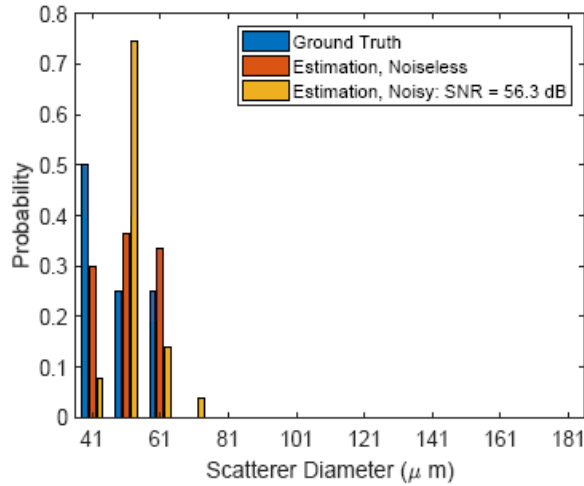


(a)

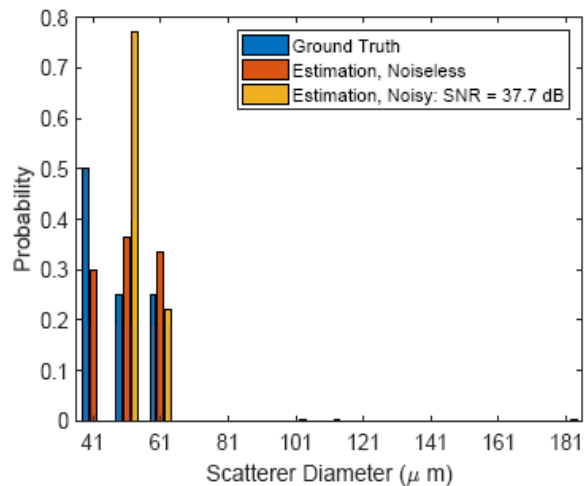


(b)

Figure 7-7 Comparison of estimations from the noiseless signal (red bars), noisy signals (yellow bars), and  $GT_i$  (blue bars) for Gaussian2 distribution. The variance of noise in (b) is 10 times higher than (a).

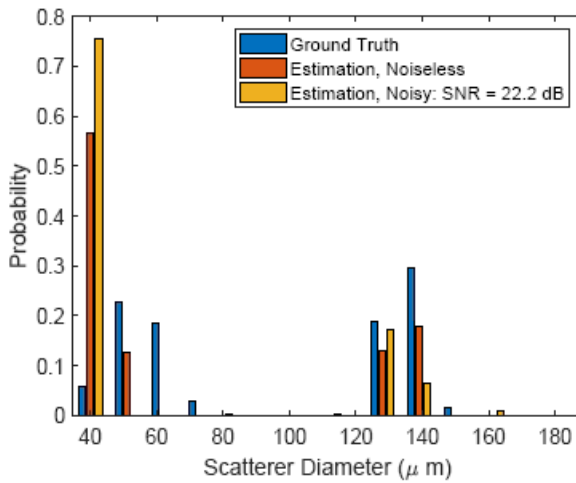


(a)

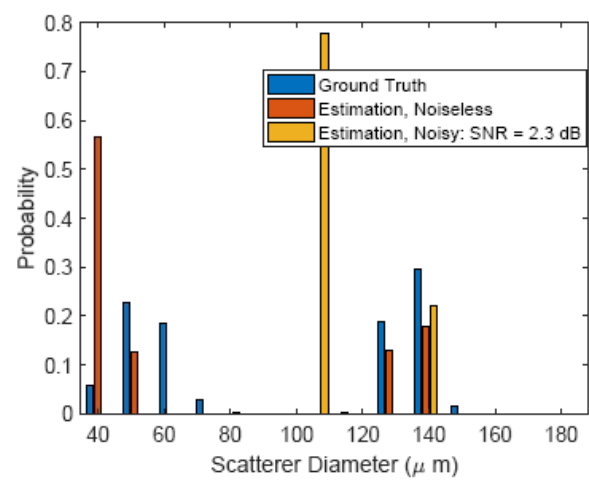


(b)

Figure 7-8 Comparison of estimations from the noiseless signal (red bars), noisy signals (yellow bars), and  $GT_i$  (blue bars) for the uniform distribution. The variance of noise in (b) is 10 times higher than (a).



(a)



(b)

Figure 7-9 Comparison of estimations from the noiseless signal (red bars), noisy signals (yellow bars), and  $GT_i$  (blue bars) for the bi-modal distribution. The variance of noise in (b) is 10 times higher than (a).

Table 7-1 Quantitative comparison of  $RMSE_{nl}$  and  $RMSE_{nh}$  respect to the  $RMSE_c$ , where sub index nl, nh, and c refer to the low noise, high noise, and clean signal

	$RMSE_{nl}/RMSE_c$	$RMSE_{nh}/RMSE_c$
Gaussian 1	3.3242	5.2678
Gaussian 2	1.1972	3.8166
Uniform	2.6972	2.9538
Bi-modal	1.4001	1.5222

Table 7-2 Uncertainty in  $RMSE_{nl}$  and  $RMSE_{nh}$  respect to the  $RMSE_c$ , where sub index nl, nh, and c refer to the low noise, high noise, and clean signal.

	$RMSE_{nl}/RMSE_c$	$RMSE_{nh}/RMSE_c$
Gaussian 1	0.3914	0.1694
Gaussian 2	0.5523	0.3273
Uniform	0.3616	0.2835
Bi-modal	0.0638	0.0604

EMD values between the ground truth and estimated distributions are shown in Table 7-3. These results are also aligned with the results of Table 7-1, showing modest increases in EMD with a ten-fold increase in the noise variance. In Table 7-4, the uncertainty in  $EMD_{nl}$  and  $EMD_{nh}$  over the different realizations of low and high noise is presented.

Table 7-3 Quantitative comparison of  $EMD_c$ ,  $EMD_{nl}$ , and  $EMD_{nh}$ , where sub index nl, nh, and c refer to the low noise, high noise, and clean signal.

	$EMD_c$	$EMD_{nl}$	$EMD_{nh}$
Gaussian 1	1.4893	4.8605	10.9687
Gaussian 2	1.6596	2.0355	6.3210
Uniform	2.8585	5.3706	5.6230
Bi-modal	24.4895	32.5822	32.6630

Comparison of Table 7-1 with Table 7-2 and Table 7-3 with Table 7-4 illustrates although the estimation in the bi-modal distribution is not accurate, it is precise.

Table 7-4 Uncertainty in  $EMD_{nl}$ , and  $EMD_{nh}$ , where sub index nl and nh refer to the low noise and high noise.

	$EMD_{nl}$	$EMD_{nh}$
Gaussian 1	0.2540	0.6044
Gaussian 2	0.9063	0.5556
Uniform	0.6409	0.6754
Bi-modal	1.1233	0.9091

The distribution of the scatterer sizes can vary during a disease. A tumor can cause aggregate size distributions in thyroid follicles [110] or aggregate red blood cells can occur in diabetics [111]. Therefore, reporting the scatterer size distribution is important for clinical purposes especially when the medium contains a wide range of sizes. In preliminary work [112], we estimated the distribution of sizes in two steps. In this work, we introduced a novel method to optimize a constrained cost function and tested the robustness of our technique by adding the Gaussian noise to the resulting BSC. Qualitative and quantitative evaluations of the results exhibit that our method

can provide a good estimation of the contribution of the scatterer sizes in terms of RMSE and EMD.

Our approach facilitates the estimation of the scatterer size distribution for a full rank matrix. Hence, in the inverse problem phase, we converted the initial matrix into a full rank matrix by combining its columns. A possible future work can deal with reconstructing the contribution for each size from the representing size.

## 7.4 Conclusions

Herein, we proposed a novel technique to estimate the scatterer size distribution instead of estimating a single effective size. Our approach is based on minimizing a constrained cost function optimized using the CVX toolbox in Matlab. We considered the acceptable  $ka$  range in the estimation of sizes and tested our proposed method on Gaussian, uniform, and bi-model distributions. Results suggest that we can apply the method to phantom data in future work.

# Chapter 8

## Conclusions and Future Work

### 8.1 Conclusions

In this thesis, we proposed novel QUS techniques to estimate average attenuation, BSC, and scatterer properties to quantify tissue microstructures. Previous work in this field can be categorized into two classes. This first class introduces novel techniques to estimate QUS parameters, while the second class incorporates these techniques into clinical scanners and commercializes them. Three QUS parameters have been commercialized clinically, namely average attenuation, backscattering, and sound speed, but more work remains to be done.

Our study focused on the first class, and we presented novel techniques in each chapter to improve the estimation of the average attenuation, BSC, ESD, AC, and scatterer size distribution. In Chapter 2, we proposed two versions of a novel technique called 1D-ALGEBRA and 2D-ALGEBRA to estimate the average attenuation and BSC. Unlike DP, the ALGEBRA technique removes the restriction of a discrete grid of parameter values over which the cost function is minimized. Therefore, continuous estimations of the attenuation and backscatter parameters are obtained. ALGEBRA optimizes a regularized cost function analytically, providing estimates much more accurately, precisely, and faster than previously presented techniques, such as the LSQ and DP, which is essential for clinical use where near real-time performance is invaluable. The regularization term in ALGEBRA is based on the  $L2$  norm. Vajihi *et al.* [113] showed that the use of the  $L1$  norm in the regularization terms provides better precision in parameter estimates than the use of the  $L2$  norm. However, the  $L1$  norm is not analytically differentiable so it could not be implemented in the ALGEBRA. Moreover, each frequency and depth of the power spectrum have the same contribution in the ALGEBRA method. Taking into consideration these shortcomings leads us to introduce a novel technique. In Chapter 3, the  $L1$  and  $L2$  norms in the regularization parts of the cost function were incorporated based on the physics of the BSC and average attenuation. Besides, we introduced a weight for each depth and frequency of power spectra multiplied by the data term according to the noise level of power spectra. In the end, we penalized

the cost function using ADMM. In Chapter 4, we modified the linear equation in [56] and considered different scattering models, such as form factors for different scatterer geometries, to estimate the ESD and AC as well as simultaneously estimate attenuation coefficients optimized using DP. To do so, we presented two approaches. In the first approach, we exploited the Gaussian form factor, while in the second approach, we assumed a more general form factor equation, which is suitable for any impedance correlation function. It should be mentioned that in the second approach we estimated more parameters compared to the first approach.

As a possible application of our method described in Chapter 4, Chapter 5 investigates to answer the question that whether the parametric image of the AC obtained using DP provides better contrast in detecting high-contrast objects or the conventional B-mode images. To respond to this question, two criteria were utilized, CNR and border resolution. CNR voted for the parametric image of the AC, whereas the border resolution selected the B-mode image.

Noting the drawbacks of DP as well as to benefit from the concept of analytical estimation introduced in Chapter 2, in Chapter 6, we proposed a novel method called  $\text{ALGEBRA}_{\text{ESD}}$ . The method employs the same linear equation in Chapter 4 to estimate ESD and AC analytically. However, when a media contains a wide range of sizes, reporting a single ESD cannot tell the whole story about the media. Therefore, in Chapter 7, we presented a cost function minimized using CVX toolbox in Matlab to estimate scatterer size distribution. The estimated probability of each scatterer size represents its contribution in forming the BSC. The qualitative and quantitative comparisons in each chapter justify that our proposed algorithms outperform the other techniques.

## 8.2 Future Work

Whether our proposed methods would perform well in clinical trials and real tissue data is an interesting question. As a result, testing our techniques on tissue data can be regarded as the first step towards clinical validation of each technique.

Our regularized-based techniques require adjusting regularization weights for each phantom experiment. In general, larger weights are used in phantoms in which there is no significant change in the acoustic properties, such as phantom A (uniform phantom), thus allowing a significant variance reduction. However, increasing the weights to reduce the variance can result in biased

estimates. In other words, there is a trade-off between variance and bias in the selection of the weights. An interesting future work would be introducing an automated method to select the weights based on identifying what acoustic properties are the most influential in the selection process. The weights that result from applying this method to representative data from various organs could be saved as part of the imaging presets in the scanner to provide parametric images in real-time.

The attenuation coefficient was assumed to be linearly dependent on frequency. A more realistic model would be a power-law fit [114]. However, the effect of the power law dependence could be minimized by the averaging effect of the effective attenuation. If a significant deviation from a linear dependence on frequency is expected, our regularized-based methods could be applied over contiguous, narrow frequency bands over which the variation of the effective attenuation with frequency could be approximated as linear, as implemented by Nasief *et al.* [115]. Then, the values obtained from the various frequency bands could be combined.

A possible extension of our work on estimating the ESD and AC would be applying our proposed method to more complex phantoms that reflect the characteristics of real tissue. Furthermore, comparing the analytical approach to iterative approaches using nonlinear solvers such as Nelder Mead Simplex and Bayesian Optimization can be interesting.

The field of deep learning is rapidly developing as a powerful tool for addressing a wide range of challenges, including QUS parameter estimations for better tissue characterization. The properties of scatterers can be learned from RF data using deep learning algorithms. However, all medical applications, including QUS, suffer from limited data sets as a major limitation of deep learning techniques.

## References

- [1] D. Jankovic and P. Peng, *Regional nerve blocks in anesthesia and pain therapy: traditional and ultrasound-guided techniques*. Springer, 2015.
- [2] G. Cloutier, F. Destrempes, F. Yu, and A. Tang, “Quantitative ultrasound imaging of soft biological tissues: a primer for radiologists and medical physicists,” *Insights Imaging*, vol. 12, no. 1, pp. 1–20, 2021.
- [3] M. F. Insana, T. J. Hall, and J. L. Fishback, “Identifying acoustic scattering sources in normal renal parenchyma from the anisotropy in acoustic properties,” *Ultrasound Med. Biol.*, vol. 17, no. 6, pp. 613–626, 1991.
- [4] D. Nicholas, “Evaluation of backscattering coefficients for excised human tissues: results, interpretation and associated measurements,” *Ultrasound Med. Biol.*, vol. 8, no. 1, pp. 17–28, 1982.
- [5] Y. Hirooka, A. Itoh, H. Kawashima, E. Ohno, Y. Itoh, Y. Nakamura, T. Hiramatsu, H. Sugimoto, H. Sumi, and D. Hayashi, “Feasibility of newly developed endoscopic ultrasound with zone sonography technology for diagnosis of pancreatic diseases,” *Gut Liver*, vol. 7, no. 4, p. 486, 2013.
- [6] T. M. Bui, A. Coron, J. Mamou, E. Saegusa-Beecroft, T. Yamaguchi, E. Yanagihara, J. Machi, S. L. Bridal, and E. J. Feleppa, “Local transverse-slice-based level-set method for segmentation of 3-D high-frequency ultrasonic backscatter from dissected human lymph nodes,” *IEEE Trans. Biomed. Eng.*, vol. 64, no. 7, pp. 1579–1591, 2016.
- [7] T. Yamaguchi, “Basic concept and clinical applications of quantitative ultrasound (QUS) technologies,” *J. Med. Ultrason.*, vol. 48, no. 4, pp. 391–402, 2021.
- [8] F. Destrempes and G. Cloutier, “Statistical modeling of ultrasound signals related to the packing factor of wave scattering phenomena for structural characterization,” *J. Acoust. Soc. Am.*, vol. 150, no. 5, pp. 3544–3556, 2021.
- [9] F. Destrempes, M. Gesnik, B. Chayer, M.-H. Roy-Cardinal, D. Oliv  , J.-M. Giard, G. Sebastiani, B. N. Nguyen, G. Cloutier, and A. Tang, “Quantitative ultrasound, elastography, and machine learning for assessment of steatosis, inflammation, and fibrosis in chronic liver

- disease,” *PLoS One*, vol. 17, no. 1, p. e0262291, 2022.
- [10] F. Destrempes and G. Cloutier, “Interpretation based on stochastic geometry of homodyned-K distribution scatterer clustering parameter for quantitative ultrasound imaging,” in *2020 IEEE International Ultrasonics Symposium (IUS)*, 2020, pp. 1–4.
- [11] G. Cloutier, M. Daronat, D. Savéry, D. Garcia, L.-G. Durand, and F. S. Foster, “Non-Gaussian statistics and temporal variations of the ultrasound signal backscattered by blood at frequencies between 10 and 58 MHz,” *J. Acoust. Soc. Am.*, vol. 116, no. 1, pp. 566–577, 2004.
- [12] F. Destrempes, J. Porée, and G. Cloutier, “Estimation method of the homodyned K-distribution based on the mean intensity and two log-moments,” *SIAM J. Imaging Sci.*, vol. 6, no. 3, pp. 1499–1530, 2013.
- [13] H. Rivaz, R. Zellars, G. Hager, G. Fichtinger, and E. Boctor, “9c-1 beam steering approach for speckle characterization and out-of-plane motion estimation in real tissue,” in *2007 IEEE Ultrasonics Symposium Proceedings*, 2007, pp. 781–784.
- [14] H. Rivaz, E. M. Boctor, and G. Fichtinger, “P3E-9 ultrasound speckle detection using low order moments,” in *2006 IEEE Ultrasonics Symposium*, 2006, pp. 2092–2095.
- [15] M. L. Oelze and J. Mamou, “Review of Quantitative Ultrasound: Envelope Statistics and Backscatter Coefficient Imaging and Contributions to Diagnostic Ultrasound,” *IEEE Trans. Ultrason. Ferroelectr. Freq. Control*, vol. 63, no. 2, pp. 336–351, 2016, doi: 10.1109/TUFFC.2015.2513958.
- [16] F. Destrempes and G. Cloutier, “A critical review and uniformized representation of statistical distributions modeling the ultrasound echo envelope,” *Ultrasound Med. Biol.*, vol. 36, no. 7, pp. 1037–1051, 2010.
- [17] M. F. Insana and T. J. Hall, “Characterising the microstructure of random media using ultrasound,” *Phys. Med. Biol.*, vol. 35, no. 10, p. 1373, 1990.
- [18] S. A. Wickline, E. D. Verdonk, A. K. Wong, R. K. Shepard, and J. G. Miller, “Structural remodeling of human myocardial tissue after infarction. Quantification with ultrasonic backscatter,” *Circulation*, vol. 85, no. 1, pp. 259–268, 1992.

- [19] B. J. Oosterveld, J. M. Thijssen, P. C. Hartman, R. L. Romijn, and G. J. E. Rosenbusch, "Ultrasound attenuation and texture analysis of diffuse liver disease: methods and preliminary results," *Phys. Med. Biol.*, vol. 36, no. 8, p. 1039, 1991.
- [20] R. Kuc, "Clinical application of an ultrasound attenuation coefficient estimation technique for liver pathology characterization," *IEEE Trans. Biomed. Eng.*, no. 6, pp. 312–319, 1980.
- [21] A. C. Kak and K. A. Dines, "Signal processing of broadband pulsed ultrasound: measurement of attenuation of soft biological tissues," *IEEE Trans. Biomed. Eng.*, no. 4, pp. 321–344, 1978.
- [22] R. Kuc and M. Schwartz, "Estimating the acoustic attenuation coefficient slope for liver from reflected ultrasound signals," *IEEE Trans. Sonics Ultrason.*, vol. 26, no. 5, pp. 353–361, 1979.
- [23] T. Tada, T. Nishimura, M. Yoshida, and H. Iijima, "Nonalcoholic fatty liver disease and nonalcoholic steatohepatitis: new trends and role of ultrasonography," *J. Med. Ultrason.*, vol. 47, no. 4, pp. 511–520, 2020.
- [24] M. F. Insana, T. J. Hall, and L. T. Cook, "Backscatter coefficient estimation using array transducers," *IEEE Trans. Ultrason. Ferroelectr. Freq. Control*, vol. 41, no. 5, pp. 714–723, 1994.
- [25] M. F. Insana, R. F. Wagner, D. G. Brown, and T. J. Hall, "Describing small-scale structure in random media using pulse-echo ultrasound," *J. Acoust. Soc. Am.*, vol. 87, no. 1, pp. 179–192, 1990.
- [26] J. Mamou, M. L. Oelze, W. D. O'Brien Jr, and J. F. Zachary, "Identifying ultrasonic scattering sites from three-dimensional impedance maps," *J. Acoust. Soc. Am.*, vol. 117, no. 1, pp. 413–423, 2005.
- [27] F. L. Lizzi, M. Ostromogilsky, E. J. Feleppa, M. C. Rorke, and M. M. Yaremko, "Relationship of ultrasonic spectral parameters to features of tissue microstructure," *IEEE Trans. Ultrason. Ferroelectr. Freq. Control*, vol. 34, no. 3, pp. 319–329, 1987.
- [28] J. Mamou and M. L. Oelze, *Quantitative ultrasound in soft tissues*. 2013. doi: 10.1007/978-94-007-6952-6.

- [29] T. Liu, F. L. Lizzi, R. H. Silverman, G. J. Kutcher, and I. Introduction, “Ultrasonic tissue characterization using 2-D spectrum analysis and its application in ocular tumor diagnosis,” pp. 1032–1039, 2004, doi: 10.1118/1.1690196.
- [30] M. F. Insana, T. J. Hall, J. G. Wood, and Z. Y. Yan, “Renal ultrasound using parametric imaging techniques to detect changes in microstructure and function,” *Invest. Radiol.*, vol. 28, no. 8, pp. 720–725, 1993.
- [31] M. L. Oelze and J. F. Zachary, “Examination of cancer in mouse models using high-frequency quantitative ultrasound,” *Ultrasound Med. Biol.*, vol. 32, no. 11, pp. 1639–1648, 2006, doi: 10.1016/j.ultrasmedbio.2006.05.006.
- [32] H. G. Nasief, I. M. Rosado-Mendez, J. A. Zagzebski, and T. J. Hall, “A quantitative ultrasound-based multi-parameter classifier for breast masses,” *Ultrasound Med. Biol.*, vol. 45, no. 7, pp. 1603–1616, 2019.
- [33] A. Sadeghi-Naini, H. Suraweera, W. T. Tran, F. Hadizad, G. Bruni, R. F. Rastegar, B. Curpen, and G. J. Czarnota, “Breast-lesion characterization using textural features of quantitative ultrasound parametric maps,” *Sci. Rep.*, vol. 7, no. 1, pp. 1–10, 2017.
- [34] A. Coila, G. Torres, J. Rouyer, S. Aristizabal, M. Urban, and R. Lavarello, “Recent developments in spectral-based ultrasonic tissue characterization,” in *2018 IEEE 15th International Symposium on Biomedical Imaging (ISBI 2018)*, 2018, pp. 1018–1021.
- [35] K. A. Wear, R. F. Wagner, M. F. Insana, and T. J. Hall, “Application of autoregressive spectral analysis to cepstral estimation of mean scatterer spacing,” *IEEE Trans. Ultrason. Ferroelectr. Freq. Control*, vol. 40, no. 1, pp. 50–58, 1993.
- [36] Z. Zhou, W. Wu, S. Wu, K. Jia, and P. H. Tsui, “A Review of Ultrasound Tissue Characterization with Mean Scatterer Spacing,” *Ultrason. Imaging*, vol. 39, no. 5, pp. 263–282, 2017, doi: 10.1177/0161734617692018.
- [37] N. I. Nizam, S. R. Ara, K. Hasan, and S. P. Jul, “Classification of Breast Lesions Using Quantitative Ultrasound Biomarkers,” pp. 1–14.
- [38] W. C. A. Pereira, S. L. Bridal, A. Coron, and P. Laugier, “Mean scatterer spacing of backscattered ultrasound signals from in vitro human cancellous bone specimens,” in *2002*

- IEEE Ultrasonics Symposium, 2002. Proceedings.*, 2002, vol. 2, pp. 1337–1340.
- [39] P. Gong, P. Song, C. Huang, J. Trzasko, and S. Chen, “System-independent ultrasound attenuation coefficient estimation using spectra normalization,” *IEEE Trans. Ultrason. Ferroelectr. Freq. Control*, vol. 66, no. 5, pp. 867–875, 2019, doi: 10.1109/TUFFC.2019.2903010.
- [40] K. Nam, J. A. Zagzebski, and T. J. Hall, “Quantitative assessment of in vivo breast masses using ultrasound attenuation and backscatter,” *Ultrason. Imaging*, vol. 35, no. 2, pp. 146–161, 2013.
- [41] G. Ghoshal, J. Mamou, and M. L. Oelze, “State of the art methods for estimating backscatter coefficients,” in *Quantitative ultrasound in soft tissues*, Springer, 2013, pp. 3–19.
- [42] F. Destrempe, E. Franceschini, T. H. François, and G. Cloutier, “Unifying concepts of statistical and spectral quantitative ultrasound techniques,” *IEEE Trans. Med. Imaging*, vol. 35, no. 2, pp. 488–500, 2015.
- [43] A. K. Z. Tehrani, M. Amiri, I. M. Rosado-Mendez, T. J. Hall, and H. Rivaz, “Ultrasound scatterer density classification using convolutional neural networks and patch statistics,” *IEEE Trans. Ultrason. Ferroelectr. Freq. Control*, vol. 68, no. 8, pp. 2697–2706, 2021.
- [44] M. Amiri, A. K. Z. Tehrani, and H. Rivaz, “Segmentation of ultrasound images based on scatterer density using U-Net,” in *2020 42nd Annual International Conference of the IEEE Engineering in Medicine & Biology Society (EMBC)*, 2020, pp. 2063–2066.
- [45] A. K. Z. Tehrani, I. M. Rosado-Mendez, and H. Rivaz, “Robust Scatterer Number Density Segmentation of Ultrasound Images,” *IEEE Trans. Ultrason. Ferroelectr. Freq. Control*, vol. 69, no. 4, pp. 1169–1180, 2022.
- [46] L. Zhang, V. Vishnevskiy, and O. Goksel, “Deep network for scatterer distribution estimation for ultrasound image simulation,” *IEEE Trans. Ultrason. Ferroelectr. Freq. Control*, vol. 67, no. 12, pp. 2553–2564, 2020.
- [47] M. Byra, H. Piotrkowska-Wróblewska, K. Dobruch-Sobczak, and A. Nowicki, “Combining Nakagami imaging and convolutional neural network for breast lesion classification,” in *2017 IEEE International Ultrasonics Symposium (IUS)*, 2017, pp. 1–4.

- [48] B. S. Garra, “Elastography: history, principles, and technique comparison,” *Abdom. Imaging*, vol. 40, no. 4, pp. 680–697, 2015.
- [49] S. Mondillo, M. Galderisi, D. Mele, M. Cameli, V. S. Lomoriello, V. Zacà, P. Ballo, A. D’Andrea, D. Muraru, and M. Losi, “Speckle-tracking echocardiography: a new technique for assessing myocardial function,” *J. Ultrasound Med.*, vol. 30, no. 1, pp. 71–83, 2011.
- [50] A. L. Coila and R. Lavarello, “Regularized spectral log difference technique for ultrasonic attenuation imaging,” *IEEE Trans. Ultrason. Ferroelectr. Freq. Control*, vol. 65, no. 3, pp. 378–389, 2017.
- [51] F. Deeba, C. Schneider, S. Mohammed, M. Honarvar, E. Tam, S. Salcudean, and R. Rohling, “SWTV-ACE: spatially weighted regularization based attenuation coefficient estimation method for hepatic steatosis detection,” in *International Conference on Medical Image Computing and Computer-Assisted Intervention*, 2019, pp. 610–618.
- [52] F. Destrempes, M. Gesnik, and G. Cloutier, “Construction of adaptively regularized parametric maps for quantitative ultrasound imaging,” in *2019 IEEE International Ultrasonics Symposium (IUS)*, 2019, pp. 2027–2030.
- [53] A. Coila, R. Laines, C. Salazar, J. Rouyer, G. Jimenez, J. A. Pinto, J. Guerrero, and R. Lavarello, “In vivo attenuation estimation in human thyroid nodules using the regularized spectral log difference technique: Initial pilot study,” in *2017 IEEE International Ultrasonics Symposium (IUS)*, 2017, pp. 1–4.
- [54] A. C. Saavedra, A. Coila, J. Arroyo, B. Castaneda, and R. J. Lavarello, “In vivo attenuation coefficient estimation in the healthy forearm and thigh human dermis,” in *2018 IEEE International Ultrasonics Symposium (IUS)*, 2018, pp. 1–4.
- [55] A. B. and R. L. Hector Chahuaray, “Regularized framework for simultaneous estimation of ultrasonic attenuation and backscatter coefficients,” in *IEEE International Ultrasonics Symposium (IUS)*, 2020.
- [56] Z. Vajihi, I. M. Rosado-Mendez, T. J. Hall, and H. Rivaz, “Low Variance Estimation of Backscatter Quantitative Ultrasound Parameters Using Dynamic Programming,” *IEEE Trans. Ultrason. Ferroelectr. Freq. Control*, vol. PP, no. 1, p. 1, 2018, doi:

10.1109/TUFFC.2018.2869810.

- [57] K. Nam, J. A. Zagzebski, and T. J. Hall, “Simultaneous backscatter and attenuation estimation using a least squares method with constraints,” *Ultrasound Med. Biol.*, vol. 37, no. 12, pp. 2096–2104, 2011, doi: 10.1016/j.ultrasmedbio.2011.08.008.
- [58] F. Deeba, C. Schneider, S. Mohammed, M. Honarvar, J. Lobo, E. Tam, S. Salcudean, and R. Rohling, “A multiparametric volumetric quantitative ultrasound imaging technique for soft tissue characterization,” *Med. Image Anal.*, vol. 74, p. 102245, 2021.
- [59] M. Grant, S. Boyd, and Y. Ye, “CVX: Matlab software for disciplined convex programming (web page and software).” 2009.
- [60] I. Rafati, F. Destrepes, and G. Cloutier, “Regularized phantom-free construction of local attenuation coefficient slope maps for quantitative ultrasound imaging,” in *2020 IEEE International Ultrasonics Symposium (IUS)*, 2020, pp. 1–3.
- [61] J. Birdi, J. D’hooge, and A. Bertrand, “Spatially Variant Ultrasound Attenuation Mapping using a Regularized Linear Least-Squares Approach,” *IEEE Trans. Ultrason. Ferroelectr. Freq. Control*, 2022.
- [62] M. L. Oelze and W. D. O’Brien Jr, “Method of improved scatterer size estimation and application to parametric imaging using ultrasound,” *J. Acoust. Soc. Am.*, vol. 112, no. 6, pp. 3053–3063, 2002.
- [63] R. Lavarello and M. Oelze, “Quantitative ultrasound estimates from populations of scatterers with continuous size distributions: Effects of the size estimator algorithm,” *IEEE Trans. Ultrason. Ferroelectr. Freq. Control*, vol. 59, no. 9, pp. 2066–2076, 2012.
- [64] R. Lavarello and M. Oelze, “Quantitative ultrasound estimates from populations of scatterers with continuous size distributions,” *IEEE Trans. Ultrason. Ferroelectr. Freq. Control*, vol. 58, no. 4, pp. 744–753, 2011.
- [65] E. P. Nordberg and T. J. Hall, “Effective scatterer diameter estimates for broad scatterer size distributions,” *Ultrason. Imaging*, vol. 37, no. 1, pp. 3–21, 2015.
- [66] M. F. Insana, J. G. Wood, and T. J. Hall, “Identifying acoustic scattering sources in normal

- renal parenchyma in vitro by varying arterial and ureteral pressures,” *Ultrasound Med. Biol.*, vol. 18, no. 6–7, pp. 587–599, 1992.
- [67] B. S. Garra, M. F. Insana, I. A. Sesterhenn, T. J. Hall, R. F. Wagner, C. Rotellar, J. Winchester, and R. K. Zeman, “Quantitative ultrasonic detection of parenchymal structural change in diffuse renal disease.,” *Invest. Radiol.*, vol. 29, no. 2, pp. 134–140, 1994.
- [68] T. N. Nguyen, A. S. Podkova, A. Y. Tam, E. C. Arnold, R. J. Miller, T. H. Park, M. N. Do, and M. L. Oelze, “Characterizing Fatty Liver in vivo in Rabbits, Using Quantitative Ultrasound,” *Ultrasound Med. Biol.*, vol. 45, no. 8, pp. 2049–2062, 2019, doi: 10.1016/j.ultrasmedbio.2019.03.021.
- [69] A. Han, J. W. Erdman, D. G. Simpson, M. P. Andre, and W. D. O’Brien, “Early detection of fatty liver disease in mice via quantitative ultrasound,” in *2014 IEEE International Ultrasonics Symposium*, 2014, pp. 2363–2366.
- [70] G. Ghoshal, R. J. Lavarello, J. P. Kemmerer, R. J. Miller, and M. L. Oelze, “Ex vivo study of quantitative ultrasound parameters in fatty rabbit livers,” *Ultrasound Med. Biol.*, vol. 38, no. 12, pp. 2238–2248, 2012.
- [71] S. C. Lin, E. Heba, T. Wolfson, B. Ang, A. Gamst, A. Han, J. W. Erdman Jr, W. D. O’Brien Jr, M. P. Andre, and C. B. Sirlin, “Noninvasive diagnosis of nonalcoholic fatty liver disease and quantification of liver fat using a new quantitative ultrasound technique,” *Clin. Gastroenterol. Hepatol.*, vol. 13, no. 7, pp. 1337–1345, 2015.
- [72] Q. W. Guerrero, H. Feltovich, I. M. Rosado-Mendez, L. C. Carlson, G. Li, and T. J. Hall, “Anisotropy and spatial heterogeneity in quantitative ultrasound parameters: Relevance to the study of the human cervix,” *Ultrasound Med. Biol.*, vol. 44, no. 7, pp. 1493–1503, 2018.
- [73] Q. W. Guerrero, H. Feltovich, I. M. Rosado-Mendez, L. C. Carlson, and T. J. Hallcor, “Quantitative Ultrasound Biomarkers Based on Backscattered Acoustic Power: Potential for Quantifying Remodeling of the Human Cervix during Pregnancy,” *Ultrasound Med. Biol.*, vol. 45, no. 2, pp. 429–439, 2019, doi: 10.1016/j.ultrasmedbio.2018.08.019.
- [74] M. L. Oelze, J. P. Kemmerer, G. Ghoshal, and R. M. Vlad, “Therapy monitoring and assessment using quantitative ultrasound,” in *Quantitative Ultrasound in Soft Tissues*,

- Springer, 2013, pp. 193–216.
- [75] M. L. Oelze, “Quantitative ultrasound successes: past, present and future,” in *Medical Imaging 2020: Ultrasonic Imaging and Tomography*, 2020, vol. 11319, p. 113190X.
- [76] T. Nguyen and M. Oelze, “Reference free quantitative ultrasound classification of fatty liver,” in *2019 IEEE International Ultrasonics Symposium (IUS)*, 2019, pp. 2424–2427.
- [77] A. Han, A. S. Boehringer, Y. N. Zhang, V. Montes, M. P. Andre, J. W. Erdman, R. Loomba, C. B. Sirlin, and W. D. O’Brien, “Improved assessment of hepatic steatosis in humans using multi-parametric quantitative ultrasound,” in *2019 IEEE International Ultrasonics Symposium (IUS)*, 2019, pp. 1819–1822.
- [78] D. Rohrbach, B. Wodlinger, J. Wen, J. Mamou, and E. Feleppa, “High-frequency quantitative ultrasound for imaging prostate cancer using a novel micro-ultrasound scanner,” *Ultrasound Med. Biol.*, vol. 44, no. 7, pp. 1341–1354, 2018.
- [79] G. I. Baroncelli, “Quantitative ultrasound methods to assess bone mineral status in children: technical characteristics, performance, and clinical application,” *Pediatr. Res.*, vol. 63, no. 3, pp. 220–228, 2008.
- [80] K. Quiaoit, D. DiCenzo, K. Fatima, D. Bhardwaj, L. Sannachi, M. Gangeh, A. Sadeghi-Naini, A. Dasgupta, M. C. Kolios, and M. Trudeau, “Quantitative ultrasound radiomics for therapy response monitoring in patients with locally advanced breast cancer: Multi-institutional study results,” *PLoS One*, vol. 15, no. 7, p. e0236182, 2020.
- [81] H. Rivaz, E. M. Boctor, M. A. Choti, and G. D. Hager, “Real-time regularized ultrasound elastography,” *IEEE Trans. Med. Imaging*, vol. 30, no. 4, pp. 928–945, 2010.
- [82] H. S. Hashemi and H. Rivaz, “Global time-delay estimation in ultrasound elastography,” *IEEE Trans. Ultrason. Ferroelectr. Freq. Control*, vol. 64, no. 10, pp. 1625–1636, 2017.
- [83] L. X. Yao, J. A. Zagzebski, and E. L. Madsen, “Backscatter coefficient measurements using a reference phantom to extract depth-dependent instrumentation factors,” *Ultrason. Imaging*, vol. 12, no. 1, pp. 58–70, 1990.
- [84] K. Nam, I. M. Rosado-Mendez, L. A. Wirtzfeld, G. Ghoshal, A. D. Pawlicki, E. L. Madsen,

- R. J. Lavarello, M. L. Oelze, J. A. Zagzebski, and W. D. O'Brien Jr, "Comparison of ultrasound attenuation and backscatter estimates in layered tissue-mimicking phantoms among three clinical scanners," *Ultrason. Imaging*, vol. 34, no. 4, pp. 209–221, 2012.
- [85] I. E. Commission, "Ultrasonics–Pulse-echo scanners: Part 2. Measurement of maximum depth of penetration and local dynamic range," *IEC*, pp. 61391–61392, 2010.
- [86] E. L. Madsen, F. Dong, G. R. Frank, B. S. Garra, K. A. Wear, T. Wilson, J. A. Zagzebski, H. L. Miller, K. K. Shung, and S. H. Wang, "Interlaboratory comparison of ultrasonic backscatter, attenuation, and speed measurements.," *J. ultrasound Med.*, vol. 18, no. 9, pp. 615–631, 1999.
- [87] J.-F. Chen, J. A. Zagzebski, and E. L. Madsen, "Tests of backscatter coefficient measurement using broadband pulses," *IEEE Trans. Ultrason. Ferroelectr. Freq. Control*, vol. 40, no. 5, pp. 603–607, 1993.
- [88] I. M. Rosado-Mendez, K. Nam, T. J. Hall, and J. A. Zagzebski, "Task-oriented comparison of power spectral density estimation methods for quantifying acoustic attenuation in diagnostic ultrasound using a reference phantom method," *Ultrason. Imaging*, vol. 35, no. 3, pp. 214–234, 2013.
- [89] G. Strang and K. Borre, *Linear algebra, geodesy, and GPS*. Siam, 1997.
- [90] "mldivide, \." <https://www.mathworks.com/help/matlab/ref/mldivide.html>
- [91] N. Jafarpisheh, T. J. Hall, H. Rivaz, and I. M. Rosado-Mendez, "Analytic Global Regularized Backscatter Quantitative Ultrasound," *IEEE Trans. Ultrason. Ferroelectr. Freq. Control*, vol. 68, no. 5, pp. 1605–1617, 2021, doi: 10.1109/TUFFC.2020.3042942.
- [92] K. Nam, J. A. Zagzebski, and T. J. Hall, "Simultaneous backscatter and attenuation estimation using a least squares method with constraints," *Ultrasound Med. Biol.*, vol. 37, no. 12, pp. 2096–2104, 2011.
- [93] A. C. Luchies, G. Ghoshal, W. D. O'brien, and M. L. Oelze, "Quantitative ultrasonic characterization of diffuse scatterers in the presence of structures that produce coherent echoes," *IEEE Trans. Ultrason. Ferroelectr. Freq. Control*, vol. 59, no. 5, pp. 893–904, 2012.

- [94] K. Nam, J. A. Zagzebski, and T. J. Hall, “Quantitative Assessment of In Vivo Breast Masses Using Ultrasound Attenuation and Backscatter,” 2013, doi: 10.1177/0161734613480281.
- [95] F. Deeba, R. Hu, J. Terry, D. Pugash, J. A. Hutcheon, C. Mayer, S. Salcudean, and R. Rohling, “A Spatially Weighted Regularization Method for Attenuation Coefficient Estimation,” in *2019 IEEE International Ultrasonics Symposium (IUS)*, 2019, pp. 2023–2026.
- [96] M. F. Insana and T. J. Hall, “Parametric ultrasound imaging from backscatter coefficient measurements: image formation and interpretation,” *Ultrason. Imaging*, vol. 12, no. 4, pp. 245–267, 1990.
- [97] A. Sadeghi-Naini, L. Sannachi, H. Tadayyon, W. T. Tran, E. Slodkowska, M. Trudeau, S. Gandhi, K. Pritchard, M. C. Kolios, and G. J. Czarnota, “Chemotherapy-response monitoring of breast cancer patients using quantitative ultrasound-based intra-tumour heterogeneities,” *Sci. Rep.*, vol. 7, no. 1, pp. 1–12, 2017.
- [98] N. Jafarpisheh, I. M. Rosado-Mendez, T. J. Hall, and H. Rivaz, “Regularized Estimation of Effective Scatterer Size and Acoustic Concentration Quantitative Ultrasound Parameters Using Dynamic Programming,” in *42nd Annual International Conference of the IEEE Engineering in Medicine and Biology Society (EMBC)*, 2020.
- [99] T. J. Hall, M. F. Insana, L. A. Harrison, N. M. Soller, and K. J. Schlehr, “Ultrasound contrast-detail analysis: A comparison of low-contrast detectability among scanhead designs,” *Med. Phys.*, vol. 22, no. 7, pp. 1117–1125, 1995.
- [100] T. J. Hall, M. F. Insana, N. M. Soller, and L. A. Harrison, “Ultrasound contrast-detail analysis: a preliminary study in human observer performance,” *Med. Phys.*, vol. 20, no. 1, pp. 117–127, 1993.
- [101] N. Jafarpisheh, I. M. Rosado-Mendez, T. J. Hall, and H. Rivaz, “Regularized Estimation of Effective Scatterer Size and Acoustic Concentration Quantitative Ultrasound Parameters Using Dynamic Programming,” in *2020 42nd Annual International Conference of the IEEE Engineering in Medicine & Biology Society (EMBC)*, 2020, pp. 13–16.
- [102] M. F. Insana and D. G. Brown, “Acoustic scattering theory applied to soft biological

- tissues,” *Ultrason. Scatt. Biol. tissues*, pp. 75–124, 1993.
- [103] R. K. Saha and M. C. Kolios, “Effects of cell spatial organization and size distribution on ultrasound backscattering,” *IEEE Trans. Ultrason. Ferroelectr. Freq. Control*, vol. 58, no. 10, pp. 2118–2131, 2011.
- [104] D. Savéry and G. Cloutier, “Effect of red cell clustering and anisotropy on ultrasound blood backscatter: A Monte Carlo study,” *IEEE Trans. Ultrason. Ferroelectr. Freq. Control*, vol. 52, no. 1, pp. 94–103, 2005.
- [105] I. Fontaine, D. Savéry, and G. Cloutier, “Simulation of ultrasound backscattering by red cell aggregates: Effect of shear rate and anisotropy,” *Biophys. J.*, vol. 82, no. 4, pp. 1696–1710, 2002.
- [106] D. J. Anstee and F. A. Spring, “Red cell membrane glycoproteins with a broad tissue distribution,” *Transfus. Med. Rev.*, vol. 3, no. 1, pp. 13–23, 1989.
- [107] P. Chaturvedi, M. F. Insana, and T. J. Hall, “Ultrasonic and elasticity imaging to model disease-induced changes in soft-tissue structure,” *Med. Image Anal.*, vol. 2, no. 4, pp. 325–338, 1998.
- [108] M. Grant and S. Boyd, “CVX: Matlab software for disciplined convex programming, version 2.1.” 2014.
- [109] Y. Rubner, C. Tomasi, and L. J. Guibas, “The earth mover’s distance as a metric for image retrieval,” *Int. J. Comput. Vis.*, vol. 40, no. 2, pp. 99–121, 2000.
- [110] A. Faggiano, J. Coulot, N. Bellon, M. Talbot, B. Caillou, M. Ricard, J.-M. Bidart, and M. Schlumberger, “Age-dependent variation of follicular size and expression of iodine transporters in human thyroid tissue,” *J. Nucl. Med.*, vol. 45, no. 2, pp. 232–237, 2004.
- [111] J. Tripette, L.-C. Nguyen, L. Allard, P. Robillard, G. Soulez, and G. Cloutier, “In vivo venous assessment of red blood cell aggregate sizes in diabetic patients with a quantitative cellular ultrasound imaging method: Proof of concept,” *PLoS One*, vol. 10, no. 4, p. e0124712, 2015.
- [112] N. Jafarpisheh, I. M. Rosado-Mendez, T. J. Hall, and H. Rivaz, “Estimation of the Scatterer

- Size Distributions in Quantitative Ultrasound Using Constrained Optimization,” in *2021 IEEE International Ultrasonics Symposium (IUS)*, 2021, pp. 1–4.
- [113] Z. Vajihi, I. Rosado-Mendez, T. J. Hall, and H. Rivaz, “L1 and l2 norm depth-regularized estimation of the acoustic attenuation and backscatter coefficients using dynamic programming,” in *2019 IEEE 16th International Symposium on Biomedical Imaging (ISBI 2019)*, 2019, pp. 1749–1752.
- [114] T. L. Szabo, *Diagnostic ultrasound imaging: inside out*. Academic Press, 2004.
- [115] H. G. Nasief, I. M. Rosado-Mendez, J. A. Zagzebski, and T. J. Hall, “Acoustic properties of breast fat,” *J. Ultrasound Med.*, vol. 34, no. 11, pp. 2007–2016, 2015.